University of Zurich[UZH]

# Monitoring arctic snow and ice melt using SAR gamma nought backscatter, passive microwave- and scatterometer instruments

GEO 511 Master's Thesis


**Author**
Simon Hagmayer
13-916-812

**Supervised by**
Dr. David Small

**Faculty representative**
Prof. Dr. Michael Schaepman



29.04.2019
Department of Geography, University of Zurich

University of Zurich[UZH]

Department of Geography

# Monitoring arctic snow and ice melt using SAR gamma nought ($\gamma_c^0$) backscatter, passive microwave- and scatterometer instruments

GEO 511 Master's Thesis

**Author**
Simon Hagmayer
13-916-812

SAR **melt onset** in 2018
HH polarization, 2 day composites

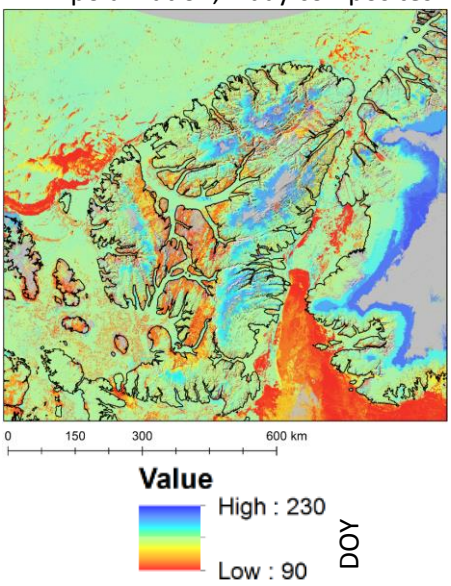


SAR **number of melt days** in 2018
HH polarization, 2 day composites

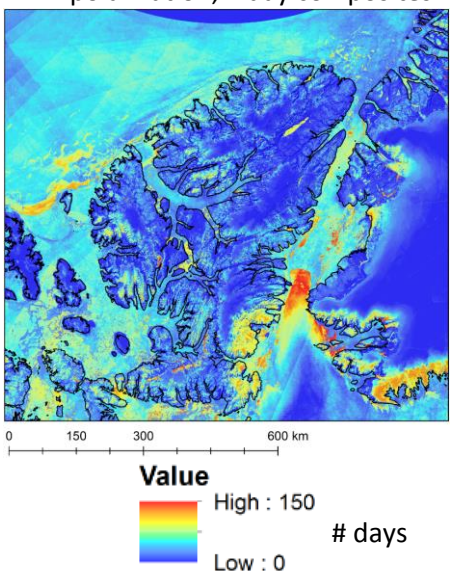


SAR **melt end** in 2018
HH polarization, 2 day composites

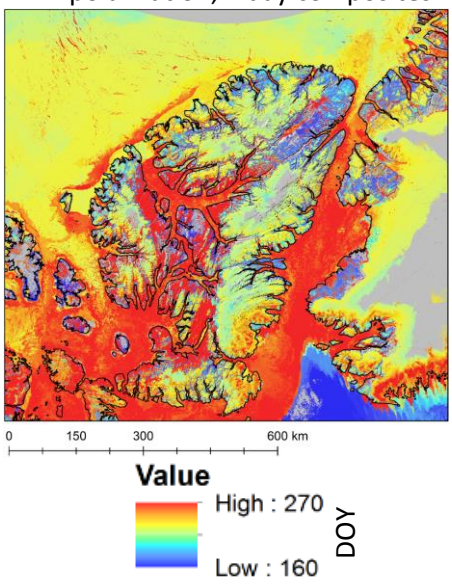


**Supervised by**
Dr. David Small

**Faculty representative**
Prof. Dr. Michael Schaepman

29.04.2019
Department of Geography, University of Zurich

# Table of content

# Abstract

Snow is of global importance for the climate, freshwater availability, vegetation cycle and natural hazards. Snow has a high albedo and is one of the most prominent and active surface materials in Arctic ecosystems. Since the 1960s a decrease of snow cover is observed on a global scale and since the 1970s also a decrease in Arctic sea ice. Information on snow water equivalent, snow extent and melt onset is crucial for climatic and hydrological models and for disaster assessments. Historically, melt onset estimates with remote sensing was addressed since 1979 using passive microwave (PM) imagery, because of the sensor's daily revisit time and the weather and light independence of microwave sensors. However, the spatial resolution of PM is limited to 10-25 km. Scatterometer instruments, like the Advanced Scatterometer (ASCAT) were used since 2000 to detect melt processes with a spatial resolution of about 5 km. Synthetic Aperture Radar (SAR) instruments have a much higher spatial resolution of ~20-100 m, but the sensors do not have such a high temporal resolution like PM or scatterometers. Furthermore, different viewing geometries complicate the task of detecting melt processes. With the concept of gamma nought ($\gamma_c^0$) these disadvantages can be addressed. $\gamma_c^0$ backscatter composites can combine different C-band SAR sensors and passes to improve the temporal resolution. Moreover, the $\gamma_c^0$ are radiometrically terrain corrected, making the backscatter more robust against different viewing geometries and the influence of the terrain. In this study the capability of $\gamma_c^0$ backscatter composites in HH and HV polarizations to detect melt processes on Ellesmere Island and the surrounding Arctic sea ice was tested. The composites were derived from Sentinel-1 and RADARSAT-2 acquisitions. Wet snow or ice areas (WSIA) were mapped throughout the melt seasons, as well as melt onset, ending and the number of melt days from 2015 to 2018. Results were compared to the often used scatterometer and PM instruments, as well as weather data to investigate advantages and disadvantages each instrument type holds. A threshold based change detection method was applied to all instrument types. Results indicated a high resemblance between SAR, ASCAT and PM instruments, where SAR showed the strongest correlation to temperature data (r = 0.73). SAR derived melt onset products also showed the strongest similarities with MODIS surface temperature data. The improved spatial resolution and the now sufficient temporal resolution of SAR clearly showed the advantages of using SAR data in future melt monitoring, especially in rough terrain. Additionally, a new method is presented here, using no reference scene to detect melt processes. The new method showed an even higher resemblance to PM derived sea-ice onsets and a higher robustness against sea ice structure influences, but presumably worse results on land areas.

# 1. Introduction

## 1.1. The importance of snow and sea ice

Snow is of global and regional importance and one of the most active natural elements on the Earth's surface. Due to the high albedo of snow, it reflects a major part of the incoming solar radiation back to space, leading to a reduced warming of the Earth's surface (Klein et al. 2000), (Klein and Stroeve, 2002), (Jain et al. 2008), (Zhao and Fernandes 2009). During midwinter on the northern hemisphere, 40-50% of the land surface is covered with snow (Hall et al. 1995), (Pepe et al. 2005), (Lemke et al. 2007). Snow melting is the main source of freshwater in many regions, like in the western US (Guangjun et al., 2017). In many countries like Switzerland, hydropower is the main source of electricity generation, where snow plays an important role (Vikhamar and Solberg 2003). In Arctic ecosystems, snow is one of the most prominent and important surface types (Colbeck et al., 2015), (Barnett et al., 2005). The hydrology, the vegetation development and cycle, as well as permafrost presence are directly related to the snowmelt its accumulation cycle. Variations in the duration and the timing of snow cover affect the ground thermal regime, because snow cover strongly affects the surface albedo. The surface albedo is a crucial parameter in the surface energy balance, influencing the active layer of permafrost. Snow cover during winter results in higher ground temperatures, whereas snow cover in summer leads to decreased ground temperatures, due to the isolation effect of snow. The timing and duration of snowmelt is more important for the solar radiation balance than snow cover onset in autumn, because during spring the solar elevation is much higher (Ling and Zhang, 2003).

Since the 1960s a decrease of snow cover is observed on a global scale (Fig. 1), (Fig. 2). The two main factors causing the decrease are higher air temperatures and a reduction in sea ice extent and duration. Changes in the atmospheric circulation which were observed around 1980 might also have contributed to the changes in spring snow cover extent (Brown 2000), (Lemke et al. 2007), (Brown and Robinson, 2011). Earlier melt and less spatial coverage of snow emerged and the snow depth might be influenced too by increasing air temperatures (Foster et al. 1996), and rising air temperatures in the Arctic are accredited to anthropogenic influence (Fyfe et al., 2013). The decrease in March snow cover extent from 1970 to 2010 in the northern hemisphere is 11%, compared to pre 1970 values. But snow depth changes are less homogeneous – a decrease south of 40° N and an increase north of 40° N were reported, due to increased precipitation (Peng et al. 2010).

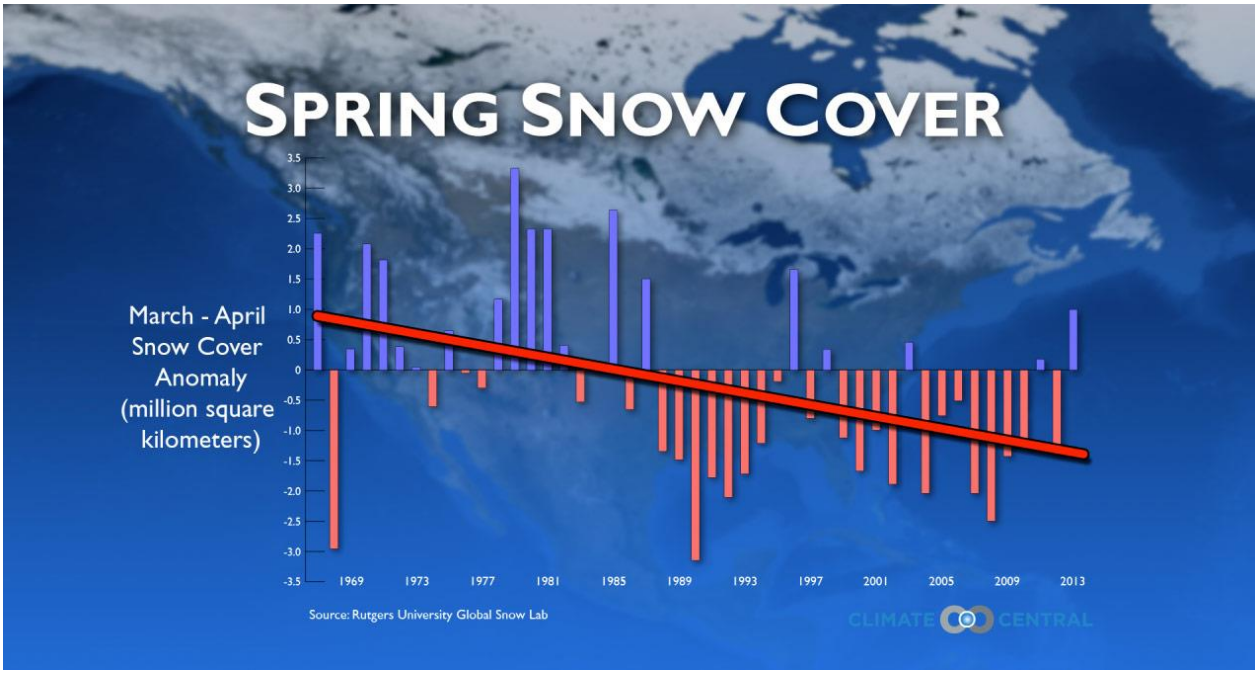


Fig. 1. Northern Hemisphere spring snow cover extent change over time (www.climatecentral.org).

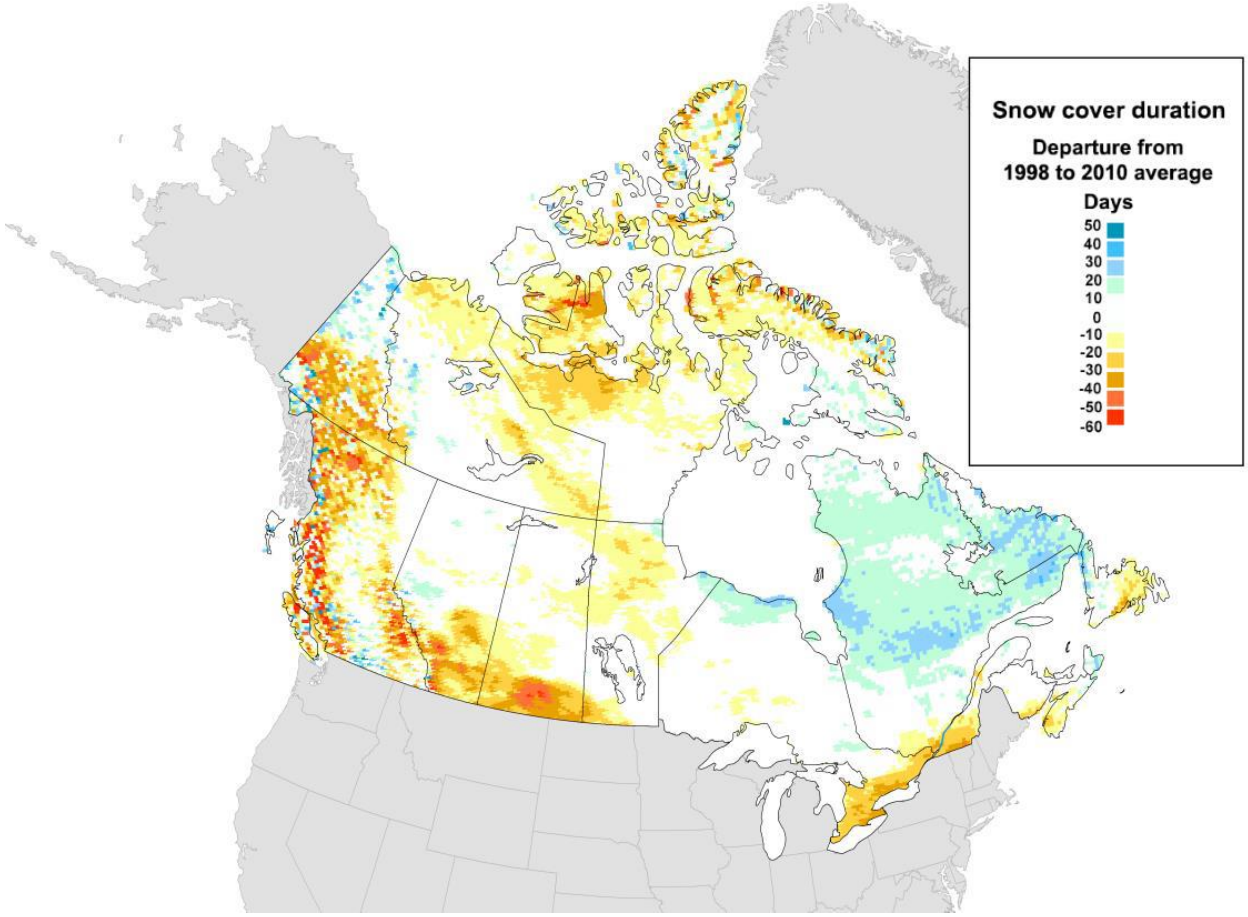


Fig. 2. Snow cover duration changes (1998 compared to 2010) in Canada (Environment and Climate Change Canada, 2018).

Climate change and variability affect the hydrology on a global scale, which drive the need for new knowledge. Climatic and hydrological models need accurate input data of snow water equivalent, snow extent and melt onset (Dietz et al., 2012). For example, earlier melt onsets of sea ice result in more additional melt processes, because of the lower albedo of water compared to ice or snow (Perovich et al., 2007). Natural hazard assessments and flood control use snowmelt data for flood prediction. Bales et al., 2006 highlighted three hydrologic needs for the better understanding: First, the better understanding of energy and water fluxes, second, the feedbacks between hydrological fluxes and ecological and biogeochemical processes and third, enhancing our measurement strategies and information systems. Hydrologic feedbacks control the water availability and influence the vegetation distribution. Furthermore, in an Arctic climate snow absolutely dominates biogeochemical fluxes and influences the global and regional climate. Especially detecting and delineating wet and dry snow is essential in the snowmelt process monitoring, climate research and disaster assessment of snow related hazards (Lemke et al., 2007). Snow and ice cover monitoring in high temporal and aerial coverage is therefore of great importance, which can only be achieved by using remote sensing (Dietz et al., 2012).

## 1.2. Optical properties of snow

### 1.2.1. Optical properties of snow – in the reflective spectrum

Snow has three possible constituents: ice, liquid water and impurities like dust. The spectral reflectance of snow depends on the snow grain size and shape, moisture/ liquid water content, snow depth, impurities, temperature, ice content and the properties of the surface beneath the snow cover (Hall and Martinec, 1985), (Sturm et al., 1995), (Tait 1998), (Kelly et al., 2003), (Foster et al., 2005), (Painter et al., 2009), (Wiscombe and Warren, 1980). The reflectance of snow in the visible range of the electromagnetic spectrum is high – up to 80% or 90% for fresh snow (Winther et al. 1999), (Klein et al. 2000), (König et al. 2001). This reflectance decreases with the age of the snow, because the number of impurities increases over time and melting and refreezing processes increase the grain size (Fig. 3 and 4), (Hall and Martinec 1985). Impurities have an absorption effect, but only in the visible spectrum, where there is a significant different absorption coefficient of ice and dust (Warren and Wiscombe 1980).

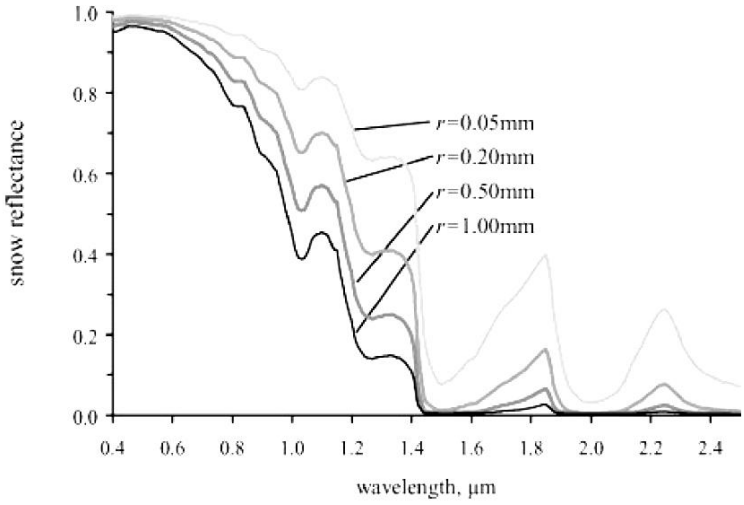


**Fig. 3. Spectral reflectance of pure snow with different grain sizes (Dozier and Painter, 2004).**

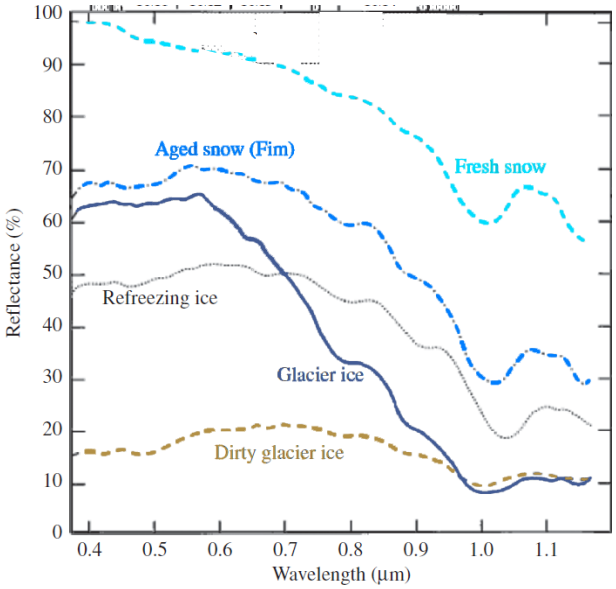


Fig. 4. surface types and their reflectance. Additionally, the band widths of different optical remote sensing instruments are shown; Landsat (TM), MODIS (M) and AVHRR (Zeng et al., 1984, modified by Dietz et al., 2012, modified).

The reflectance of snow in the longer wavelength spectrum is much lower, because ice is highly absorptive in the infrared part of the spectrum (Pepe et al., 2005), (Wang et al., 2005). Ice and water have a very similar absorption coefficient, but ice has a slight shift toward longer wavelengths. Using a hyperspectral sensor, it is possible to estimate the liquid water content in snow by examine this slight shift (Green et al., 2002). Liquid water in snow causes clustering of grains, which behave optically like large grains (Colbeck, 1979). The reflectance in the near infrared decreases in wet snow not because of the liquid water per se, but because of the clustering (Fig. 5). The snow water equivalent is the snow depth multiplied by the snow density. This equivalent only affects the reflectance for shallow snow in the visible part of the spectrum, because in the near infrared, the snow is effectively semi-infinite for a greater depth than 3 cm. Alternatively, in the visible wavelengths the semi-infinite depth is larger, about 50 cm (Fig.6.), (Zhou et al., 2004), (Dozier and Painter, 2004).

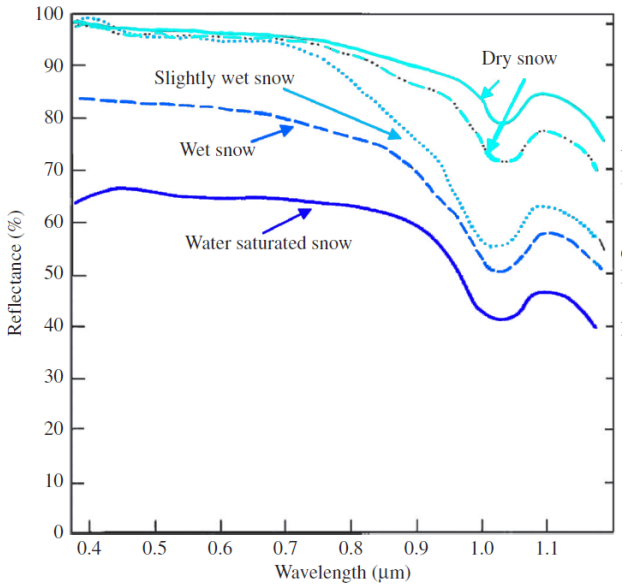


Fig. 5. Reflectance of snow with different liquid water contents (Zeng et al., 1984, modified by Dietz et al., 2012, modified).

Clouds and snow have a very similar reflectance in the visible and thermal range of the spectrum (Fig. 6). Therefore, a delineation of these two classes is difficult using optical remote sensing data (Akyürek and Sorman, 2002), (Miller and Lee, 2005), (Wang et al., 2005), (Hyvärinen et al., 2009), (Hall et al., 2010).

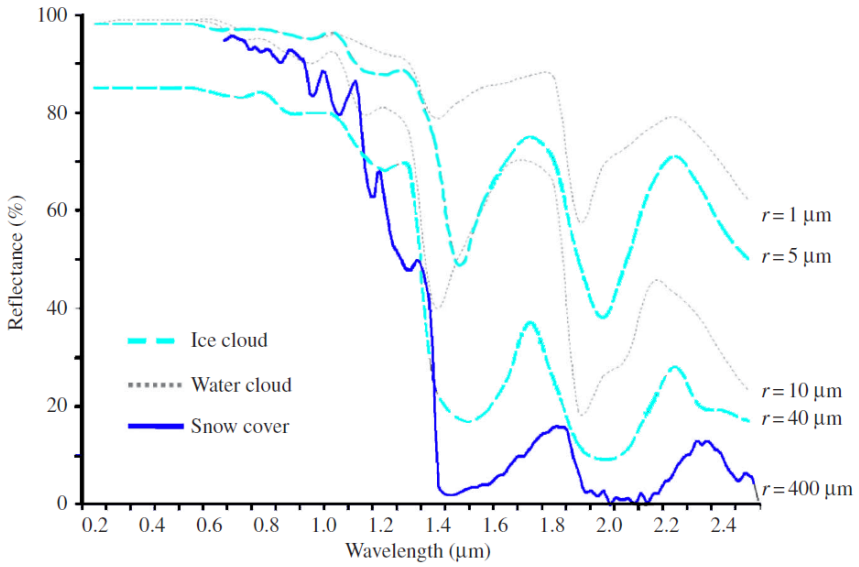


**Fig. 6. Reflectance of clouds compared to snow, where r = particle size (Dozier, 1989, modified by Dietz et al., 2012, modified)**

In the spectral range from 1.55µm to 1.70µm water clouds and snow can be discriminated, because the grain size of snow is higher than the particle size in the clouds. Therefore, most clouds have a higher reflectance in the near infrared than snow (Chang et al., 1987), (Hall et al., 2002). However, ice clouds cannot be delineated from snow easily and a maximum cloud cover of 94% is the upper limit for a successful delineation (Rodell and Houser, 2004). Therefore, in areas of frequent cloud cover it is suggested to use microwave data, which are almost weather independent.

### 1.2.2. Optical properties of snow – in the Earth's passive microwave spectrum

Passive microwave scanning uses the naturally emitted microwaves from the Earth's surface. The emitted microwaves are part of the outgoing longwave radiation in the Earth's energy budget, which are generated from the Earth's temperature (Fig. 7), (König et al., 2001).

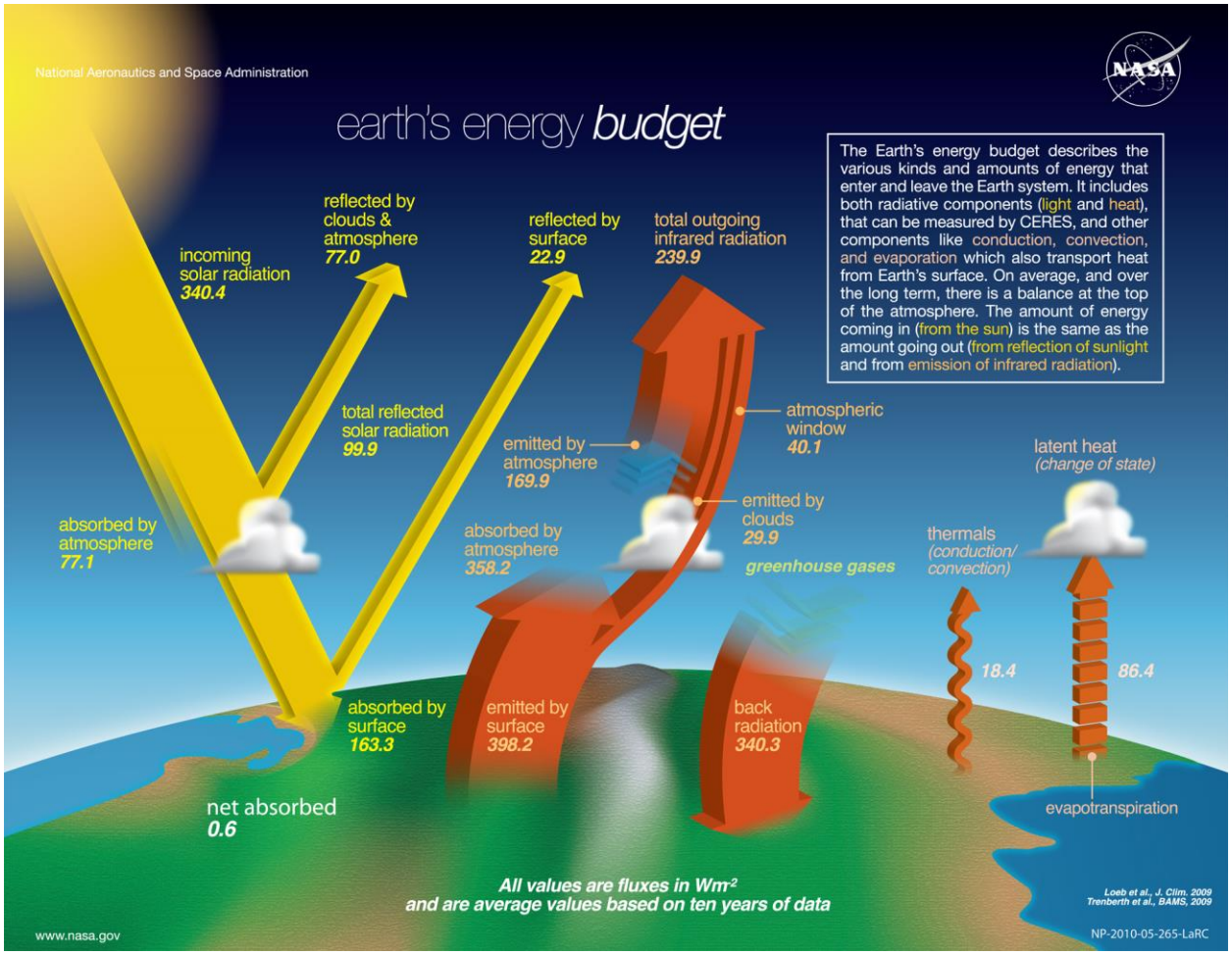


**Fig. 7. Scheme of the Earth's energy Budget with amounts of fluxes (www.climate.nasa.gov)**

The parameter measured with passive microwave sensors is called brightness temperature (Tb) in degrees Kelvin, which is correlated to the physical near-surface temperature as following (Ts):

$$Tb = \varepsilon Ts,$$

where ε is the emissivity of the near-surface snowpack (Zwally and Gloersen, 1977). A higher emissivity leads to a greater measured microwave signal and therefore to a higher brightness temperature. The emissivity increases with a small proportion of moisture, because it makes the snowpack act like a black body, resulting in more emitted energy (Liu et al., 2006). Volume scattering is dominant in dry snow, whereas in wet snow conditions, surface scattering increases due to the moisture. Therefore, a strong increase in the emissivity is observable at the transition from dry to wet snow, because surface scattering is stronger compared to volume scattering (Fig. 8), (Markus et al., 2009), (Ulaby et al., 1986).

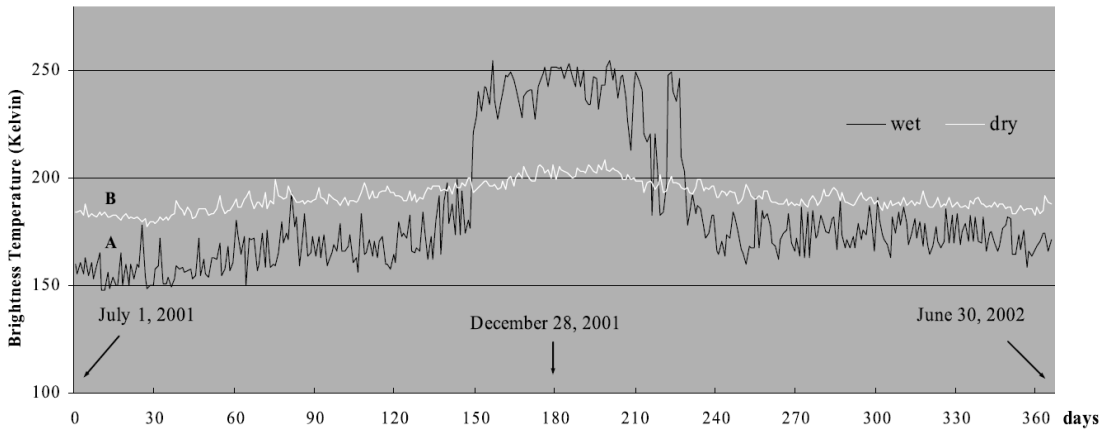


**Fig. 8. Measured brightness temperatures in the Antarctica over one year. Wet snow shows a significant increase in brightness temperature in the summertime. (Liu et al., 2006).**

Microwave radiation is continuously emitted from the Earth's surface, even at night. This radiation can be measured by passive microwave instruments, such as SSMR (Scanning Multichannel Microwave Radiometer), SSM/I (Special Sensor Microwave/ Image), or AMSR-E (Advanced Microwave Scanning Radiometer – Earth Observing System) from space (König et al., 2001) or more recently by the Advanced Scatterometer (ASCAT). The radiation is weakened by snow cover for wavelengths similar to the snow grain size and the weakening is higher with increasing snow coverage (Chang et al., 1987). The dielectric constants of ice and water are very different and the key factors determining the propagation of the microwave through the snow layer. Liquid water in the snow layer increases the absorption of microwaves from the ground beneath significantly. The snow moisture, grain size and shape are the influencing factors on how much of the signal reaches the sensor and therefore the snow depth and the snow water equivalent are the typical snow properties measured with passive microwave sensors (Foster et al., 1999), (Clifford, 2010). Dry snow has a small microwave absorption. Volume scattering occurs by the dielectric discontinuities of snow grains and air contained in the snow layer. Snow depth of dry snow can be estimated by the volume scattering, where a bigger volume of snow causes a greater scattering. However, in wet snow the volume scattering is suppressed. Snow cover mapping is usually done with horizontally polarized data, because vertically polarized data could confuse snow and the underlying dry soils (Amlien, 2008).

Different sensors measure different wavelengths, where a smaller wavelength (= higher frequency) results in a better spatial resolution. But smaller wavelengths lead to a smaller measurable maximum snow depth. The maximum measurable snow depth is equal to 10 – 100 times the wavelength. Therefore, a wavelength of 0.8 cm which is equal to the frequency of 37 GHz, is limited to a maximum measurable snow depth of about 100 cm (Clifford, 2010).

### 1.2.3. Optical properties of snow – interactions with active Radar

Synthetic aperture radar (SAR) is an active system, meaning the sensor sends out electromagnetic waves which are scattered, absorbed or reflected by the Earth's surface. The fraction of the sent-out energy which is scattered back to the sensor is measured. In contrast, like we have already seen before, passive systems use another source of energy, for example optical sensors use the suns radiation as a light source. The main advantage of active systems over passive ones is the time independence. An active system can take images day and night. Furthermore, passive systems are susceptible to light conditions. Shadow effects, for example, are

very variable depending on the daytime and season. These changes in illumination must be corrected in optical images, whereas in SAR images the illumination is coherent (Plank, 2014), (Woodhouse, 2005).

SAR uses electromagnetic waves in the order of microwaves (wavelength of mm to km). These microwaves have a longer wavelength than the shorter electromagnetic waves of the sun. Using these longer waves makes SAR much more independent to atmospheric conditions, like cloud coverage, fog or haze, compared to optical images, because the penetration ability is higher for longer wavelengths. In some areas, this is a crucial property, since cloud coverage can be very frequent, for example in tropical rainforests, or in our area of interest, Ellesmere Island (Woodhouse, 2005).

Using the longer wavelength of SAR makes it possible to measure physical properties of an object. SAR is sensitive to the surface roughness, moisture and to geometrical structures. The rougher the surface is, the brighter it gets imaged in a SAR amplitude scene, because more energy appears at the sensor. For example, a forest is typically brighter in a SAR scene than a flat meadow. Geometrical structures, like buildings will be displayed very bright because of the corner reflection or double bounce effect. The corner reflection takes place when a wave is reflected from the ground onto an object, like a wall, and there again reflected to the sensor (Meier, 1989).

But SAR also has some disadvantages compared to other sensors. SAR holds only a little visual information, because only the amplitude, the phase and the polarization are measured. SAR systems use a sensor which is looking sideways. This constellation is crucial to get a good spatial resolution in SAR images, but it can cause some negative effects (Meier, 2013):

Foreshortening: The slope of a mountain which is headed to the sensor can be imaged shorter than it should be, because the sent signal appeared at the mountain peak earlier than it would without the topography (Fig. 9, b), (Woodhouse, 2005).

Lay-Over: The sent signal can appear at the peak of a tall object earlier than at its base. Therefore, the peak also gets imaged earlier in the SAR scene (Fig. 9, c), (Woodhouse, 2005).

Shadow: Objects or the topography can prevent the wave propagation. Everything located behind such objects in the line of sight of the sensor is not seen and not imaged (Fig. 9, d), (Woodhouse, 2005).

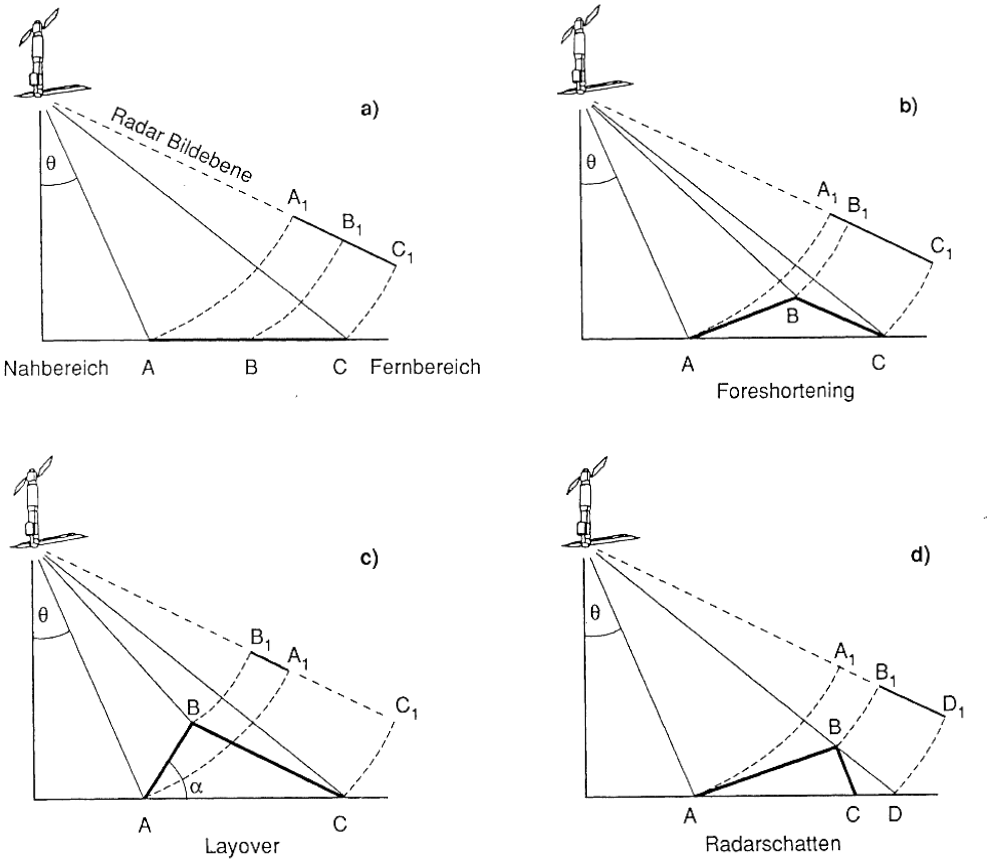


**Fig. 9. Acquisition of a SAR scene without topography a), Foreshortening b), Layover c) and shadow d) graphically represented (Meier, 1989).**

Especially in rough terrain these effects can cause big problems. In such areas, it is recommended using data which was captured by using a steeper incidence angle to reduce the effects (Bhattacharya und Mukherjee, 2017).

When using active microwaves only wet snow detection is reliable (Wang et al., 2008). The ground underneath dry snow scatters most of the incoming radiation back and not the snow itself, because of the high penetration capability of SAR (König et al., 2001). Liquid water in snow reduces the penetration depth and the backscatter coefficient. The C-band penetration depth of dry snow is typically 20m (one-way), but for wet snow with 5% liquid water content less than 3cm (Fig. 10), (Nagler et al., 2016).

The occurrence of liquid water in the snowpack of multiyear sea-ice also results in a decreased backscatter (Winebrenner et al., 1994), but for first year ice (FYI) the backscatter increases, because an increased snow grain size and brine volume increases the dielectric constant, resulting in more volume scattering (Barber, 2005).

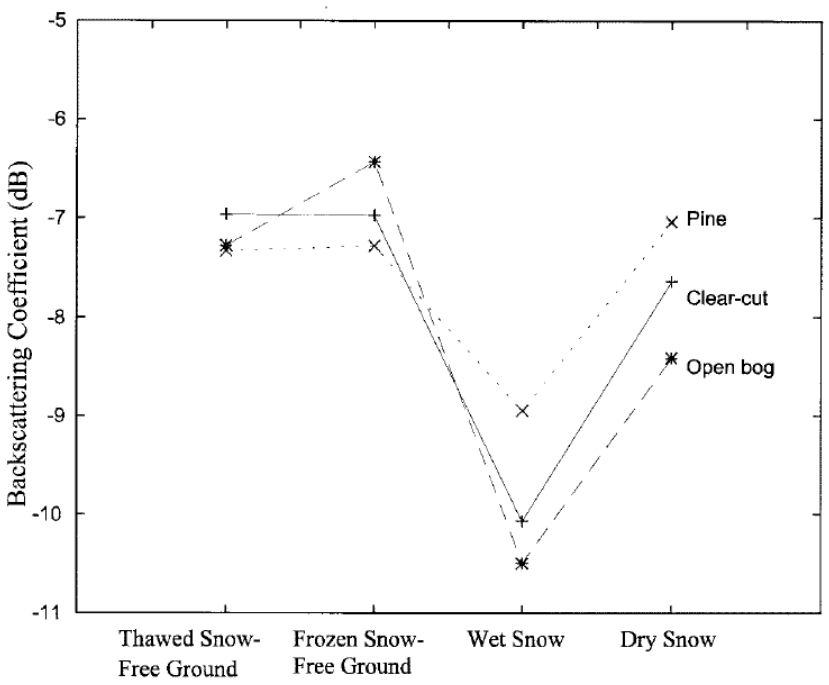


**Fig. 10. SAR averaged backscatter coefficients of the ERS-1 Satellite sensor for different snow conditions and land surface types (Koskinen et al., 1997).**

Scatterometers are active microwave instruments with a high temporal resolution due to the big swath, and can be used to detect ice layers in a snowpack (Nghiem et al., 2005), or snow melt onset (Foster et al., 2011). However, their spatial resolution is low compared to SAR but higher than the PM's resolution (König et al., 2001).

The weather independence of SAR and other microwave instruments is crucial to find snow melt onset and ending, because often these tipping points cannot be found exactly due to cloud cover when using optical images (Stettner et al., 2018). Schweiger 2004, stated that the Arctic sea has a cloud cover frequency of up to 81%. Furthermore, sunlight availability is crucial for optical images, but absent in an Arctic region for a major part of the year.

In summary, SAR remote sensing has a high penetration capability, which allows to delineate wet snow from other land types at any weather conditions, any daytime, and regardless of the solar illumination conditions. Furthermore, SAR is very sensitive to surface moisture variability. But problems can occur in areas of rough topography due to the acquisition behavior of SAR (Robinson et al., 1984).

## 1.3. History of snow mapping with microwave instruments

In the 1960's it was possible to map snow from space for the first time with the TIROS-1 satellite (Lucas and Harrison, 1990). In the 1970's it was shown that X-band and C-band SAR are capable of mapping wet snow (Mätzler and Schanda, 1984).

Since 1979, passive microwave (PM) brightness temperature observations are available. Due to their high temporal resolution, PM instruments became the best candidate to detect the transition from dry to wet snow and are still the most widely used sensors (Drobot and Anderson, 2001), (Belchansky et al., 2004), (Markus et al., 2009), (Bliss and Anderson, 2014). However, their spatial resolution is limited to 10 - 25 km.

In 1994 Shi and Dozier studied the backscatter, the polarization and frequency ratios of snow in SIR/-C/X-SAR. One year later, they inferred snow wetness using C-band SAR (Shi and Dozier, 1995). In 1997 they came up with a supervised classification algorithm, using a classification tree. Inputs are intensity, polarization properties and frequency ratios, also allowing to delineate wet from dry snow (Shi et al., 1994), (Shi and Dozier, 1997). But most SAR instruments are single-frequency types. After the repeat-pass sensors ERS-1, JERS-1 and RADARSAT-1 the monitoring of snow has become practical by using the change detection method. Change detection is the comparison of a scene with another scene of the same area and with the same sensor at a different acquisition time (Nagler, 1996), (Koskinen et al., 1999), (Nagler and Rott, 2000). Later also polarimetric SAR data was available with the instruments ENVISAT ASAR, ALOS PALSAR and RADARSAT-2. Better classification results were achieved using the polarimetric information. But detecting shallow dry snow is still a difficult task using C-band SAR, because it can penetrate more than 10m of dry snow (Park et al., 2014), (Ulaby and Moore, 1982). This problem can be solved by using the interferometric coherence between two repeat passes. Snow-free surfaces preserve the coherence, whereas a snow-covered surface has a lower coherence. Therefore, a threshold for the coherence can be applied to delineate snow from non-snow surfaces (Shi et al., 1997), (Kumar and Venkataraman, 2011). But detecting the exact time of melt onset, for example, was still a very difficult task using SAR, because of the lower temporal resolution compared to PM (Howell et al., 2018).

Since 2000 scatterometer backscatter measurements are available with a daily global temporal resolution, like for PM instruments. In contrast to PM, scatterometer have a better spatial resolution of (~2-5 km) and several methods are available to detect wet snow (Nghiem and Tsai, 2001), (Howell et al., 2006), (Wang et al., 2011), (Mortin et al., 2012), (Mortin et al., 2014).

C-band SAR would still hold a better spatial resolution of 20-100m and is therefore in the focus of today's research. The challenge nowadays is still to get a high temporal resolution using SAR. Furthermore, the viewing geometry, if inconsistent, can be a limiting factor (Howell et al., 2018).

In 2014 and 2016 the satellites Sentinel-1A and Sentinel-1B were launched. These two satellites acquire SAR images with a high spatial resolution (5 x 20m in IW mode) of the Earth's whole land surface every 6 days. The data is open source and can be used as a powerful tool in snowmelt monitoring (Nagler et al., 2016), (www.earth.esa.int). Stettner et al., 2018 used TerraSAR-X data to generate snow cover maps for the Arctic region Herschel Island, because no operational product was available in both high temporal and spatial resolution. TerraSAR-X has a revisiting time of 11 days and uses an X-Band SAR sensor. The X-Band is less sensitive to snow moisture, but better suited in mapping dry snow.

For the detection of wet snow, the C-band Sentinel-1A and 1B hold a great potential. The combination of the Sentinel-1A and 1B SAR images with RADARSAT2 SAR images can provide a high temporal resolution with a high spatial resolution as well. Howell et al., 2018 showed this potential in the Arctic by estimating melt onset for sea ice. The foundation which made the combination of different sensors, passes and viewing geometries possible is the concept of normalized gamma naught (Small, 2011), (Small, 2012).

The upcoming RADARSAT Constellation Mission in 2019 consists of three C-band SAR satellites. These satellites will provide additional SAR images, especially of the Arctic, which can be included in the $\gamma_c^0$ backscatter composites to improve their quality and the temporal resolution (www.asc-csa.gc.ca), (Howell et al., 2018).

## 1.4. Study area

Ellesmere Island is the most mountainous and northerly island of the Canadian Arctic Archipelago (CAA) (Fig. 11). It has an area of 196'236 $km^2$ and it is the largest of the Queen Elizabeth Islands and the 10$^{th}$ largest island in the world. Ellesmere Island is located in Nunavut. The Kane Basin and Kennedy Channel, respectively the Nares Strait separate the island from Greenland. Barbeau Peak is the highest point of the island with an elevation of 2616 m a.s.l. (White and Copland, 2018), (www.thecanadianencyclopedia.ca).

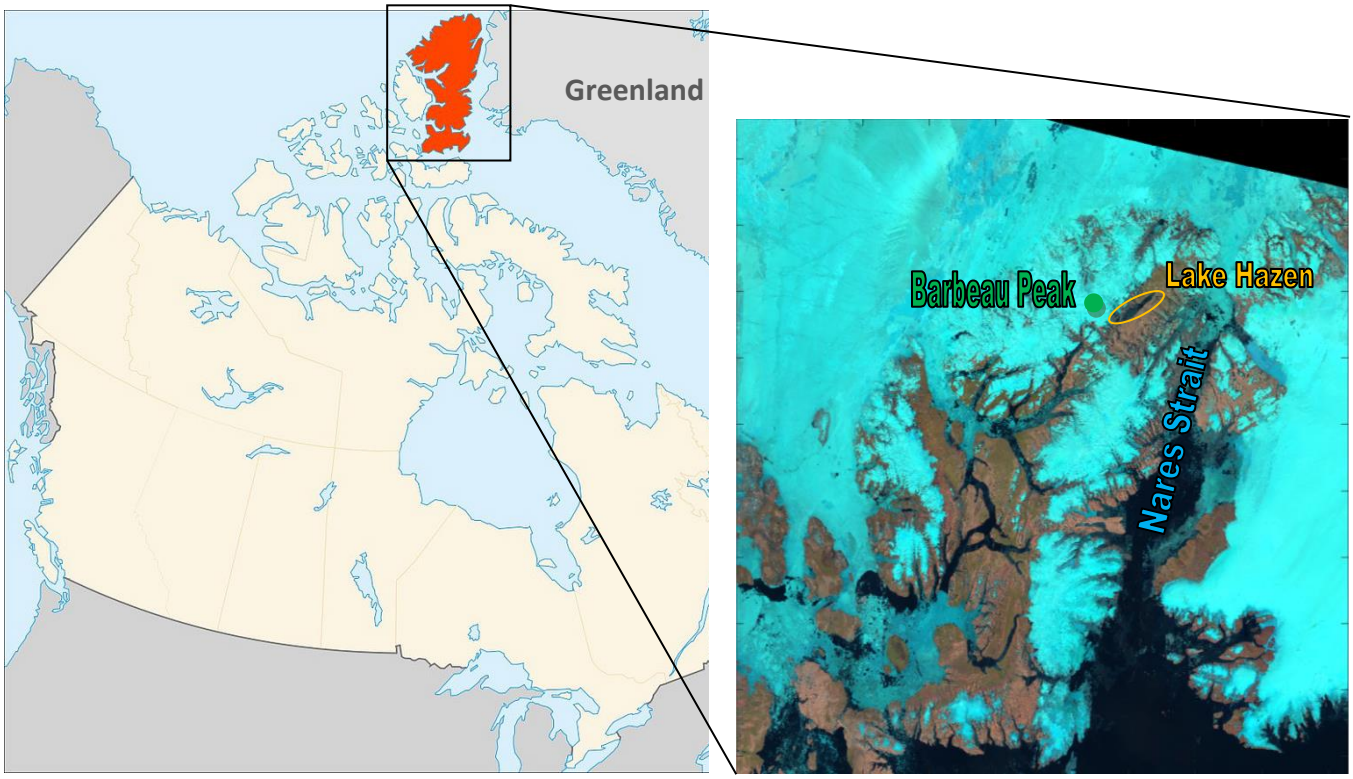


**Fig. 11. Left: Map of the Ellesmere Island (Canada) (www.flickr.com, modified), Right: MODIS composite image false color (R= SWIR, G= NIR, B=RED), from 01.08.2017 to 11.08.2017 (Trishchenko, 2017).**

The coast has a high frequency of fog and cloud coverage, due to varying sea ice extent. The lowland interior of the island is surrounded by mountains. The interior has a low mean precipitation because the surrounding mountains capture the most precipitation (Maxwell, 1981). Between 1961 and 2007 the monthly mean precipitation rates measured at the Eureka weather station ranged from 1.8 mm in late winter to 12 mm in July. Over this period, an increase of 10% in the mean annual precipitation rates was observed (Lesins et al., 2010). The mean air temperature measured in this period was -19.1 °C (White and Copland, 2018).

Ellesmere Island is a polar desert with sparse vegetation (Fig. 12). But the flora is quite diverse for such an environment, holding 151 species of moss for example. The fauna of Ellesmere Island holds small herds of muskoxen, a small caribou herd and several bird species and other land mammals. At Lake Hazen, the summers are quite warm compared to the rest of the island. At the Tanquary Fiord the average frost free period is 55 days (www.thecanadianencyclopedia.ca).

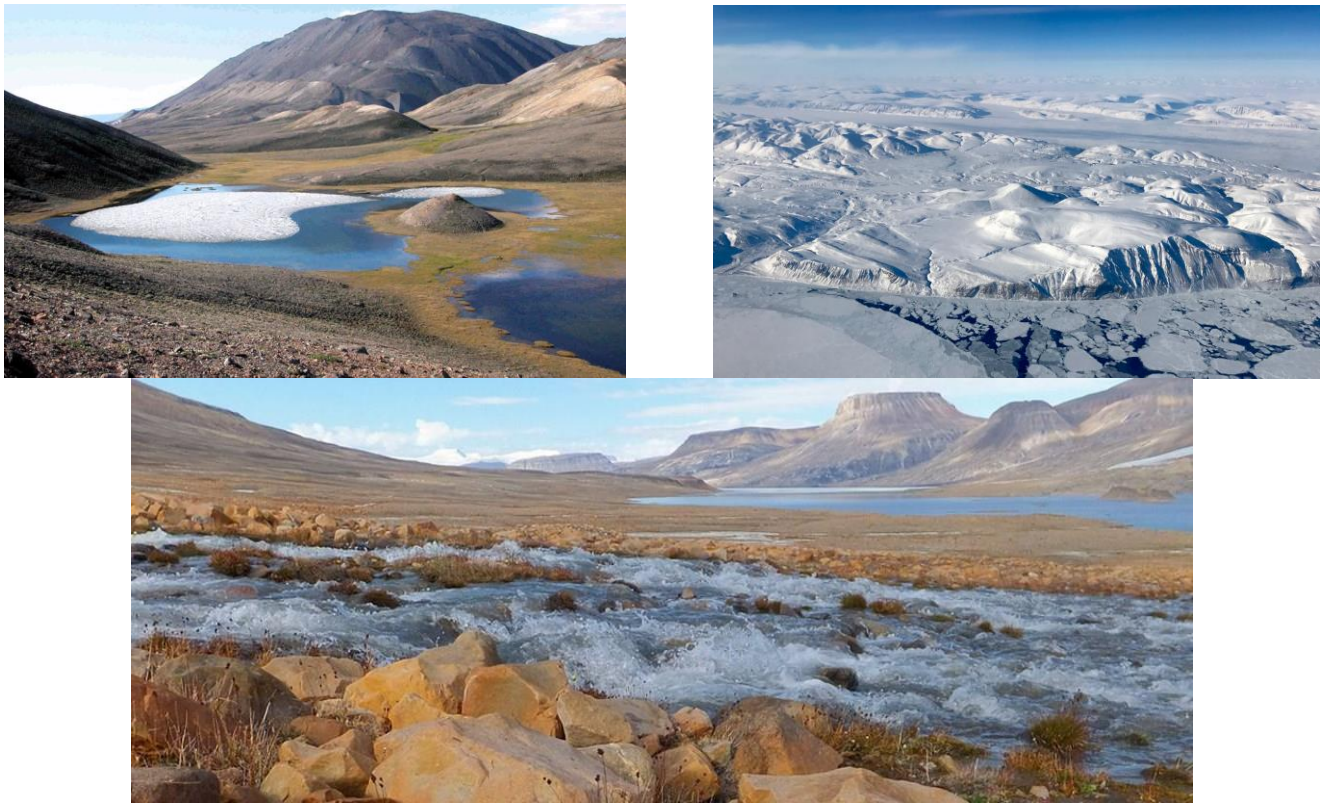

Fig. 12. Impressions of the Ellesmere Island's landscape (www.cruisemapper.com), (www.espo.nasa.gov).

One reason of investigating this area is the abundance of Sentinel-1A, Sentinel-1B and RADARSAT-2 images. In Arctic regions, the coverage of sun-synchronous satellites is in general higher, resulting in a higher number of overlapping images (Stettner et al., 2018). Furthermore, the rough terrain of Ellesmere Island makes it a perfect candidate for investigating the advantages of the higher spatial resolution held by SAR instruments (Howell et al., 2018).

## 1.5. Research questions

The main goal of this study is to compare different snow and ice melt products derived from three different Instruments (SAR, scatterometer and passive microwave). Passive microwave sensors are the most widely used to detect melt onset (e.g. (Drobot and Anderson, 2001), (Belchansky et al., 2004), (Markus et al., 2009), (Bliss and Anderson, 2014)). Scatterometers, an active microwave instrument with a real aperture are used quite often too for this task (e.g. Howell et al., 2006), (Wang et al., 2011), (Mortin et al., 2012), (Mortin et al., 2014)). Both these instruments are commonly used, because they have a daily global coverage. On the other hand, their low spatial resolution limits the detection of melt onset and end to large study areas. Small scale analysis is therefore almost impossible, especially in coarse topographies. SAR instruments on the other hand, can provide images with a much higher spatial resolution. The use of SAR scenes to detect melt onset and end was mostly limited to the temporal resolution, where most SAR sensors have a revisiting time of several days. Furthermore, different viewing angles had to be considered, often leading to exclusions of scenes and therefore to an even worse temporal resolution (Howell et al., 2018). These disadvantages can be overcome with the concept of $\gamma_c^o$, where terrain-corrected SAR scenes can be combined from different sensors (Small, 2011), (Small, 2012). This concept can increase the temporal resolution significantly, depending on the number of instruments available. A lot of studies focused on glacier changes or sea ice changes (see for example (White and Copland, 2018) or (Howell et al., 2018). Fewer studies focused on land area snow melt, especially in an Arctic area, where this study will focus on. Moreover, the studies addressing melt with active microwave in-

struments on land areas are often focusing just on melt onset but not on melt end and the number of melt days.

The main questions addressed in this study are:

- How well can we detect melt onset, end and the number of melt days using $\gamma_c^o$ backscatter SAR scenes compared to the often used scatterometer and passive microwave instruments?
    - Do the SAR HH and HV polarizations make any difference and if yes, how?
- How plausible are the results when we compare them to auxiliary data, such as temperature data?
- What advantages and disadvantages does each instrument offer considering the task of detecting wet snow and melt onset, end and the number of melt days?

## 1.6. Hypothesis

It is assumed that active SAR performs well in finding the melt onset and endings, but the temporal resolution could still be a problem, even when using $\gamma_c^o$ backscatter composites. Passive microwave instruments are considered to be more robust against the influence of different land cover types when detecting wet snow. The lower spatial resolution of passive microwave instruments and scatterometers compared to SAR instruments will probably be a big problem, concerning the mountainous terrain of Ellesmere Island (Nagler and Rott, 2000).

# 2. Data

Several instruments and datasets were used in this study. An overview is shown in table 1.

Tab. 1. Data used in this study and possible alternatives. Datasets not used in this study are marked with *.

| Sensor type/ Instrument | Spatial resolution | Temporal resolution | Temporal coverage | Observable |
|---|---|---|---|---|
| Sentinel-1 (SAR) | **< 0.4 km** | Nearly daily | 2014 - | C-band ~ 5.3 GHz Backscatter |
| RADARSAT-2 (SAR) | **< 0.4 km** | | 2007 - | C-band ~ 5.3 GHz Backscatter |
| ASCAT (Scatterometer) | 4.45 km | **daily** | 2007 - | C-band ~ 5.3 GHz Backscatter |
| AMSR2 (PM) | 10 km | **daily** | 2012 - | 6, 7, 10, 18, 23, 36, 89 GHz Brightness Temperature |
| AMSR-E (PM) * | 10 km | **daily** | 2002 | 7, 10, 19, 23, 37, 89 GHz Brightness Temperature |
| FY-3C (PM) * | 10 km | **daily** | Sept. 2013 - | 10, 19, 23, 37, 89 GHz Brightness Temperature |
| PMW algorithm (sea ice melt derived from PM) | 25 km | yearly | 1979 - | - |
| ERA5 | 0.25 ° | hourly | 2008 - | - |
| MODIS TOA level-3 reflectance (optical sensor) | 400 m | 10 days | 2000 – 2017 | 0.620 – 0.670 µm VIS (Red)<br>0.841 – 0.876 µm NIR<br>0.459 – 0.479 µm VIS (Blue)<br>0.545 – 0.565 µm VIS (Green)<br>1.230 – 1.250 µm NIR<br>1.628 – 1.652 µm SWIR<br>2.105 – 2.155 µm SWIR |
| MODIS land surface temperature (MOD11C1) (optical sensor) | 0.05 ° | daily | 2000 - | Day Land surface Temperature [Kelvin] |

## 2.1. Passive microwave Imagery

Passive microwave (PM) data was used from the satellite GCOM-W1 with the AMSR2 instrument onboard. The FY-3C satellite with the MWRI instrument was hold as a backup alternative, but was not used in the end.

### 2.1.1. AMSR2

The GCOM-W1 satellite was launched in 2012 and is operated by Japan Aerospace Exploration Agency (JAXA). The orbiting altitude is 700 km producing images with a 1450 km swath width (Fig. 13). Seven bands are available, with the spatial resolution depending on the frequency. Higher frequencies generally have better spatial resolution (Tab. 2).

Tab. 2. AMSR2 band configuration and their corresponding spatial resolution (www.remss.com).

| Band [GHz] | Polarization | Spatial Resolution (3-dB footprint size) [km x km] |
|---|---|---|
| 6.93 | V,H | 62 x 35 |
| 7.3 | V,H | 62 x 35 |
| 10.65 | V,H | 42 x 24 |
| 18.7 | V,H | 22 x 14 |
| 23.8 | V,H | 19 x 11 |
| 36.5 | V,H | 12 x 7 |
| 89.0 | V,H | 5 x 3 |

Level-3 products are also available where all bands have a spatial GSD of 10 km. These data can be downloaded at www.gportal.jaxa.jp (www.remss.com).

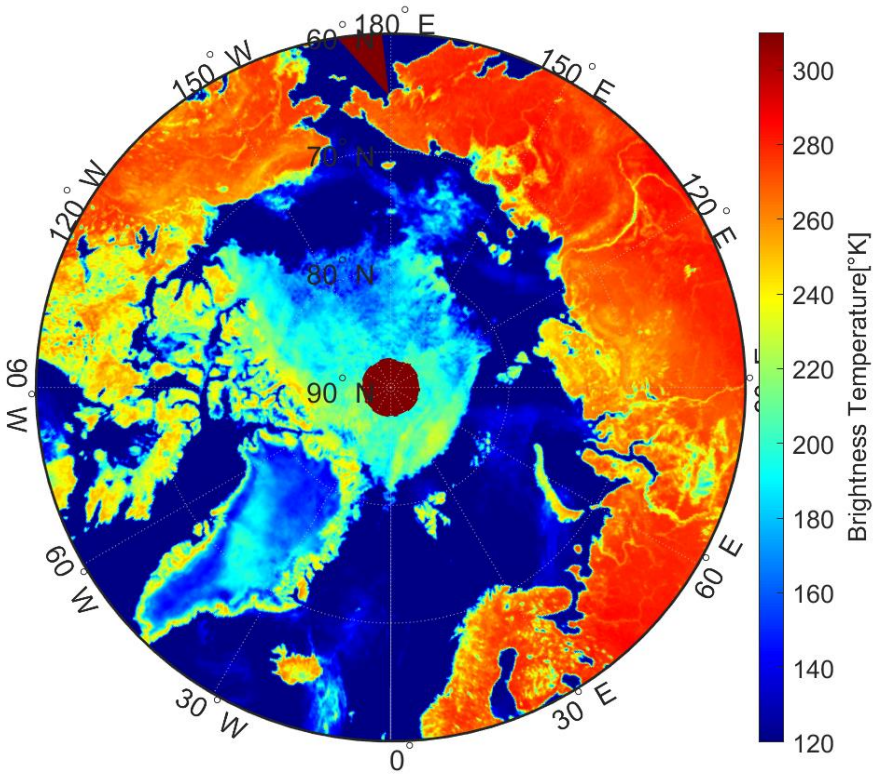


Fig. 13. Brightness temperature at the 19 GHz band measured with the AMSR2 sensor. The image shows the northern hemisphere on the 31.08.2018.

### 2.1.2. FY-3C/ MWRI

The FY-3C satellite was launched in 2013 and is operated by the China Meteorological Administration (CMA). The sun-synchronous satellite orbits the Earth at an altitude of 836 km. Bands are available at 10, 19, 23, 37 and 89 GHz. The spatial resolution is similar to AMSR2; 10 km (www.wmo-sat.info). Data from the FY-3C satellite were not used in this study, but could become important in the future, when the older AMSR2 sensor will

stop working. Due to the similar band configuration and the similar spatial resolution as to AMSR2 sensor, the MWRI instrument is the best candidate to replace AMSR2 data (Liu et al., 2018).

### 2.1.3. PMW algorithm data

The Passive Microwave (PMW) algorithm uses SSM/I data and multiple indicators to detect melt onset and end of sea ice. Maps are available every year from 1979 to (currently) 2017. The data has a spatial resolution of 25 km and can be downloaded at https://neptune.gsfc.nasa.gov/csb/ (Markus et al., 2009).

## 2.2. Scatterometer Imagery

Scatterometer Instruments are active microwave instruments that measure radar backscatter, but in contrast to SAR they use a real aperture. In this study the ASCAT instrument was used.

### 2.2.1. ASCAT

The Advanced Scatterometer (ASCAT) is operated by EUMETSAT and has delivered products since 2007. The data can be downloaded e.g. at http://www.scp.byu.edu/data/Ascat/. The dataset *Scatterometer Image Reconstruction (SIR)* uses VV polarization and combines ascending and descending passes. The spatial resolution of ASCAT images is 4.45 km. The acquisitions' incidence angle is approximately 40° (Fig. 14), (Early and Long, 2001).

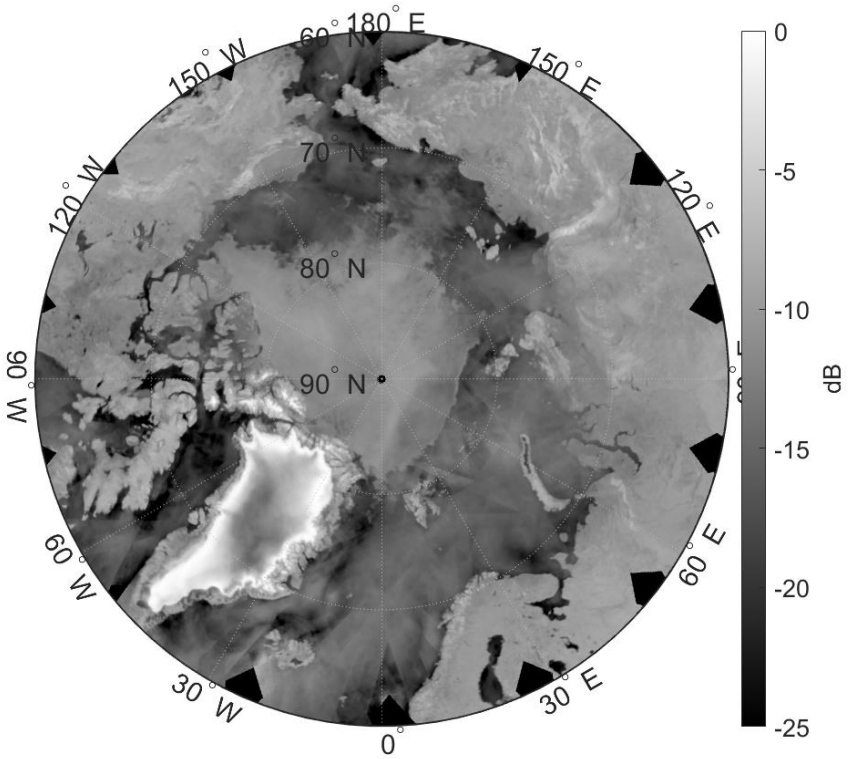


**Fig. 14. An example of an ASCAT composite backscatter image over the northern hemisphere. The image was acquired on 31.08.2015.**

## 2.3. SAR Imagery

Three radar satellite platforms Sentinel-1A/ 1B and RADARSAT-2 were used in this study. These platforms deliver Synthetic Aperture Radar (SAR) data.

### 2.3.1. Sentinel-1A/B

The two satellites Sentinel-1A and Sentinel-1B are operated by the European Space Agency (ESA). Sentinel-1A was launched in 2014, 1B in late 2016. Their orbit is sun-synchronous at an altitude of 693 km. The center frequency of the sensors on board is 5.405 GHz, which corresponds to C-band. The sensors are able to measure at HH, VV, HV and VH polarizations. The spatial resolution varies between 5m for 80 km swaths and 40m for 400 km swaths (www.earth.esa.int).

### 2.3.2. RADARSAT-2

RADARSAT-2 is operated by the Canadian Space Agency (CSA) and was launched in 2007. Like the Sentinel satellites, RADARSAT-2 has a sun-synchronous orbit and a C-band, full polarimetric, SAR instrument. The orbital altitude is 798km. The spatial resolution varies between 1 m and 100 m, the swath width between 18 km and 530 km (www.asc-csa.gc.ca).

### 2.3.3. Normalized gamma naught ($\gamma_c^0$) backscatter composites

To improve the interpretability of SAR scenes, and integrate data from multiple SAR sensors and orbital tracks, the SAR data was terrain flattened using the concept of gamma naught (Small, 2011). This requires accurate knowledge of the acquisition geometry of the SAR scenes and a digital elevation model (DEM). The images were radiometric terrain corrected (RTC), by simulating the local illuminated area using the DEM. After applying the radiometric terrain correction, the influence on backscatter of the terrain was removed, allowing us to better investigate the weaker thematic land cover induced backscatter differences. Afterwards it is possible to generate local resolution weighting (LRW) images, where each contributing image in the composite is weighted according to its local resolution. Therefore, different SAR images from different sensors (Sentinel-1 and RADARSAT-2) and with different incidence angles can be combined to a single scene. The SAR images used in this study were processed at the Remote Sensing Laboratories (RSL) of the University of Zurich to $\gamma_c^0$ composites/ LRW image (Fig. 15), (Fig. 16), (Small, 2011), (Small, 2012).

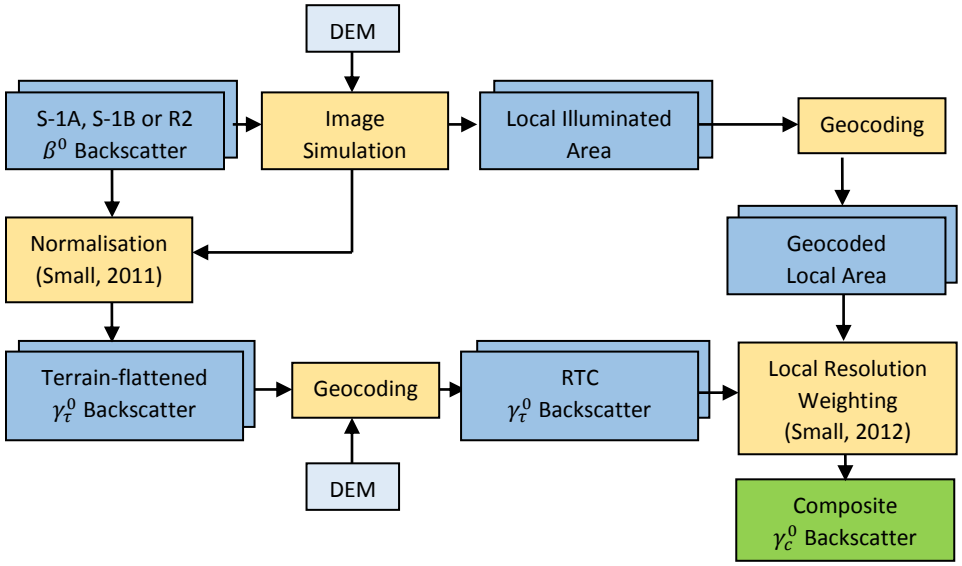


Fig. 15. Processing chain for construction of LRW/ $\gamma_c^0$ backscatter images

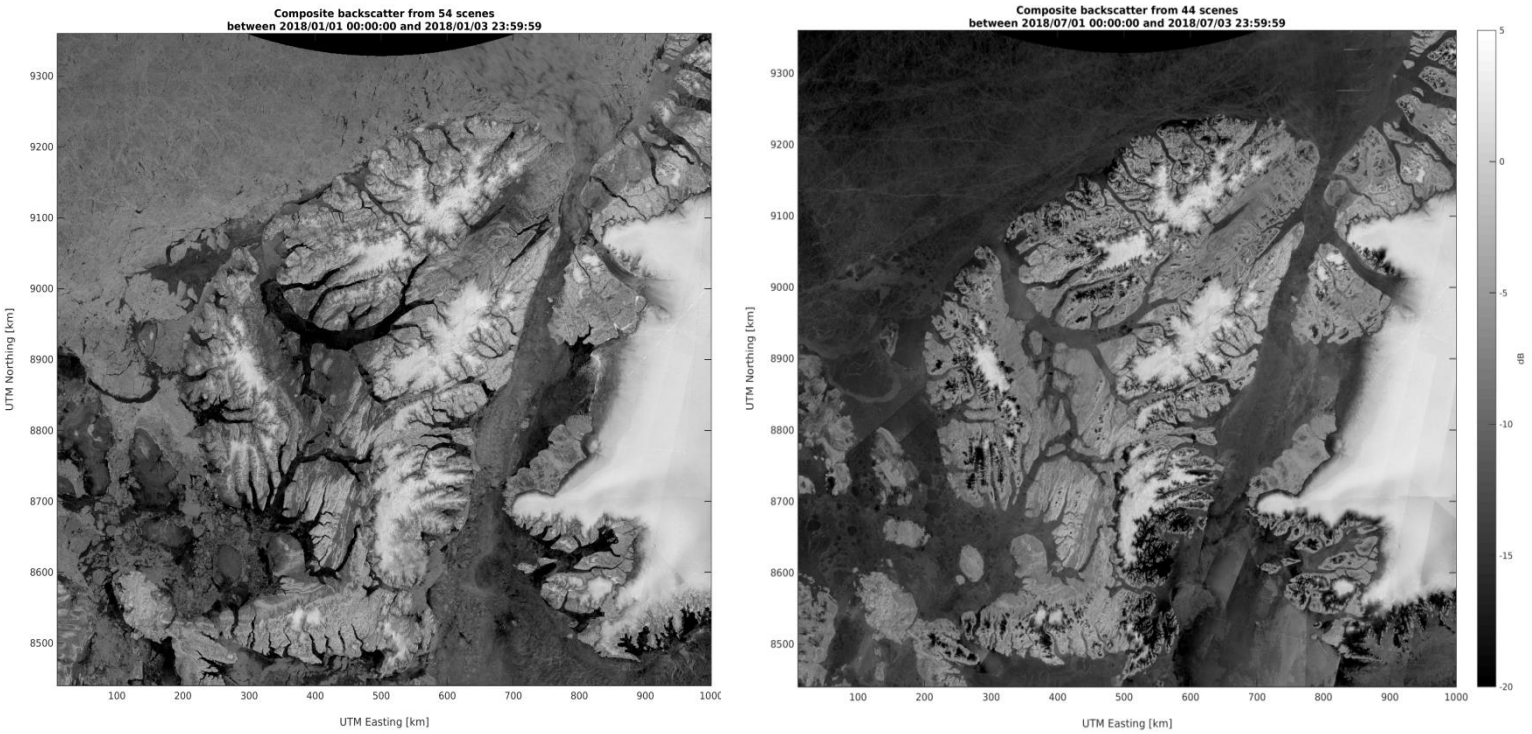


**Fig. 16. Two examples of SAR LRW/ $\gamma_c^0$ HH backscatter images. Left: The image was acquired between 01.01.2018 and 03.01.2018 showing Ellesmere Island in winter. Right: The image was acquired between 01.07.2018 and 03.07.2018 showing Ellesmere Island in summer. Contains modified Copernicus Sentinel data (2018). RADARSAT-2 Data and Products ©MacDonald, Dettwiler Associates Ltd. (2018) – All Rights Reserved. RADARSAT is an official trademark of the Canadian Space Agency.**

Different SAR composites were available, ranging from 1 day composites to 10 day composites in HH or HV polarization.

## 2.4. ERA5 products

ERA5 products are generated by the European Centre for Medium-Range Weather Forecasts (ECWMF). These products are modeled globally with historical data and weather measurements (www.cds.climate.copernicus.eu).

### 2.4.1. Temperature estimates 2m above ground

The ERA5 temperature estimates 2m above ground is used as an air temperature indicator, spatially interpolated to a complete global product (www.cds.climate.copernicus.eu). The data is available hourly, where here the data from 14:00 local time were used, assuming it to be the maximum daily air temperature.

### 2.4.2. Snowmelt estimates

The ERA5 snowmelt product estimates the liquid water content in the snow, spatially interpolated at low resolution to a complete global product (www.cds.climate.copernicus.eu).

### 2.4.3. ECWMF Sea ice concentration

The ECWMF product “sea ice monthly and daily gridded data from 1978 to present” contributes sea ice concentration in percent with a spatial resolution of 12.5km (www.cds.climate.copernicus.eu).

## 2.5. Optical imagery

The Moderate Resolution Imaging Spectro-Radiometer (MODIS) provides optical satellite images. The MODIS sensor is onboard the two satellites Aqua and Terra, operated by NASA. In 1999 the satellite Terra was

launched and in 2002 Aqua. The entire Earth's surface can be imaged every 1 to 2 days from a sun-synchronous orbit at 705km altitude with a 2330km cross-track swath. 36 spectral bands acquire data with a spatial resolution between 250m and 1000m (www.modis.gsfc.nasa.gov).

### 2.5.1. CCRS MODIS top of atmosphere (TOA) reflectance data

The Canadian Centre for Remote Sensing (CCRS) processed MODIS reflectance data to 10 day TOA cloud-free and shadow-free composites. These composites are available for 2000 to 2017 and have spatial resolutions of 250m and 400m (Trishchenko, 2017).

### 2.5.2. MODIS land surface temperature data (MOD11C1)

MOD11C1 is a MODIS derived product containing surface temperature and emissivity. The spatial resolution is 0.05° covering the whole of the Earth's surface every day. In contrast to the ERA5 temperature estimate product, the MODIS LST product has a 5 times better spatial resolution. The temperature is derived from measured emissivity values. The temperature is also dependent on the land cover classes, similar to the PM brightness temperatures. MODIS temperature values are therefore not necessarily representing physical surface temperature, which has to be kept in mind. Nevertheless, the accuracy is 1°K for materials with known emmissivities (Wan et al., 2015).

### 2.5.3. MODIS Land surface type (MCD12C1)

MCD12C1 is a MODIS derived product containing land surface classification. The spatial resolution is 0.05°. Images are available once per year, where in this study the most recent product (year 2017) was used (Fig. 17), (www.lpdaac.usgs.gov).

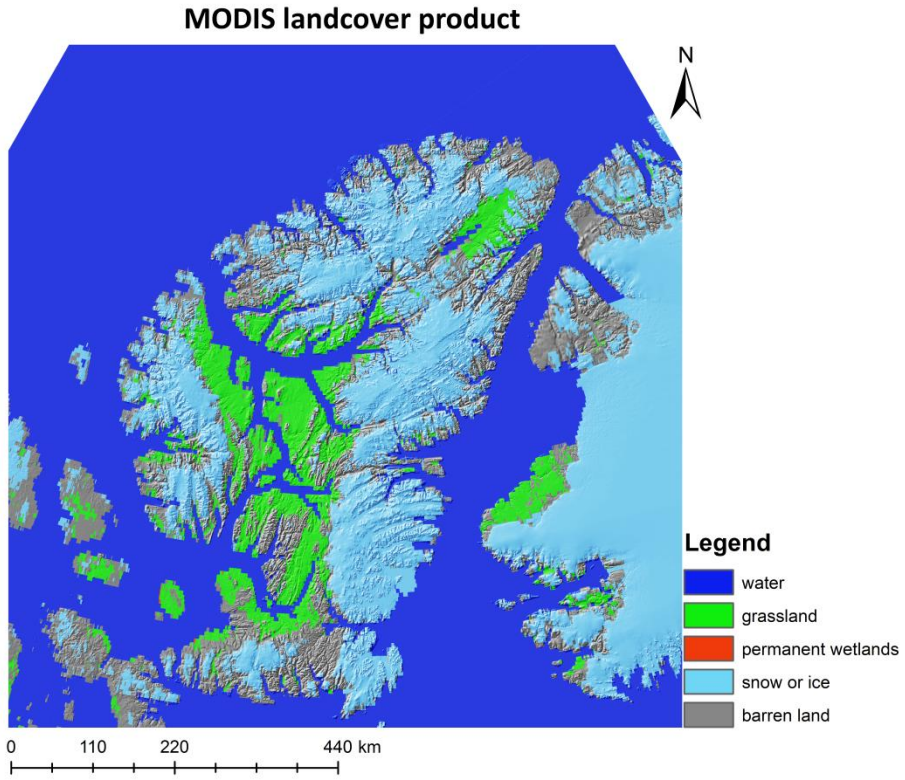


Fig. 17. MODIS landcover product shown for Ellesmere Island. In the background, a shaded relief image was used for illustration.

## 2.6. Auxiliary Data

Several auxiliary data were used in this study, such as digital elevation models, and weather data from different stations on Ellesmere Island.

### 2.6.1. Weather data

Weather data was used from the three weather stations Alert, Eureka and Grisefiord (Fig. 18). The daily maximum, minimum and mean air temperatures were available. The data can be downloaded at www.climate.weather.gc.ca.


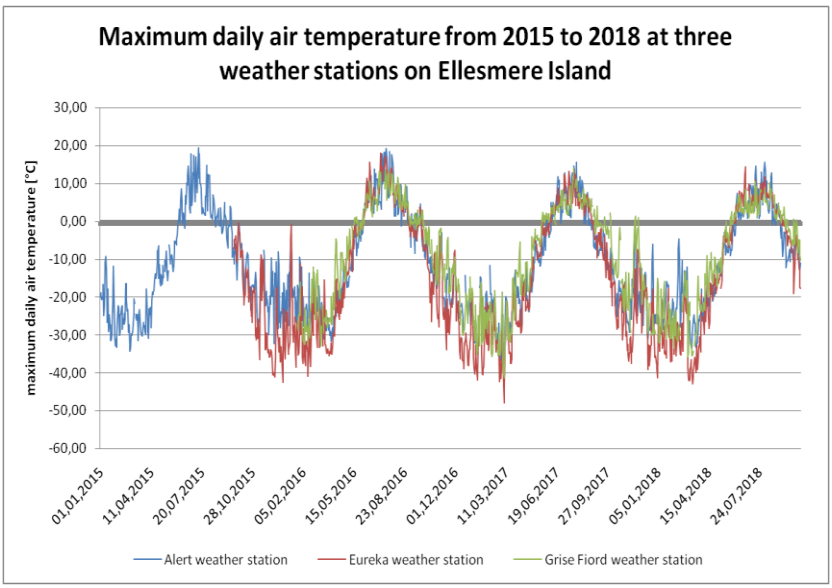


**Fig. 18. Left: Location of the three weather stations used in this study. Right: Maximum daily air temperature measured at the three stations (www.earth.google.com), (www.climate.weather.gc.ca).**

Since 2016 also snow depth measurements were available for all three weather stations (Fig. 19).

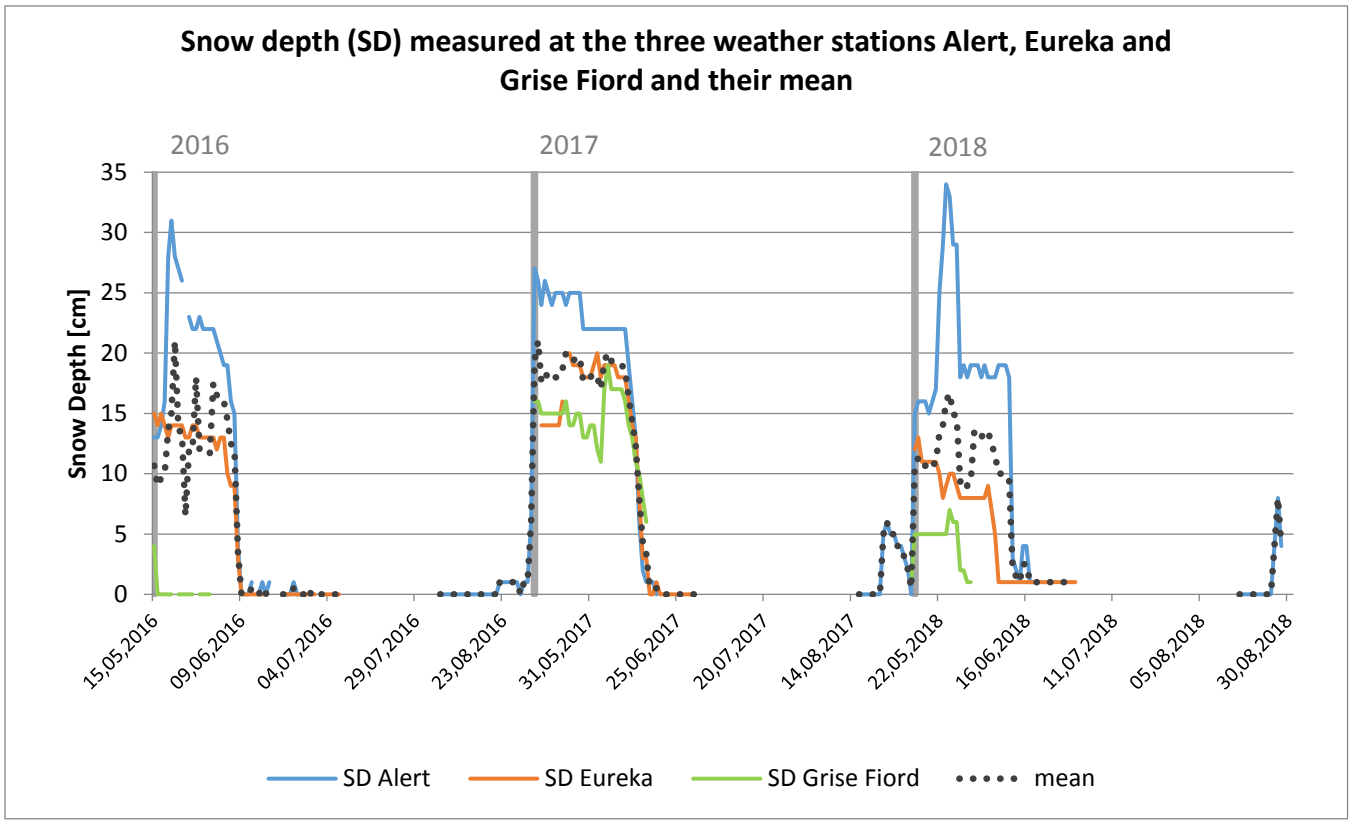


Fig. 19. Snow depth measurements at the three different weather stations and the mean (www.climate.weather.gc.ca).

### 2.6.2. Digital Elevation Model (DEM)

The digital elevation model used in this study was processed in an earlier master thesis by Vögtli M. (2018). Vögtli M. (2018) combined two different DEM's; one covers Greenland (GIMP – Greenland Ice Mapping Project), the other Canada (CDEM – Canadian Digital Elevation Model). The combined DEM was then resampled to a 400m spatial resolution (Fig. 20).

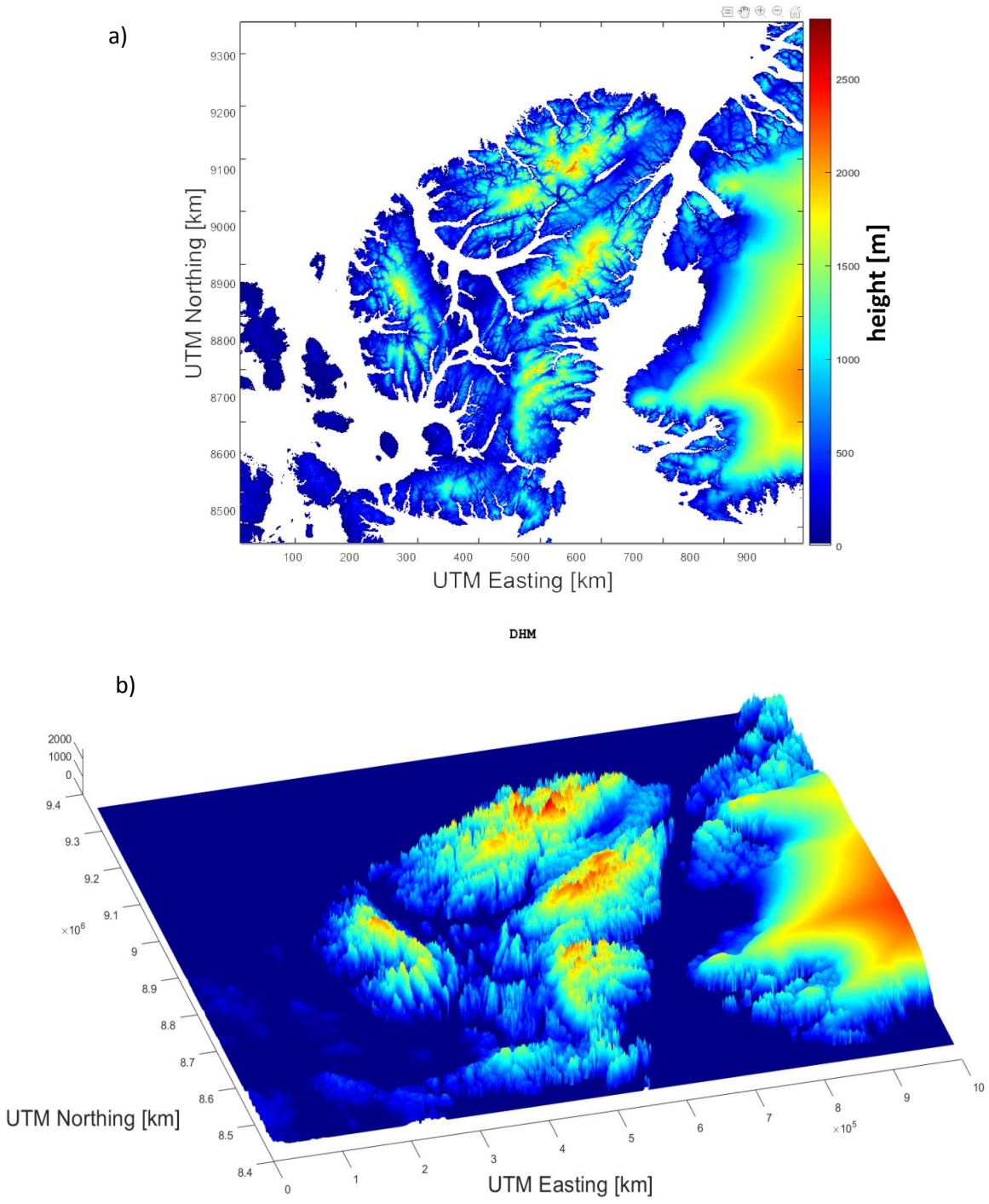


**Fig. 20. Combined Digital Elevation Model (DEM) of Ellesmere Island and adjacent Greenland. The DEM is presented from two different perspectives (a and b), to better illustrate the rough terrain.**

# 3. Methods

Passive microwave instruments can be used to map snow extent, estimate snow water equivalent and snow depth, and to derive snow/ ice melt onset and end (e.g. (Drobot and Anderson, 2001), (Belchansky et al., 2004), (Markus et al., 2009), (Bliss and Anderson, 2014)). Scatterometers and SAR instruments are used to map actively melting snow areas and to determine the melt onset and end (Nghiem et al., 2001), (Foster et al., 2011), (Howell et al., 2018). In a first step, wet snow was flagged using the three instrument types (SAR, Scatterometer and PM) and in a second step melt onset, melt end and the number of melt days was determined. Then the different results were compared with each other and other data, like ERA5 datasets and temperature reanalysis. Investigations were made over the years 2015 to 2018.

## 3.1. Pre-processing

After downloading the data needed (see chapter 2/ data for download links), it was necessary to transform each image into the same geometry. Otherwise an accurate analysis and comparison between the results is not possible. Therefore, each dataset was rewritten as a GEOTIFF, containing latitude and longitude information. Afterwards, using *gdalwarp*, these lat/lon information were transformed into the map projection UTM17 with a unified pixel spacing of 400m (Fig. 21), (GDAL/OGR contributors, 2018). Resampling ASCAT and AMSR2 images to a 400m spatial resolution was done using the nearest neighbor method.

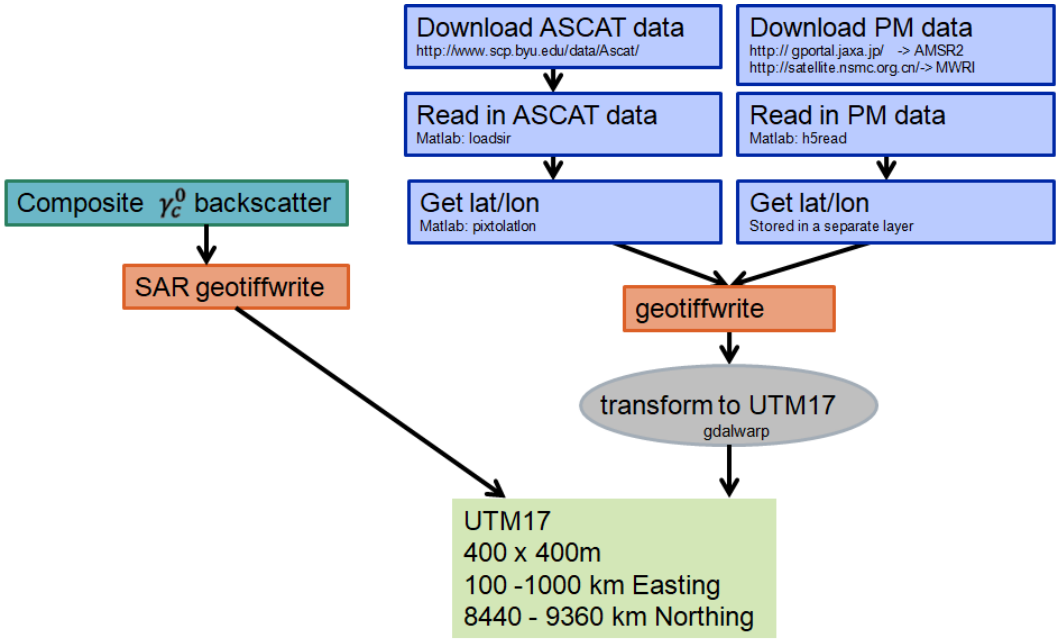


Fig. 21. Process chain for transforming all datasets into the same map geometry (UTM 17).

Optical sensors have difficulties mapping the surface beneath clouds. The problem can be mitigated with interpolation techniques (Parajka et al. 2010). But the uncertainty increases with a longer lasting cloud cover presence. Instruments working in the microwave spectrum are able to map beneath clouds and in darkness (Dietz et al., 2012). Mapping wet snow or ice areas was done using three different instruments: SAR, scatterometer and passive microwave. In the case of passive microwave, three different methods were applied and compared. For further analysis, the wet snow/ice area was calculated as the percentage of the whole land surface area within the spatial extent of observation.

According to Hall and Riggs (2007), some of the following methods perform better, if they are applied only on snow covered areas. Therefore, false positives from other surface types can be minimized. Here the ERA5 snow depth product was used as a snow extent mask, where all pixels with a snow depth > 0m were flagged as snow. This snow extent product was applied on the passive microwave data, as the spatial resolution of both products is similar and because the passive microwave single threshold based method lacks more in delineating wet snow from no-snow than the other methods (see also chapter 5.1.1.).

## 3.2. Wet snow or ice area (WSIA) mapping

### 3.2.1. WSIA mapping using PM

Passive microwave instruments like AMSR2 often have daily global coverage and are therefore well suited for time series analysis (Dietz et al., 2012). In addition to snow mapping also snow grain size, liquid water content and snow depth can be assessed with PM instruments (Rott and Nagler, 1995).

Disadvantages of passive microwave instruments are their low spatial resolution and the maximum measurable snow depth of about 1 m (Chang and Rango, 2000). The coarse spatial resolution, in the order of tens of km is unsuitable for small catchment analysis (Stettner at al., 2018).

At the melt onset, a rapid increase in brightness temperature can be observed and a corresponding decrease at the melt end (Fig. 22). This behavior makes it possible to demarcate melt onset and end. The melt onset corresponds to the position of the first significant upward edge along the time axis. The melt end corresponds to the last significant downward edge (Liu et al., 2006). To apply this method using Liu et al., 2006 proposed using the 19 GHz horizontally polarized band.

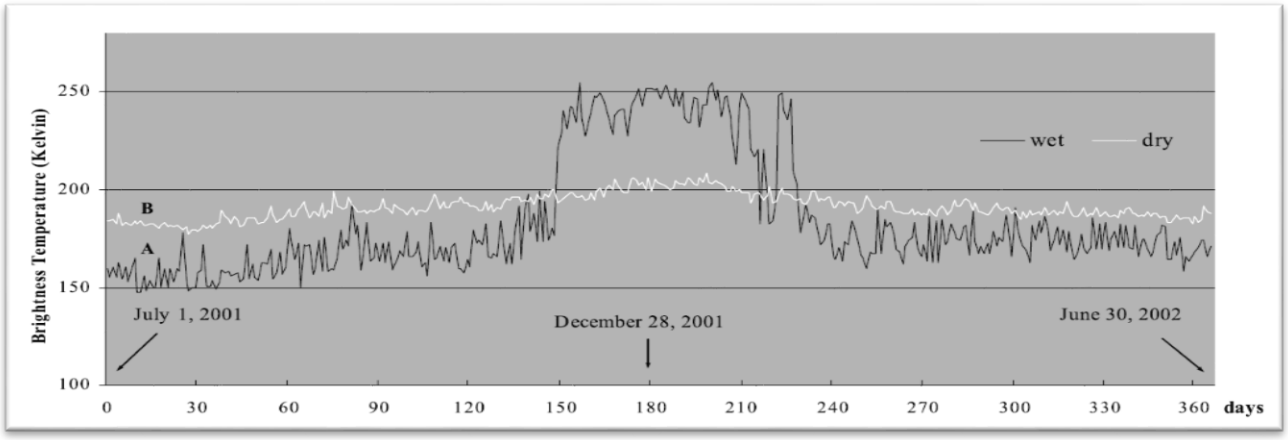


**Fig. 22. Time series of the brightness temperature measured at 19 GHz for wet and dry snow. The series was acquired over the Antarctic Peninsula. For wet snow, we can observe a clear increase in the brightness temperature, which is not observed for dry snow (Liu et al., 2006).**

#### *3.2.1.1. Diurnal Method*

Ramage and Isacks (2002) proposed a method using fixed thresholds. Foster et al., 2011 applied this method to AMSR-E data at 19 and 37 GHz. The melt onset is reached when both ascending and descending brightness temperatures exceed a threshold, while the difference between ascending and descending passes (diurnal amplitude variations, DAV) is also large. Using these two thresholds increases the probability that the melting persisted during the night and that the change in the brightness temperature is really related to liquid water and not to other factors (Foster et al., 2011). The thresholds are:

$$T_b36V > 242\ K\ AMSR2$$

$$DAV = abs(T_b ascending - T_b descending) \geq 10K$$

**DAV**: Diurnal amplitude variations

**Tb36V**: Brightness temperature at 36 GHz vertical polarization

And

$$T_b18H > 243\ K\ AMSR2$$

$$DAV = abs(T_b ascending - T_b descending) \geq 24K$$

**Tb18H**: Brightness temperature at 18 GHz horizontal polarization

#### *3.2.1.2. FY3 SCA Algorithm*

The FY3 SCA algorithm was developed by Li et al. (2007) for SSM/I data and then successfully tested by Liu et al., (2018) using FY-3/MWRI data. The algorithm uses several multiband thresholds to detect snow covered areas and divide them into detailed categories (Tab. 3).

**Tab. 3. Classification criteria for the FY3 snow cover area mapping algorithm.**

| | |
|---|---|
| Thick wet snow1 | Tb23V <= 260 AND (Tb19V - Tb37V) < 20 AND ((Tb23V - Tb89V) - (Tb19V - Tb37V)) <= -5 |
| Thick wet snow2 | Tb23V <= 260 AND (Tb19V - Tb37V) >= 20 AND ((Tb23V - Tb89V) - (Tb19V - Tb37V)) < 8 |
| Thin wet snow | Tb23V <= 260 AND (Tb19V - Tb37V) < 20 AND -5 < ((Tb23V - Tb89V) - (Tb19V - Tb37V)) < 8 AND ((Tb19V - Tb19H) <= 6 OR (Tb19V - Tb37V) >= 10) |
| Thick dry snow | Tb23V <= 260 AND (Tb19V - Tb37V) >=20 AND ((Tb23V - Tb89V) - (Tb19V - Tb37V)) >= 8 |
| Thin dry snow | Tb23V <= 260 AND (Tb19V - Tb37V) < 20 AND ((Tb23V - Tb89V) - (Tb19V - Tb37V)) >= 8 |

Note for example that Tb23V corresponds to the brightness temperature measured at the 23 GHz vertical polarized band. The wet snow area was generated by joining the thick wet snow1, thick wet snow2 and the thin wet snow together into a single wet snow product.

#### *3.2.1.3. Single band threshold*

As seen in chapter 2.2.1., the brightness temperature increases as soon as the snow changes from dry to wet. This signal can be best seen in the 19 GHz H-polarized band according to Liu et al., 2006. Hence, this band was used to measure the brightness temperature difference between a single scene and a cold dry reference scene. The reference scene consisted of a mean over the whole January and February at each pixel, ensuring the snow to be cold and dry. Different thresholds for the difference image were tested: a threshold of 30°K showed the highest correlation with the SAR/Scatterometer results:

$$T_b19H - T_b19H(ref) > +30°K = WS$$

### 3.2.2. Wet Snow or Ice Area (WSIA) mapping using SAR/ Scatterometer Instruments

Wet snow or ice decreases the backscatter compared to dry snow/ ice, the difference usually has a magnitude over -3dB (Koskinen et al., 1997). The backscatter coefficient decreases with an increasing liquid water content. The C-band penetration depth of dry snow is typically 20m (one-way), but for wet snow with 5% liquid water content less than 3cm. One can use a reference scene and then calculate the ratio to a snow scene by subtracting the local reference backscatter from the candidate scene; this method is called change detection. The reference scene can either be snow-free, or a scene with dry snow cover. Taking only one scene as a reference can lead to high uncertainties, as variations in soil moisture can also affect the backscattering significantly. A more reliable solution is to take an average over multiple dry snow or snow-free scenes, which also reduces speckle. Typically, the reference image is taken by averaging the scenes between autumn and midwinter, when most surfaces are either covered by dry snow or snow free (Nagler and Rott, 2000). In this study the

reference scene was created by calculating the mean backscatter value for each pixel over the first two months (January and February) of each year.

The reduction in backscatter relative to the reference scene is therefore an indication of snow melt. For discriminating wet from dry snow a **threshold of -2dB** was applied in the ratio backscatter image, which was found to be appropriate in single track investigations by Nagler et al., 2016. Change detection is a more stable solution than a simple threshold, because topographic effects are eliminated even without terrain flattening, due to the consistent illumination at each location. But some surface types, like agricultural fields or wetlands can have significant changes in the backscatter over time due to changes in surface roughness or wetness. These misclassifications can be removed by using land cover maps. Post-processing was done by exclude water surfaces with a watermask product derived from the MCD12C1 product (Fig. 23), (Nagler and Rott, 2000), (Nagler et al., 2016). For the grassland class in the MCD12C1 product another threshold of **-1dB** was found to be best suited in this study region. For more information on why another threshold had to be used for grasslands see chapter 5.5.4. In the case of SAR, different composite intervals were compared, from 1 day composites to 3 day composites, as well as HH and HV polarizations. For the SAR and scatterometer data the exact same method was applied, but the SAR images used were generally 2-days or 3-days composites, whereas the ASCAT images were acquired within a single day.

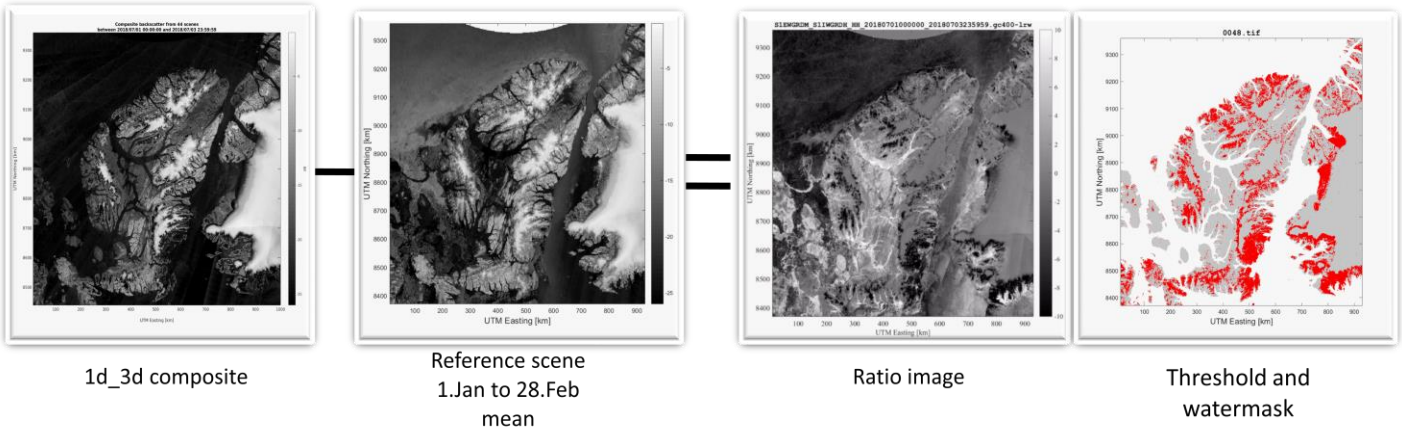


**Fig. 23. Scheme for SAR backscatter ratio generation and wet snow mapping. The red surfaces indicate wet snow or ice. Contains modified Copernicus Sentinel data (2018).**

To achieve a complete picture as possible also sea ice was included in a further step. To detect melting sea ice two other thresholds had to be applied. Howell et al. (2018) proposed a threshold of **-5dB** using ASCAT and a threshold of -8dB for SAR on multi-year-ice (MYI). For first year ice (FYI) a threshold of +5dB was suggested for both instrument types. Here, a threshold of **-5 dB** was used for MYI and one of **+5dB** for FYI for both instrument types. FYI was separated from MYI by applying a threshold of -14.5 dB on the winter reference mean image. Every sample with a larger value than -14.5 dB is considered as MYI (Kwok, 2004). Melt onset can be estimated simply using this threshold based change detection method, but melt end and the number of melt days are problematic. As soon as the sea ice is completely melted, the remaining water surface has still a very low backscatter due to the strong absorption of water at C-band. Therefore, such areas will still be flagged as melting sea ice. To overcome this problem, a sea ice extent mask was used, to exclude ice-free water surfaces. The ice extent mask was generated with the ECWMF sea ice concentration product, where only areas with an ice concentration higher than 20% were considered as sea ice.

## 3.3. Melt onset and end detection

Melt onset and end were calculated using the WSIA. The first day in the year when a pixel was flagged as wet snow or ice corresponds to the melt onset for this pixel. Melt end was then defined as the last day in the year the pixels were flagged as wet snow or ice. For this purpose, a data cube of all the WSIA binary images was created. Fig. 24 holds an example for the calculation of melt onset and end. For every location (pixel) the information of WSIA is stored in a vector. A value of 1 in the vector indicates wet snow or ice, a 0 corresponds to dry snow/ice or no snow/ice. The example shows the first 1 value at position 3. Therefore, after 3 days this pixel was mapped as wet snow/ice for the first time. The Melt onset was therefore day 3 at this pixel location.

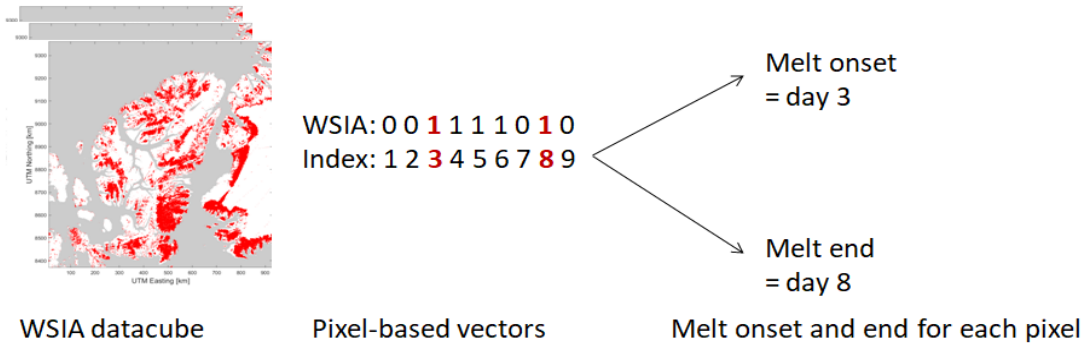


**Fig. 24. Flowchart for the detection of melt onset and end. Note that this is an illustrative example not representing actual onset and end values.**

Melt onset and end detection of sea ice with passive microwave instruments could not be addressed using the single threshold based method. Nevertheless, a product was obtained from the Passive Microwave (PMW) algorithm (see data). This dataset allowed us to investigate melt onset and end of sea ice, although the spatial resolution is only 25 km.

## 3.4. Number of melt days

The number of melt days at each pixel was not calculated by the difference of melt onset and melt end. This could lead to failures because snow or ice can be completely melted leading to a non-melt period during summer. Refreezing periods are possible and would be excluded too. Therefore, the number of melt days corresponds to the sum of days at which each pixel was flagged as wet snow or ice. Looking again at the example in fig. 24, the number of melt days is the sum of all 1 values. In this example, a 1 is represented 5 times, leading to a number of melt days of 5.

## 3.5. Sensor intercomparison

The created products (melt onset, end and melt days) were further analyzed. First to test their credibility and second to compare the products derived from the different sensors. For this purpose, the digital elevation model was used. Each product was divided into different height classes, ranging from 0 m a.s.l. to >1700 m a.s.l. with 100 m steps. The reason for combining all points higher than 1700 m a.s.l. was the small number of pixels in such higher terrain. In fig. 25 a typical pixel count is illustrated.

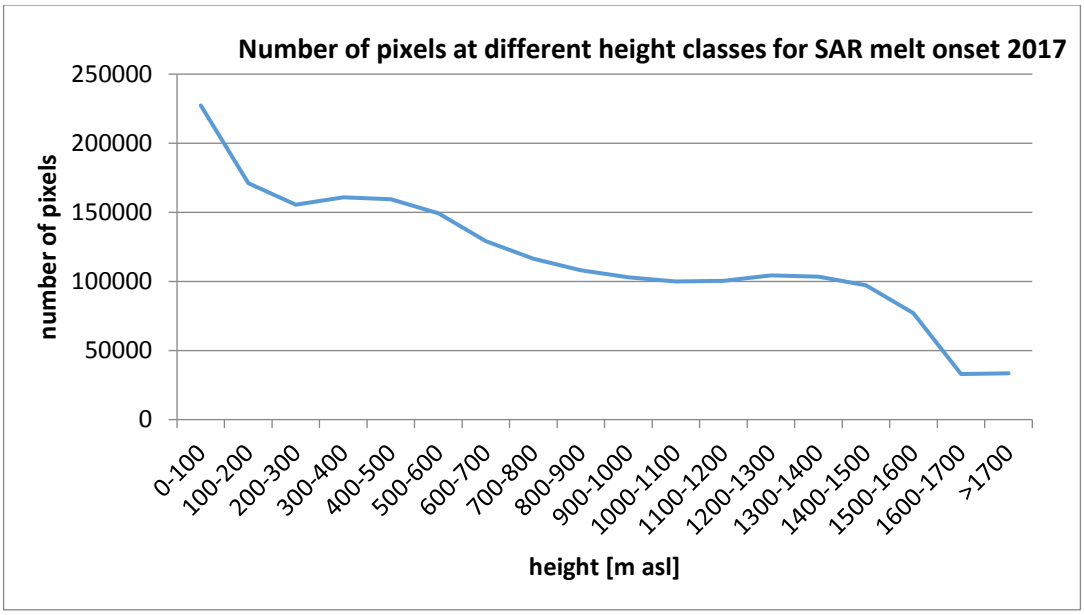


Fig. 25. Number of non-zero pixels for different height classes. In this case the 2017 SAR melt onset is illustrated.

After the combination of the height classes, the mean, median and the interquartile ranges were calculated for each height class and each product (onset, end and number of melt days).

Not only different heights can affect the timing and evolution of snow or ice melt, but also the aspect. South-facing slopes typically show warmer conditions, due to a steeper incidence angle to the sun (McCutchan and Fox, 1986). Therefore, similar to the different height classes, also different aspect classes were generated. Aspect values were derived from the digital elevation model (Fig. 26).

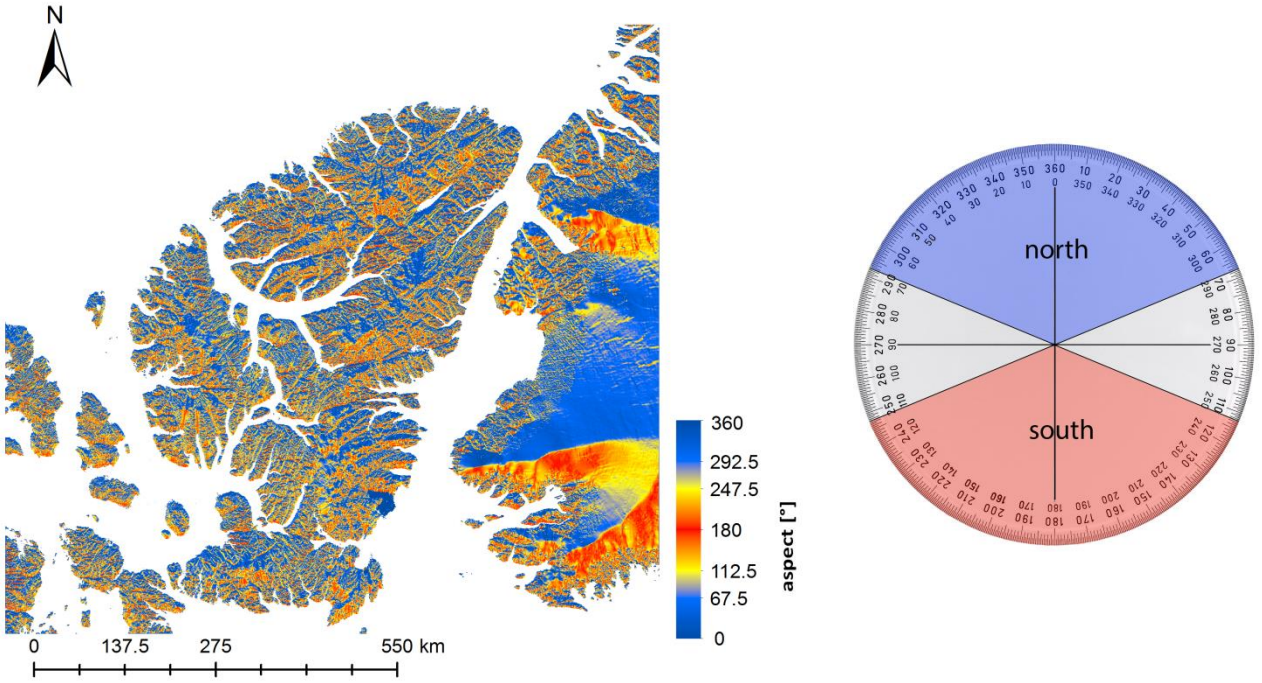


Fig. 26. Left: Aspect product derived from a digital elevation model of Ellesmere Island. Right: definition of north and south facing slopes

Two different aspect classes were created; north and south facing slopes. North facing slopes were defined as aspect values ranging from 0° to 67.5° + 292.5° to 360° and south facing as 112.5° to 247.5°.

Melt onset was also calculated using the MODIS land surface temperature data, where melt onset was defined as the first day with temperatures above 0°C. Now melt onsets could be compared spatially with a temperature estimates grid.

In summary, a flow chart of the methods applied can be seen in fig. 27.

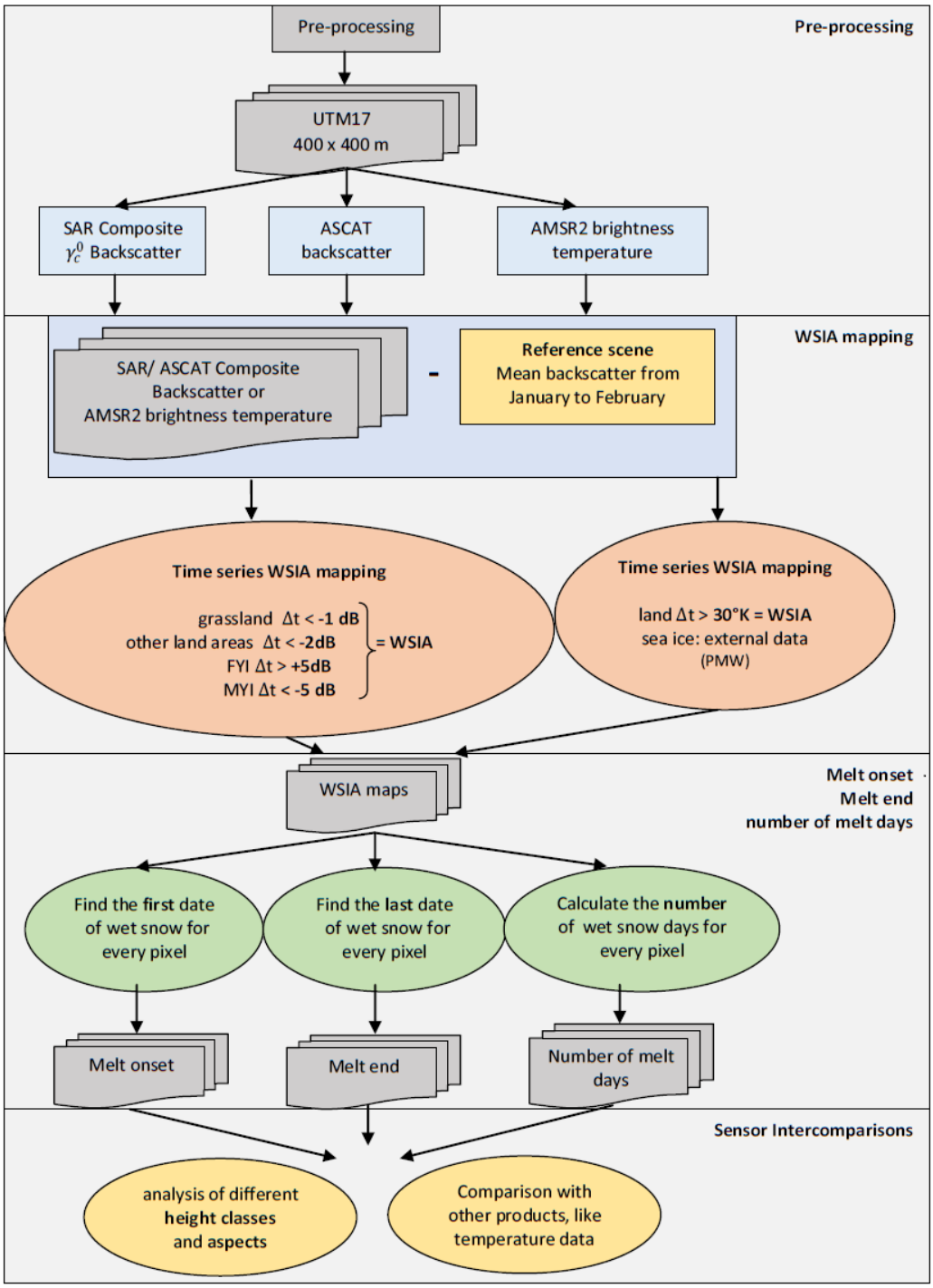


Fig. 27. Flow chart of the methods applied in this study.

# 4. Results

Results from the years 2015 to 2018 are presented here. First, a comparison between three different WSIA mapping algorithms for passive microwave data is shown. Second, the WSIA products mapped with the three different sensor types (SAR, scatterometer and passive microwave) are presented and compared. In addition to the sensor intercomparison, the results are compared with auxiliary information, such as temperature. The third part illustrates and compares the melt onset, end and the number of melt days, which were processed using the WSIA time series products. Finally, sea ice melt is also included, to give a complete image of the study area. In the complete image, also a new threshold for the grassland area on Ellesmere Island was used, to achieve a better result.

WSIA derived from SAR, ASCAT and PM showed a strong correlation with each other, temperature and snow depth data. SAR WSIA on land showed the strongest correlation with temperature data (r = 0.74). Melt onset, melt end and number of melt days products derived by the three instrument types also showed a strong correlation to each other. Earlier melt onsets were found for lower elevations. Earlier melt ends were found for high elevations and also for lowlands. The latest melt ends were found on the elevation of the lower part of the ice caps, where also the highest numbers of melt days were measured. Sea ice melt onset, end and number of melt days also showed strong correlation to each other, except in the northwestern ocean part of the study area, where SAR estimated melt onset much earlier. However, when estimating melt onset without a reference scene, the resemblance in sea ice melt onset was much higher (see chapter 5.7).

## 4.1. Wet snow or ice area (WSIA) mapping

WSIA was the basis for estimating melt onsets and ends. In the four years of observation, every summer day where melt processes could occur was investigated. In the case of the land areas the time period was from the May 15 to September 1. When sea ice was included, the time range was expanded from April 1 to September 30.

### 4.1.1. Comparison of the different Passive Microwave (PM) WSIA mapping methods

The three methods applied to map wet snow areas with the passive microwave instrument AMSR2 exhibited significant differences (Fig. 28).

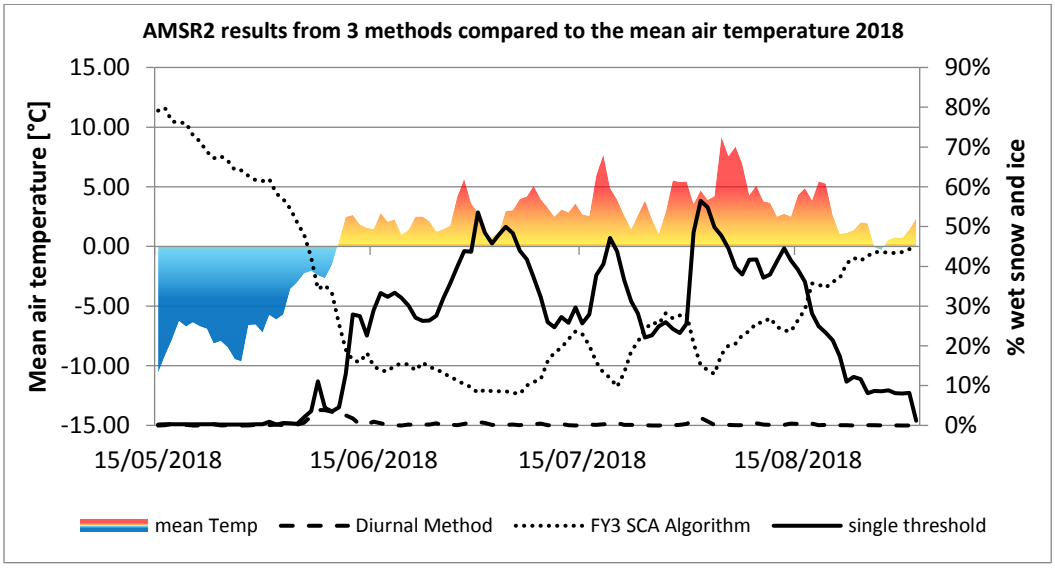


**Fig. 28. Comparison of the wet snow and ice area derived from the three passive microwave methods (diurnal, FY3 SCA, single band threshold) and the mean air temperature measured at the three weather stations Alert, Eureka and Grise Fiord.**

The diurnal method by Ramage and Isacks (2002), clearly underestimated the wet snow area on Ellesmere Island compared to the mean air temperature and the other two methods. The FY3 SCA algorithm showed a negative correlation to the mean air temperature measured at the three weather stations Alert, Eureka and Grise Fiord. With increasing air temperatures, a decrease in the WSIA was observed, where the largest wet snow area was at the coldest mean air temperature (~ -10°C). Only the single band threshold method showed a good correlation with the mean air temperature. Therefore, all further investigations and the comparison with the other instruments (SAR and Scatterometer) were performed using results from the single band threshold method.

### 4.1.2. Comparison of WSIA derived from SAR, Scatterometer and PM instruments

The comparison of the wet snow/ ice area (WSIA) derived by the three different instruments showed strong correlation with each other and the mean air temperature (Fig. 29). Especially ASCAT and SAR (Sentinel-1 and RADARSAT-2) showed very similar results, with the biggest differences between them caused by temporal or spatial gaps in the SAR data. The correlation coefficient between SAR and scatterometer WSIA was 0.94. Results from the passive microwave single band threshold, often produced significant higher peaks for the WSIA. The correlation coefficient of the mean air temperature and SAR was 0.74, 0.71 for the temperature and scatterometer and 0.72 for the temperature and PM.

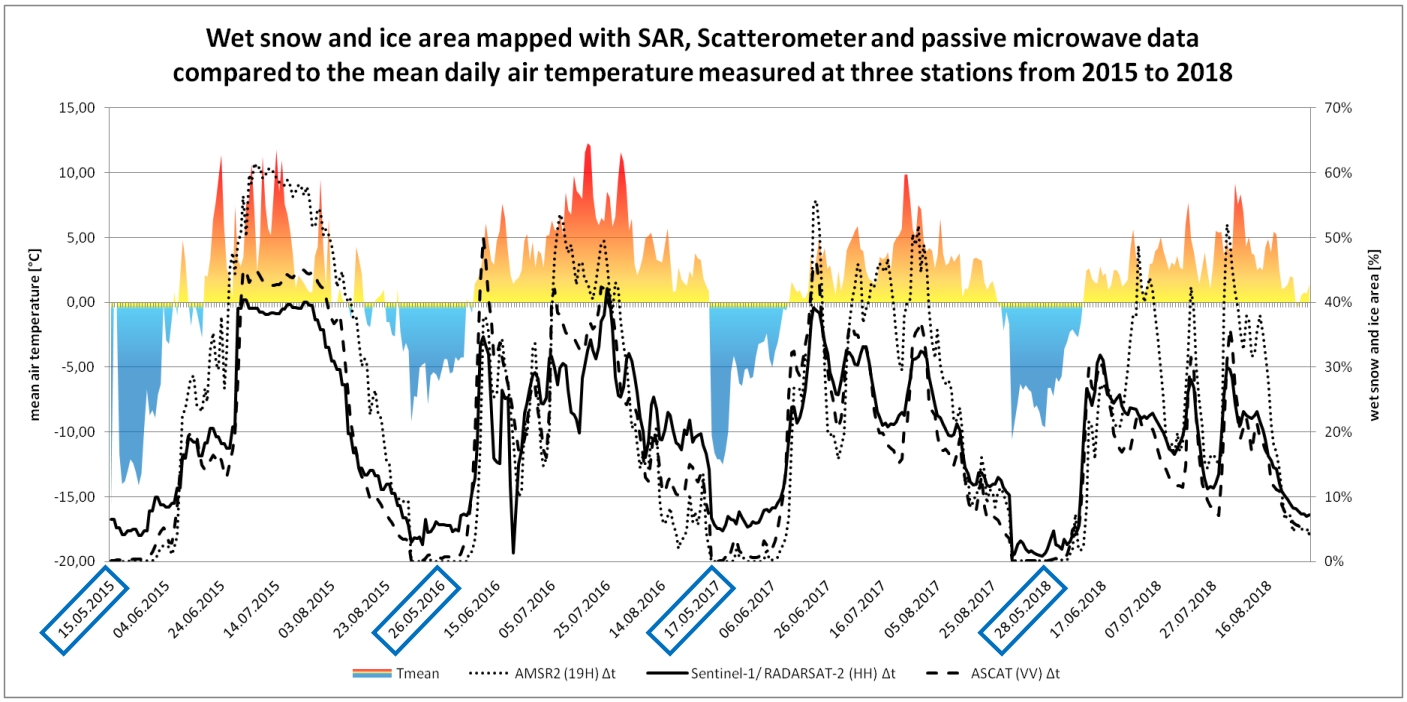


Fig. 29. WSIA derived from the three different instruments and compared to the mean air temperature.

The snow depth measurements from the three weather stations showed a strong negative correlation with the WSIA results (Fig. 30). A strong decrease in snow depth was observed at the first strong increase in WSIA. It should be noted that the three weather stations are located in lowlands and therefore the snow is melted quite early in the year, whereas in higher elevations more and longer lasting snow is abundant.

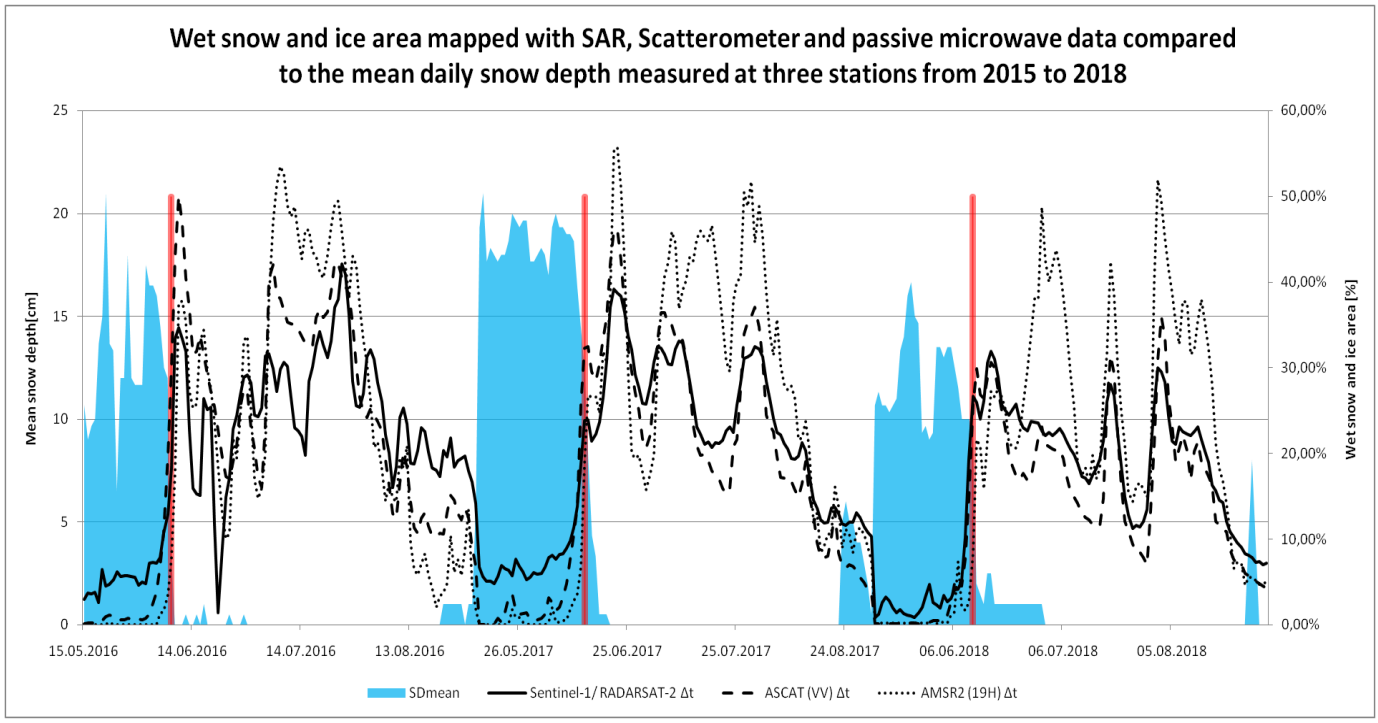


**Fig. 30. WSIA derived from the three different instruments and compared to the snow depth. The red bars indicate the timing of strong increase in WSIA and strong decrease in snow depth respectively.**

Analyzing the WSIA mapped by the different instruments again showed a strong correlation (Fig 31). Especially the scatterometer and the SAR products had a high similarity. In addition to the overall similarities, some differences could be seen. The scatterometer and the PM products had a much coarser resolution compared to SAR. The PM instrument mapped significant larger WSIA on some days, such as 20.07 and 19.08.2017.

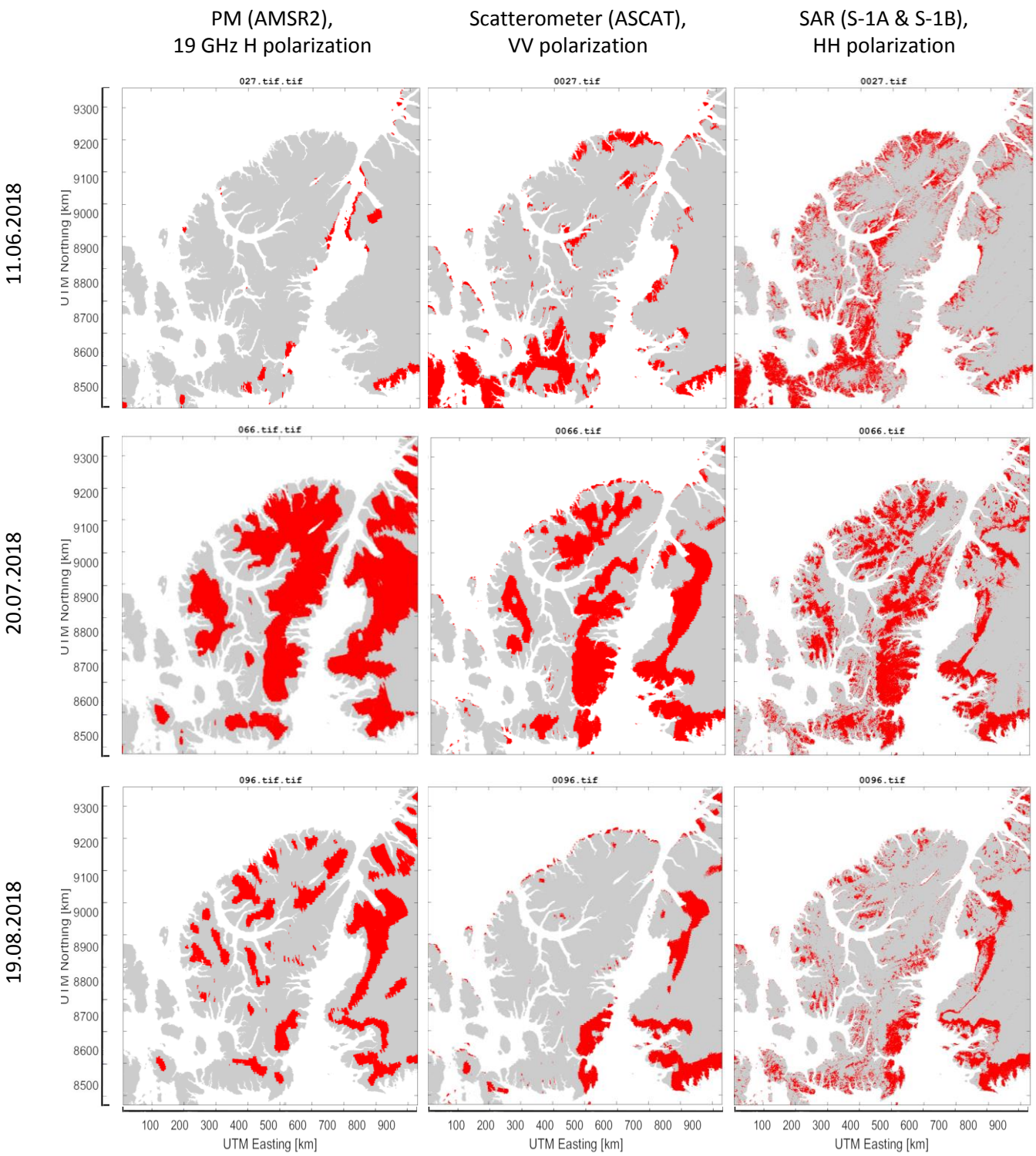


**Fig. 31. WSIA (shown in red) derived from the three different instruments (SAR, scatterometer and PM) shown for selected dates in 2018. Contains modified Copernicus Sentinel data (2015-2018).**

The WSIA showed less correlation with the ERA5 snowmelt product (Fig. 32). For instance, in the midsummer of 2015 the applied methods indicated a large WSIA, while the ERA5 snowmelt product flagged almost no WSIA. The correlation coefficient of SAR WSIA and ERA5 snowmelt product was just 0.46, whereas the correlation coefficient of SAR WSIA and the mean air temperature was 0.74.

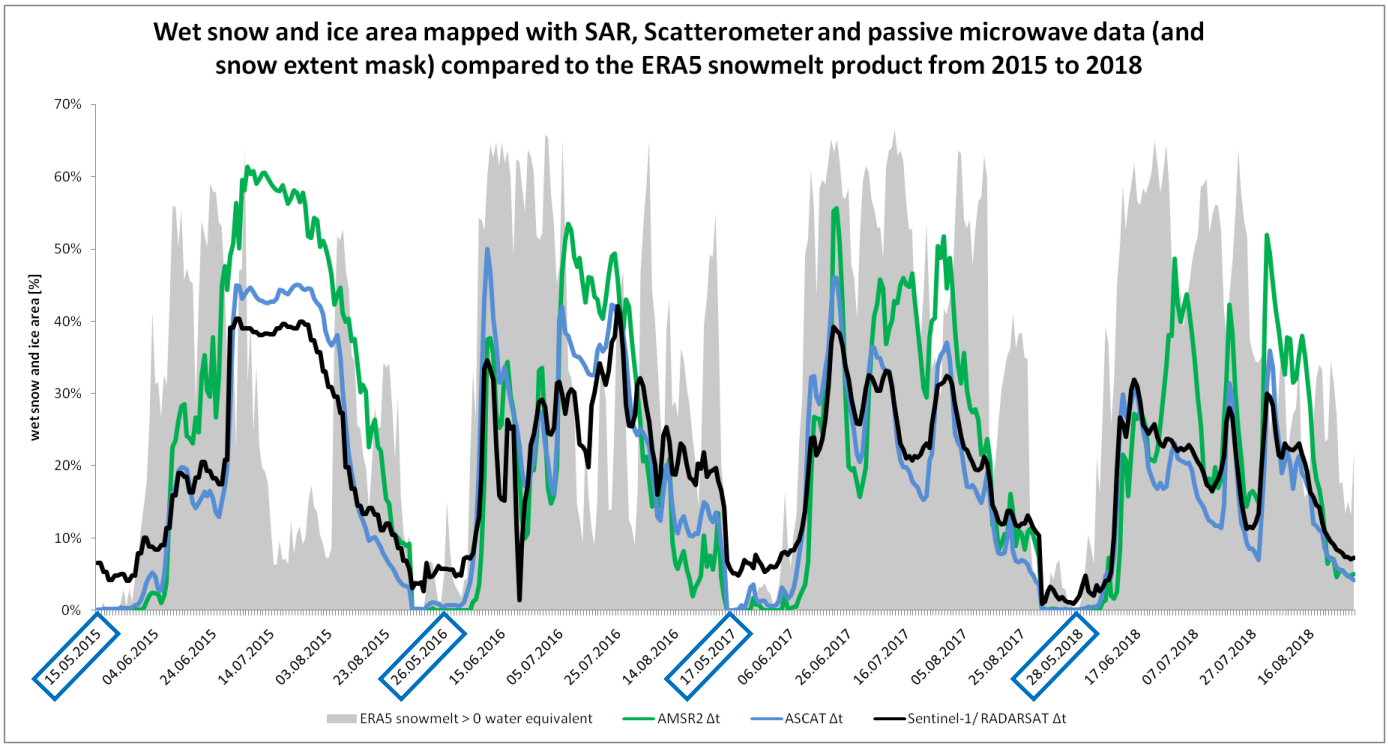


Fig. 32. WSIA derived from the three different instruments, compared to the ERA5 snowmelt product derived WSIA.

The ERA5 snowmelt product of 20.07.2015 showed significant differences to the WSIA flagged with the methods applied in this study (Fig. 33). SAR and scatterometer indicated WSIA primarily over the ice caps, where the ERA5 product did not. The spatial resolution of 0.25° was extremely low in the ERA5 product.

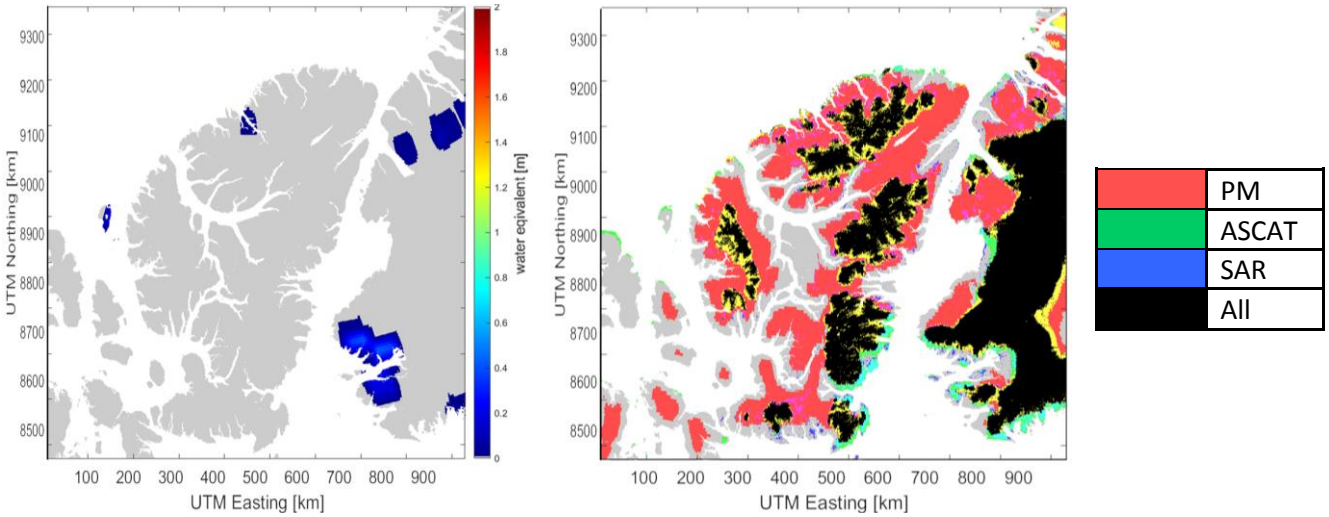


Fig. 33. Left: ERA5 snowmelt product derived WSIA map for the 20.07.2015. The blue area indicates wet snow. Right: WSIA derived by the three sensors SAR, scatterometer and passive microwave. The black area indicates wet snow detected by all three sensors.

## 4.2. Melt onset

This chapter presents the spatial distribution of melt onset estimates. The products were compared using their median values representing different height classes and aspects.

Fig. 34 presents maps of melt onset derived from the three sensor types: SAR, scatterometer and passive microwave. SAR melt onsets were prepared using 3-day composites, except for 2015, where 4-day composites had to be used, due to lower data availability. It should be noted that in these products the same threshold of -2dB was used over all the land areas, also for grassland. The grey area in these maps corresponds to land areas where no onset was found. No onset was found when over the period of investigation not a single day of WSIA could be determined.

Especially in the year 2016, but also in 2015, a larger area of no-onset-found was seen in the SAR derived maps in comparison to the other products. The reason for these additionally missing onset areas was probably due to missing SAR data. In 2015, SAR images were only available from Sentinel-1A and RADARSAT-2, Sentinel-1B images became available in late 2016 (www.earth.esa.int). Therefore, fewer SAR images were available in 2015 and 2016. Nevertheless, we observed a high degree of similarity, especially between SAR and scatterometer based maps. Passive microwave derived onset maps had nearly no missing onset areas; a melt onset could be found for the majority of the land areas. Exceptions were coastal areas, where PM often found no onset.

The years 2015 and especially 2016 showed much earlier melt onset dates in all products, indicating higher, or earlier warm temperatures in these years. On the ice caps this could also be seen, where almost everywhere an onset was found in 2015, but in 2018, no melting was ever evident at the highest parts of the island and Greenland.

Generally, an earlier melt onset was observed for lower areas, for example on the coast or the lowlands near Eureka or Lake Hazen (Fig. 34.). Later melt onsets, indicated by blue or green colors were typically found in mountain regions, for example at the ice cap near the Barbeau Peak.

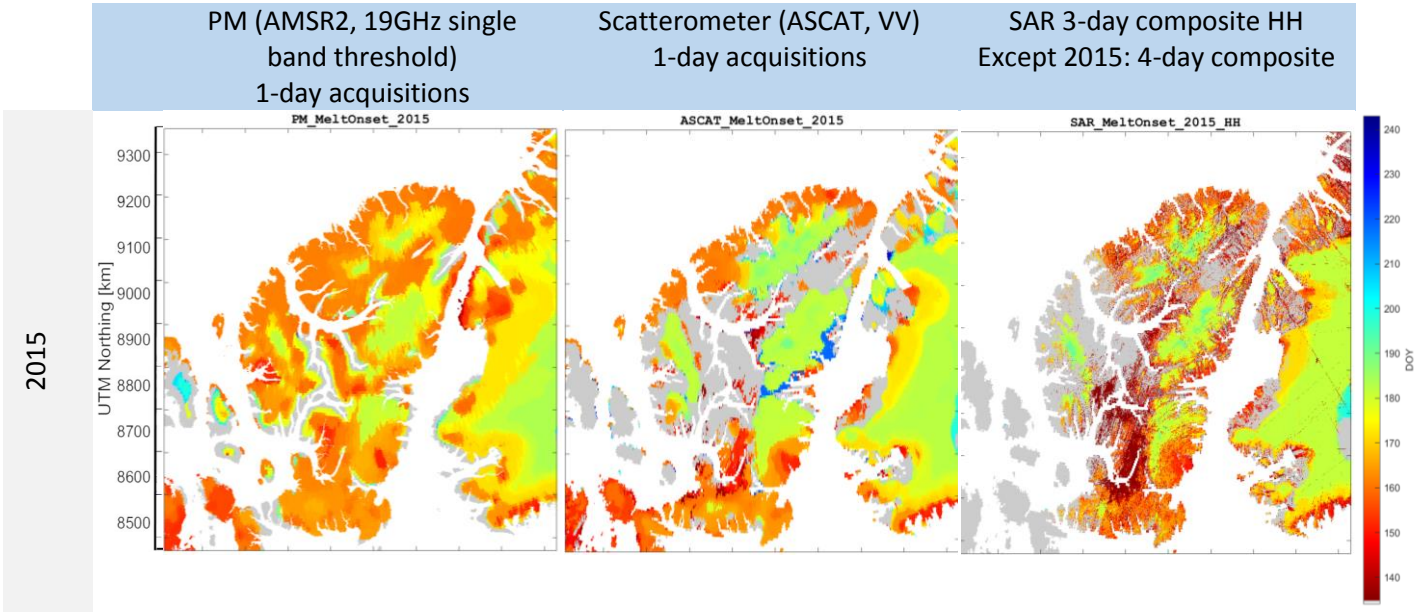

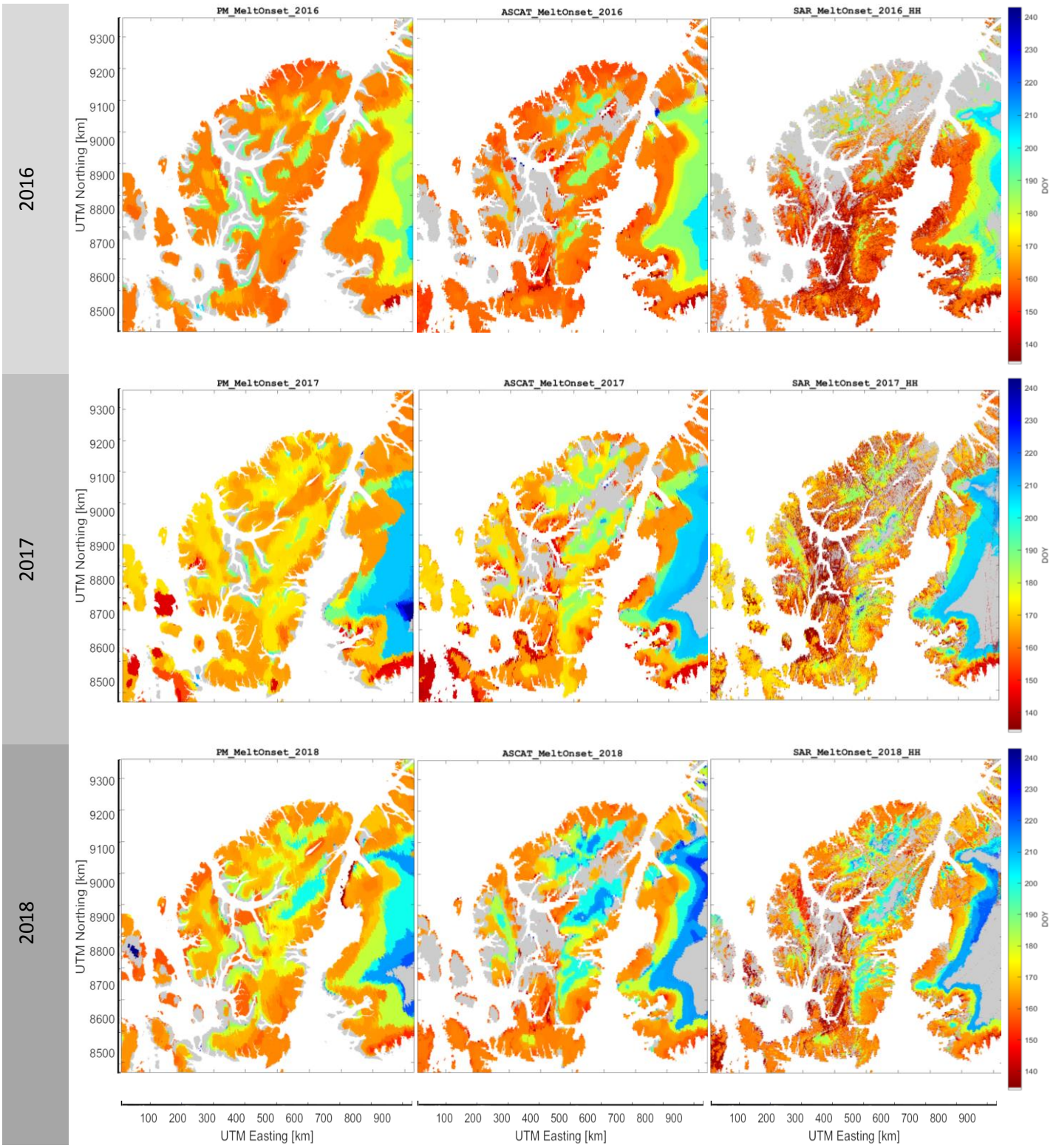


**Fig. 34. Melt onset maps generated with C-band SAR, scatterometer and passive microwave 19GHz data, showing the melt onset day of the year (DOY). Only land areas were mapped. Contains modified Copernicus Sentinel data (2015-2018).**

An earlier melt onset in lower land areas is also seen in Fig. 35. Fig. 35 shows the median melt onset with different height classes. A clear increase of later melt onsets was observed at higher elevations. The only exceptions were the two highest classes in the years 2016 and 2017 and only for the SAR melt onset products.

The percentage land samples with no onset found pixel is illustrated for the SAR products, indicating their uncertainty. The higher the percentage of no onset found pixels to the total number of pixels, the more uncertain is the melt onset median value. The highest uncertainty was present in the highest areas, but only in the years 2017 and 2018, caused by lower temperatures leading to no melt in high areas.

Scatterometer and SAR products had very similar onset values, especially after 2015. Passive microwave often showed earlier melt onsets, particularly at higher elevations.

Overall, a strong progression of melt onset dates was observed over the height classes containing ice caps (>1000m a.s.l.), as seen in fig. 35 especially for the years 2016, 2017 and 2018. The interquartile range gives information about the data distribution. The interquartile range corresponds to the middle 50% of the data, which is the difference of the upper and the lower quartile. Therefore, a small interquartile range means a small spread in the data (Upton and Cook, 1996).

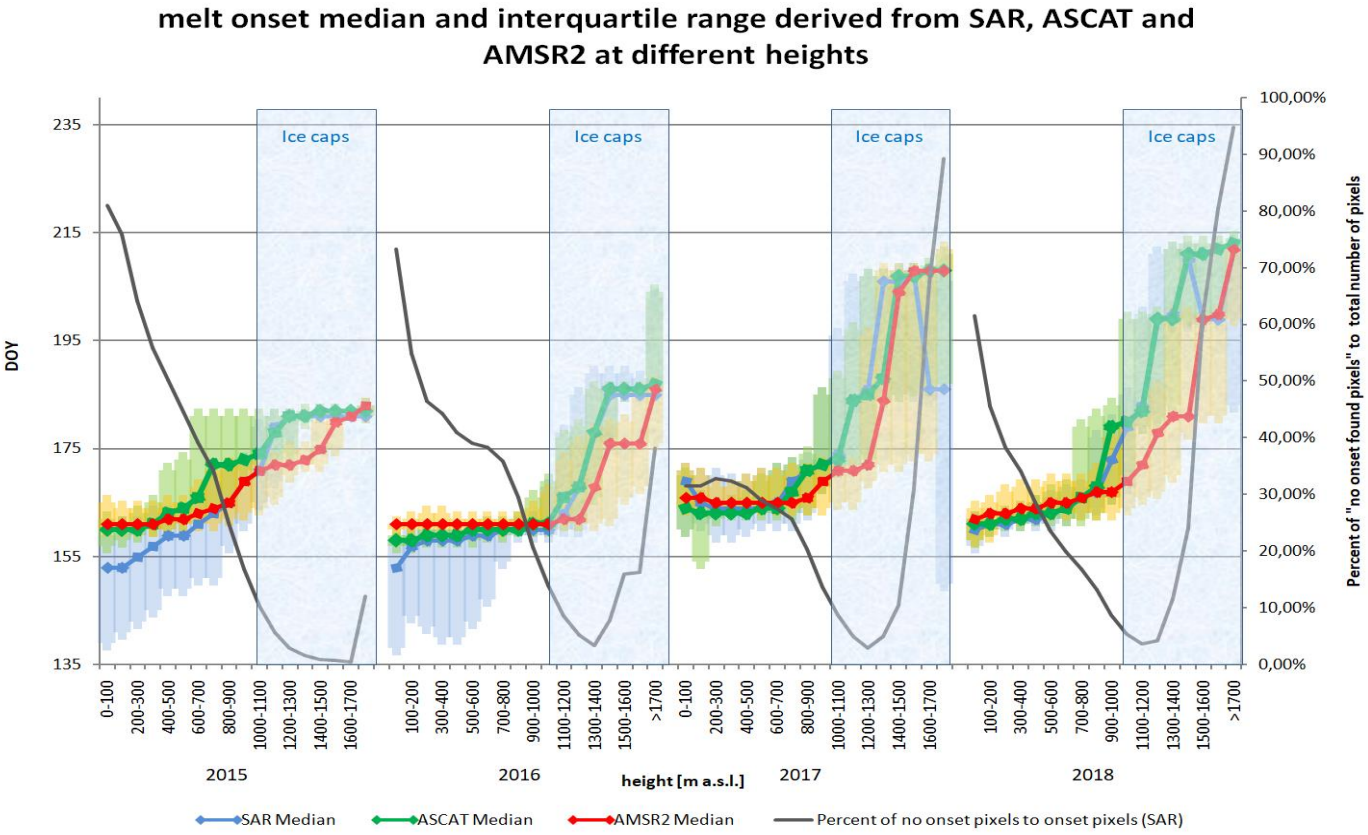


**Fig. 35. The melt onset median and the interquartile range are shown for different height classes and years. Three different sensors are compared (SAR, scatterometer and passive microwave). The blue boxes indicate the approximate height of the ice caps on Ellesmere Island. The black line shows the percentage of "no onset found samples" to the total number of land samples.**

Mean melt onset was earlier on south facing than on north facing slopes for all sensors. The difference between the north facing and the south facing slope melt onset was typically 3-4 days (Fig. 36). The difference in melt onset of the ice caps was 7-8 days for SAR and PM, for scatterometer it was 3.5 days. In contrast to the land mean, the SAR mean melt onsets in the ice caps' elevation were later compared to PM.

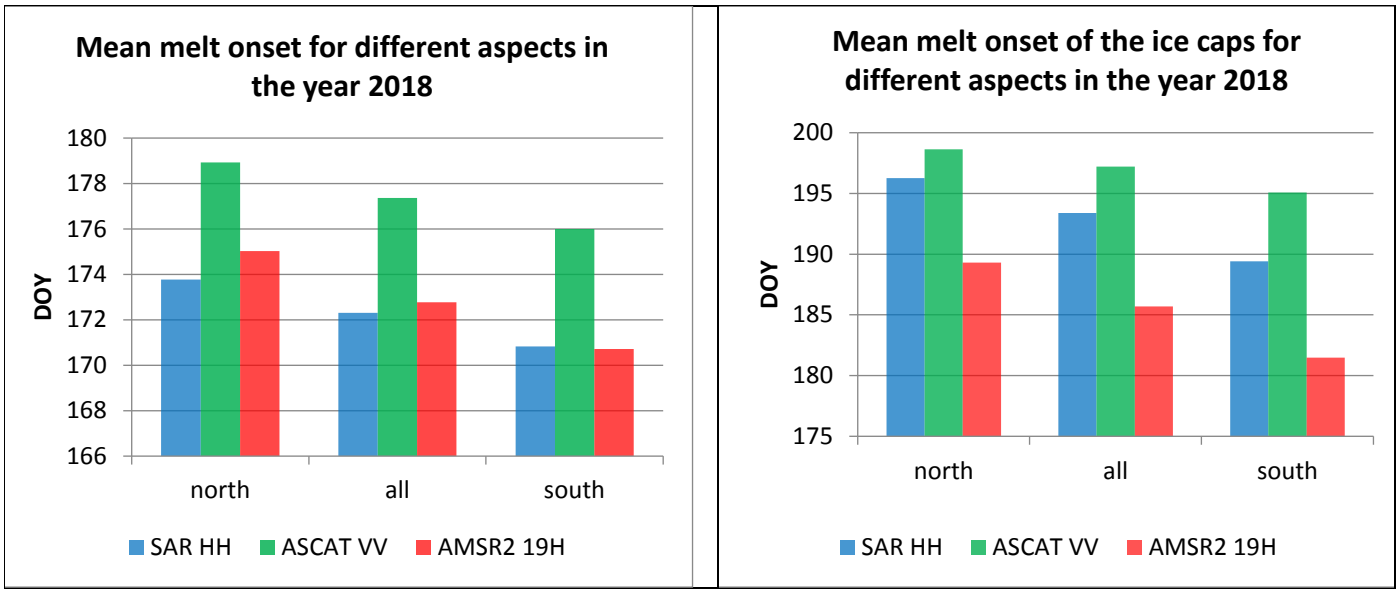


Fig. 36. Left: Mean melt onset for different aspects (north facing vs. south facing slopes). Furthermore, the three different sensor types (SAR, scatterometer and passive microwave) are compared. Right: Mean melt onset in the ice caps' elevation for different aspects.

In fig. 36, a later overall melt onset for ASCAT than for the other two instruments is shown. The reason for such a later mean melt onset with ASCAT cannot be fully explained by later melt onset values at the same pixels. In fig. 35 we saw generally high similarities between SAR and ASCAT melt onset values at different heights. Another factor causing the melt onset difference could be a higher availability of onset-found-pixels in higher terrain for ASCAT. As we have seen, higher terrain caused a later melt onset. Therefore, more pixels with a later melt onset were available for the ASCAT product, resulting in a shift towards later melt onset. In fig. 37 the larger number of available pixels in higher terrain for ASCAT can be seen for the year 2017.

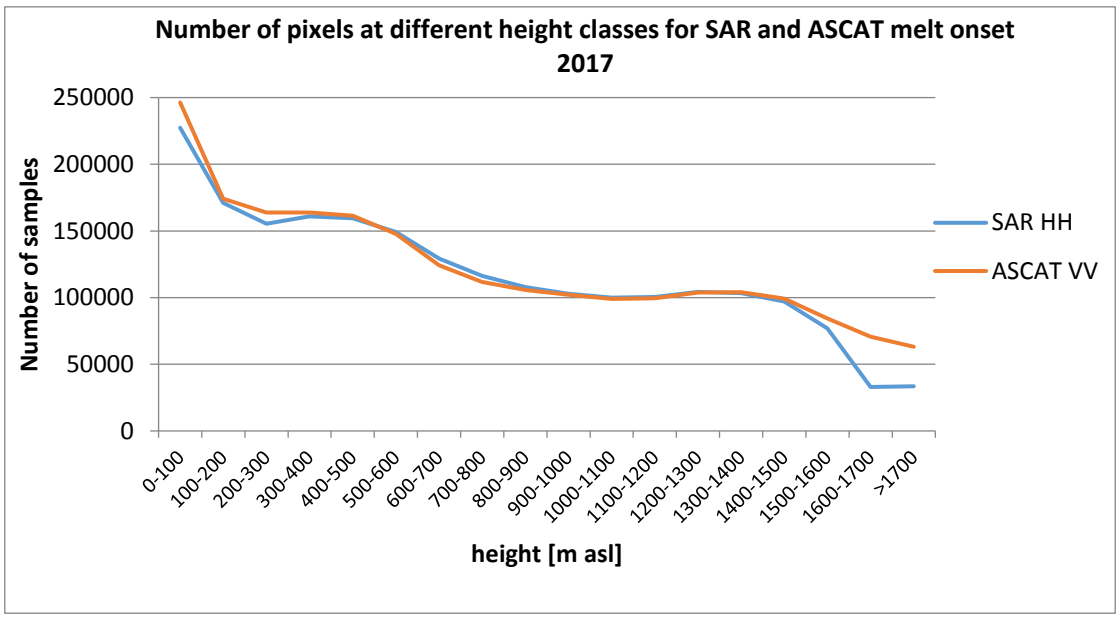


Fig. 37. Number of melt onset found samples in different height classes in the case of the 2017 melt onset products derived from SAR and ASCAT.

## 4.3. Melt end

Similar to the melt onset maps, the melt end products are presented in fig. 38. If no melt onset could be determined, then no melt end could be defined either. Therefore, the same areas appear grey.

Some areas showed an early melt end in areas of late melt onset. That behavior was expected, since that could be an indication of low air temperatures, for example in higher terrain. The earliest melt end values on the other hand, were found at the lowest elevations, for example in 2015 near the northern coastal area. Hence, some areas, especially low-elevation areas, showed an early melt onset, but also an early melt end. This pattern is probably caused by completely melted snow areas. As soon as the snow layer is melted completely, no further melt processes are seen, unless there is fresh snowfall within the melt period.

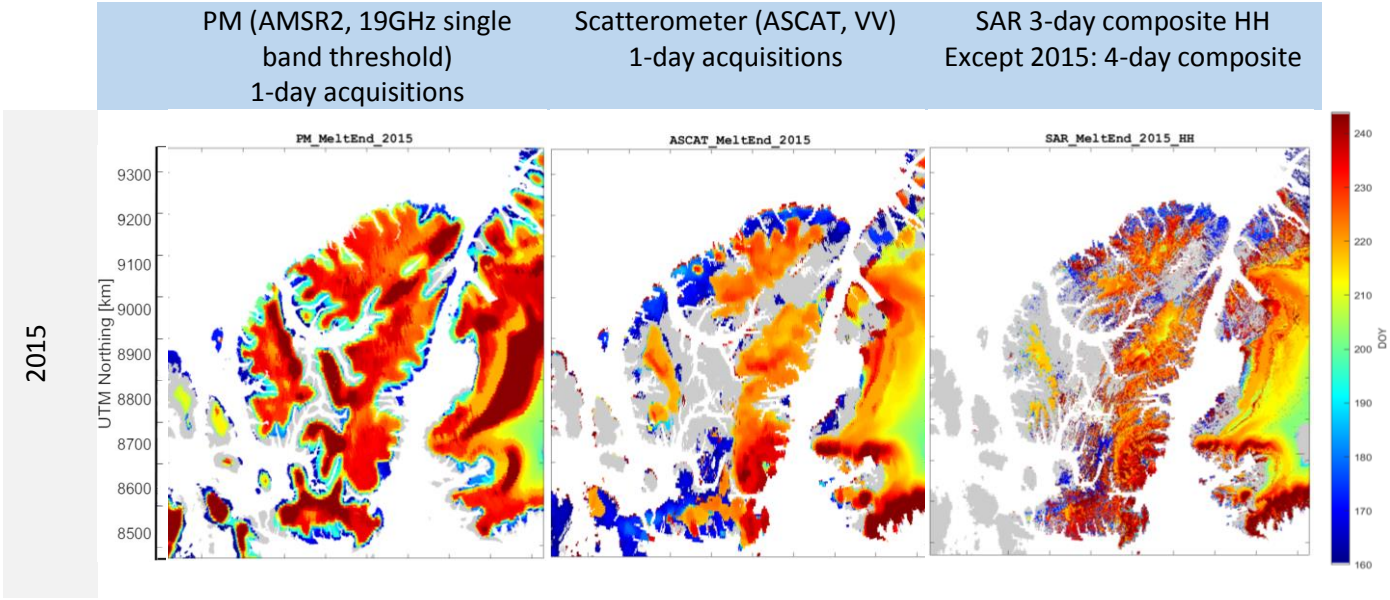

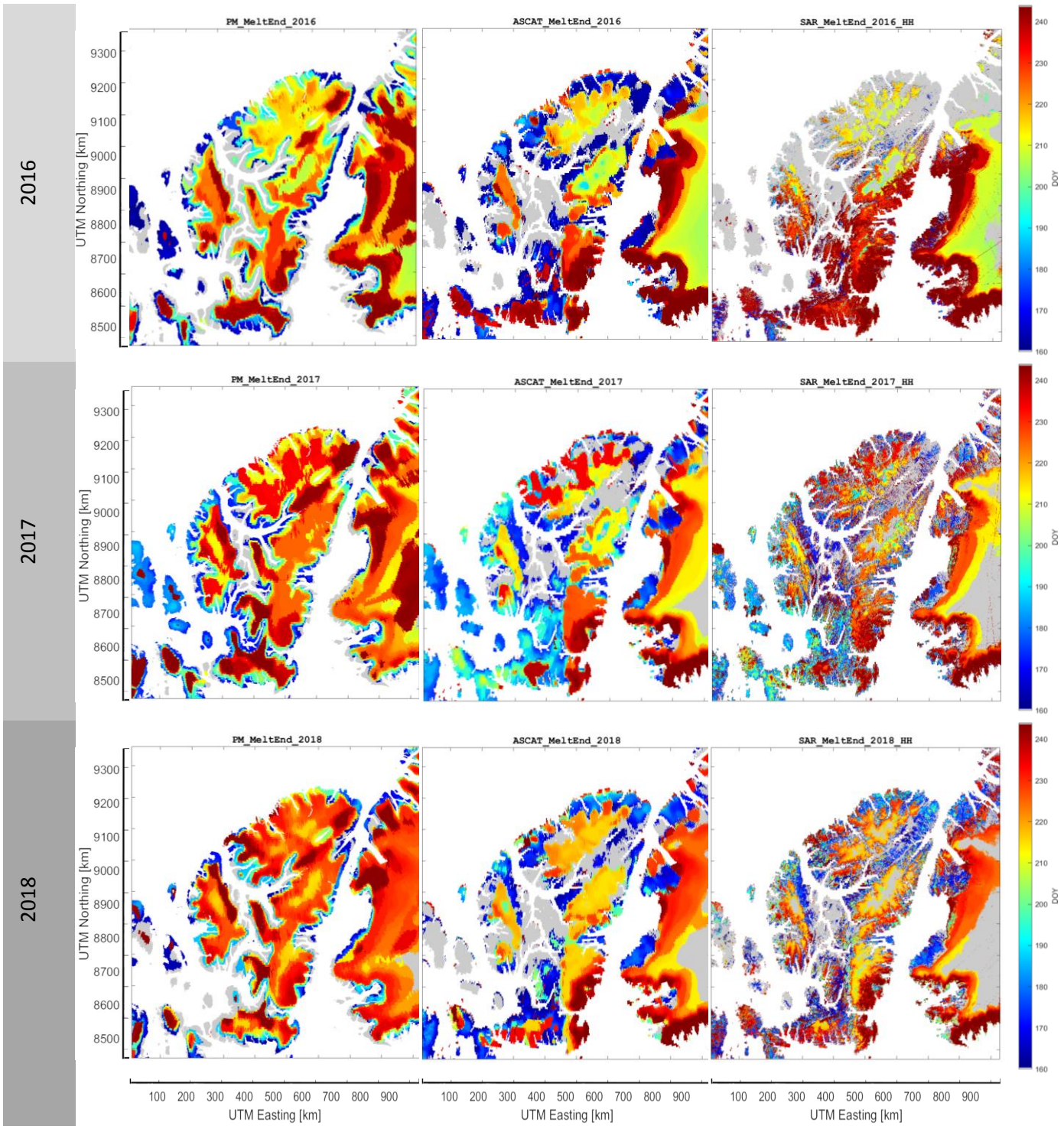


**Fig. 38. Melt end maps generated with SAR, scatterometer and passive microwave data, showing the melt onset day of the year (DOY). Only land areas were mapped. Contains modified Copernicus Sentinel data (2015-2018).**

In fig. 39, the melt end came earlier towards higher topography. Then, at the height of the ice caps, the melt end dates were again earlier. Exceptions were at height classes with a high percentage of no end found pixels. Overall, it was harder to recognize clear patterns in the melt end, than in the melt onset. For example, in 2016, SAR showed much later melt ends than the other two sensor types. Nevertheless, an n-shape pattern could be recognized, with the latest melt end values ranging between approximately 600 and 1200 m a.s.l., whenever the percentage of no-onset-found pixels was low enough to indicate reliable retrievals.

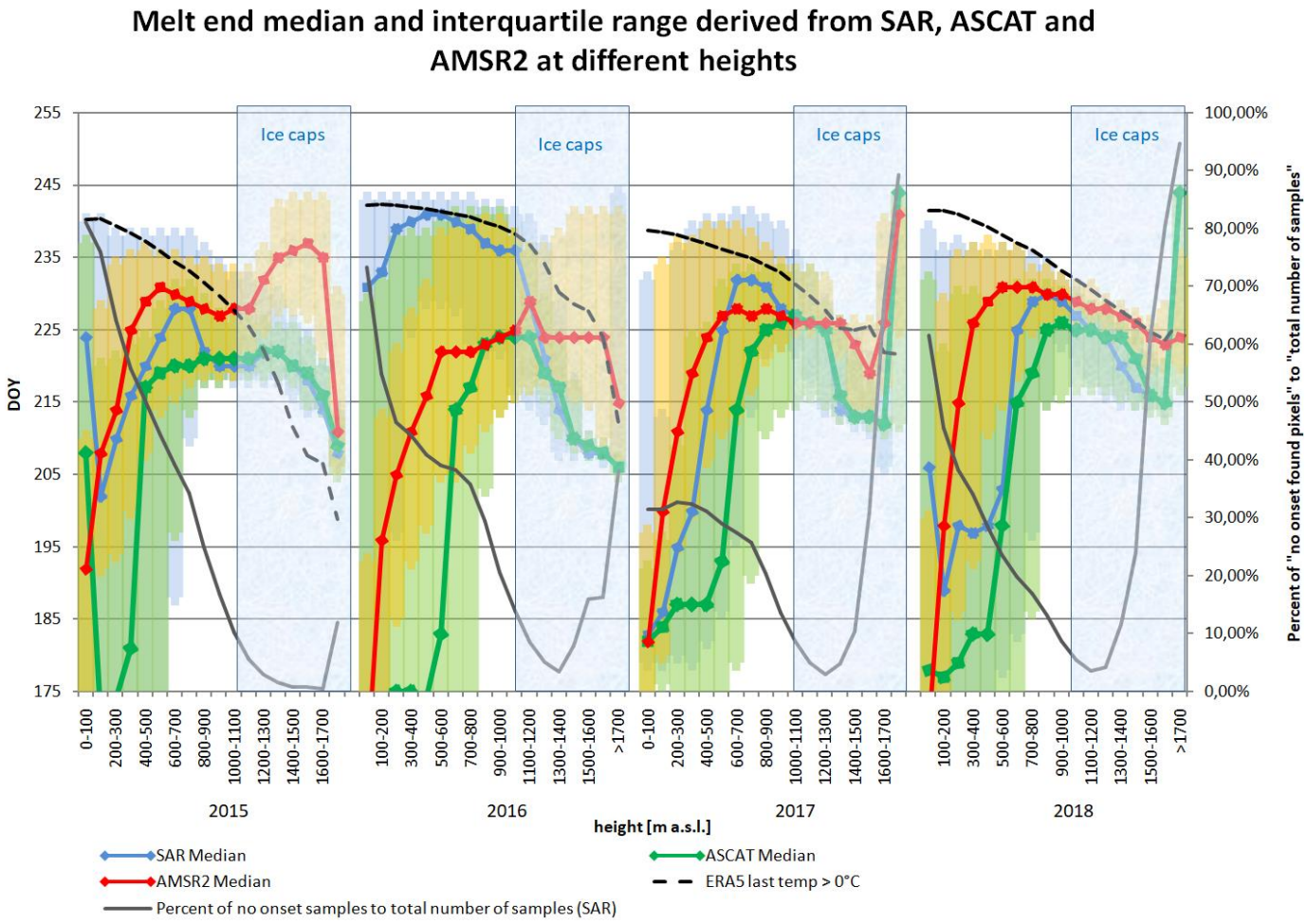


**Fig. 39. Melt end median and the interquartile range for different height classes and years. Three different sensor types are compared (SAR, scatterometer and passive microwave). The blue boxes indicate the approximate height of the ice caps on Ellesmere Island. The black solid line shows the percentage of "no onset found samples" to the total number of land samples. The black dashed line shows the last day with a temperature above 0°C in the ERA5 temperature data.**

Another significant finding was that intersensor differences were usually smallest at heights with a low percentage of no-onset pixels found. The interquartile range had its minimum in the same height class. Therefore, a higher number of valuable pixels improved the resemblance of the three sensors. An exception was the year 2015, where SAR and ASCAT showed a very high similarity in the low interquartile range, but AMSR2 did not.

## 4.4. Number of melt days

Melt days were not calculated as the difference between the melt onset and end, but by adding up the number of WSIA days. Therefore, the highest number of melt days was always observed at the low elevation of the ice caps, as well as on the coast of Greenland (Fig. 40). Simply calculating the difference between onset and end, would in some parts of the lowlands give much higher numbers, as these areas sometimes showed early melt onset and late melt ends.

Again, SAR and ASCAT showed higher resemblances to each other than to the passive microwave products. The passive microwave product generally showed a higher overall number of melt days. However, some areas showed more melt days in the SAR or ASCAT products, for example the southern coast of Greenland.

| | PM (AMSR2, 19GHz single band threshold) 1-day acquisitions | Scatterometer (ASCAT, VV) 1-day acquisitions | SAR 3-day composite HH Except 2015: 4-day composite |
|---|---|---|---|
| 2015 | 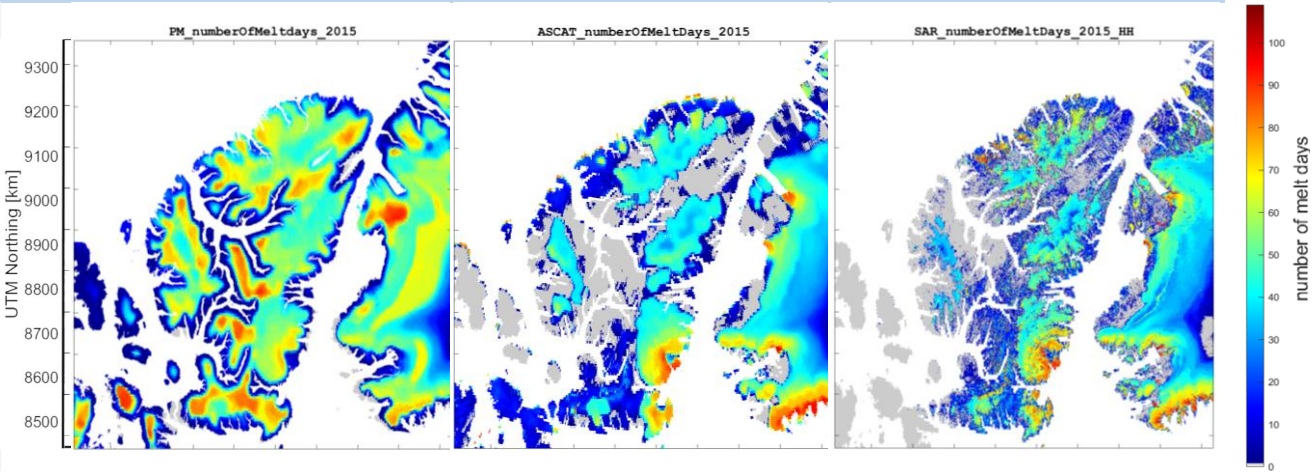 | | |

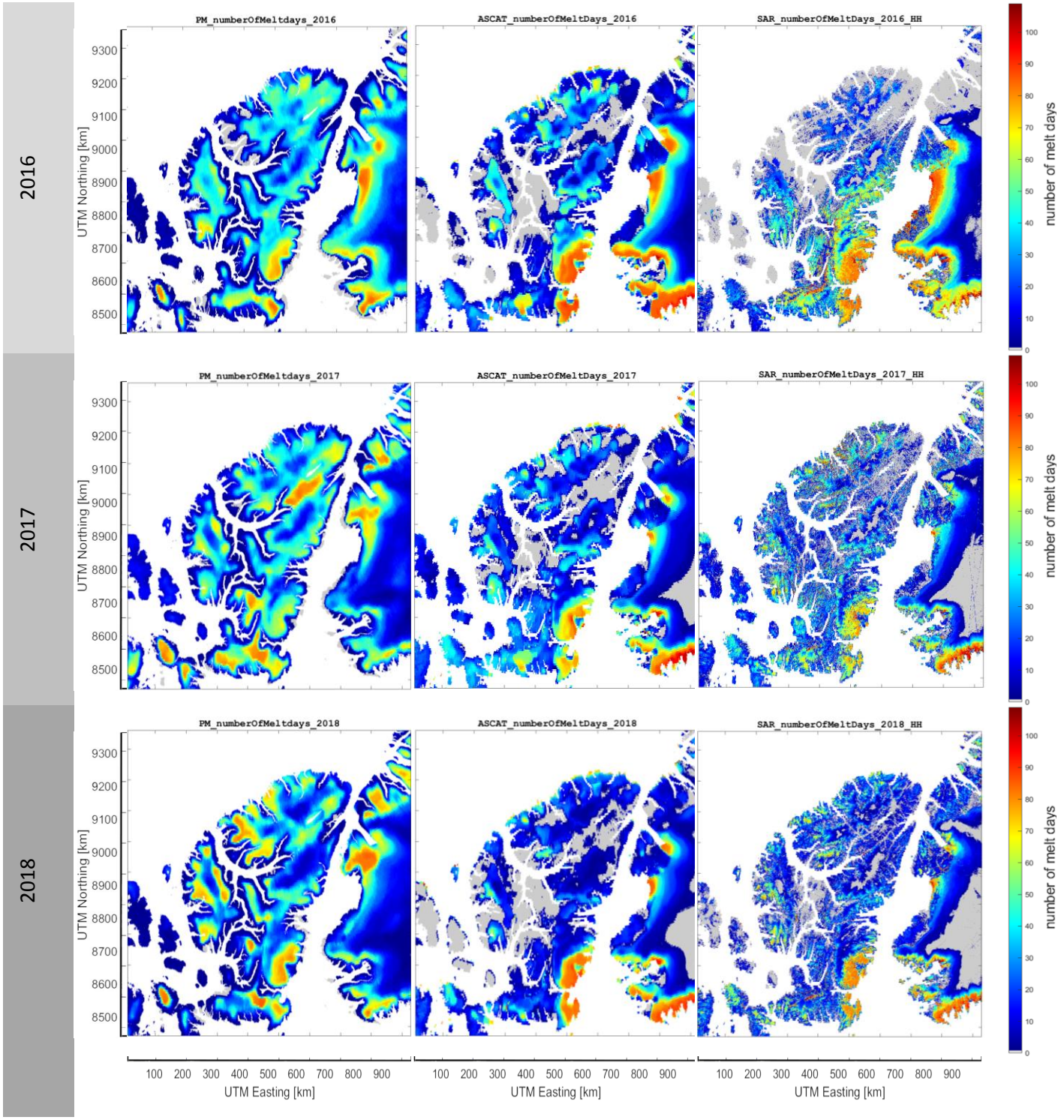


**Fig. 40. Total melt days maps generated with SAR, scatterometer and passive microwave data, showing the melt onset day of the year (DOY). Only land areas were mapped. Contains modified Copernicus Sentinel data (2015-2018).**

The median number of melt days in different height classes supported the visual findings of the melt day maps. ASCAT typically showed the lowest number of melt days while AMSR2 showed the highest number, except in 2016, when SAR surpassed AMSR2. The highest number of melt days was somewhere near the lowest part of the ice caps (ca. 1000m a.s.l.), (Fig. 41). Moreover, in colder years (2017, 2018), the maximum number of melt days was shifted towards lower terrain.

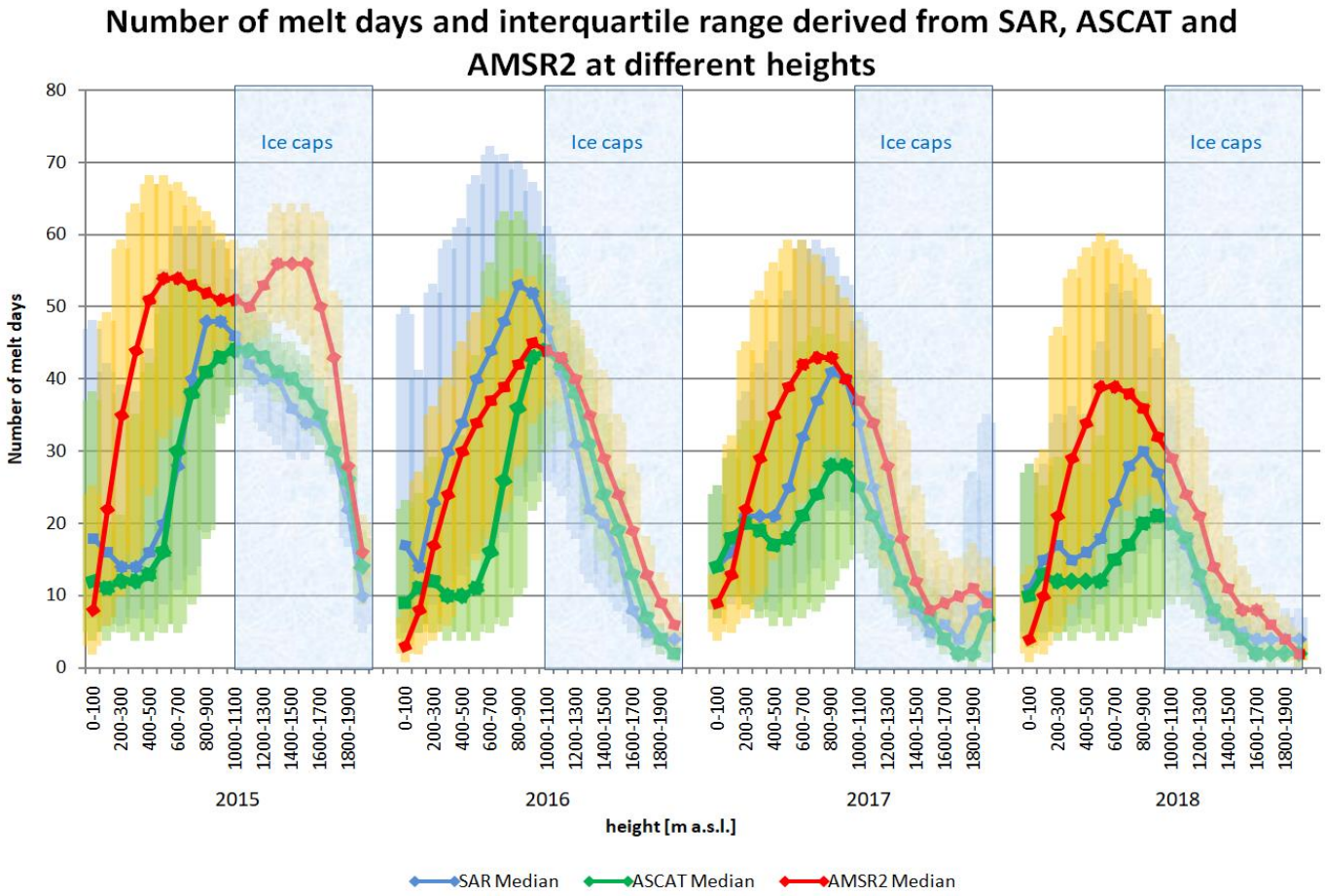


**Fig. 41. Median number of melt days and the interquartile range are shown for different height classes and years. Three different sensors are compared (SAR, scatterometer and passive microwave). The blue boxes indicate the approximate height of the ice caps on Ellesmere Island.**

Single glaciers on adjacent Greenland are shown in fig. 42. A higher number of melt days is seen in the glaciers. These glaciers are located in valleys, and therefore a warmer regime than their surroundings. They also hold a vast amount of ice, that does not melt completely throughout the summer.

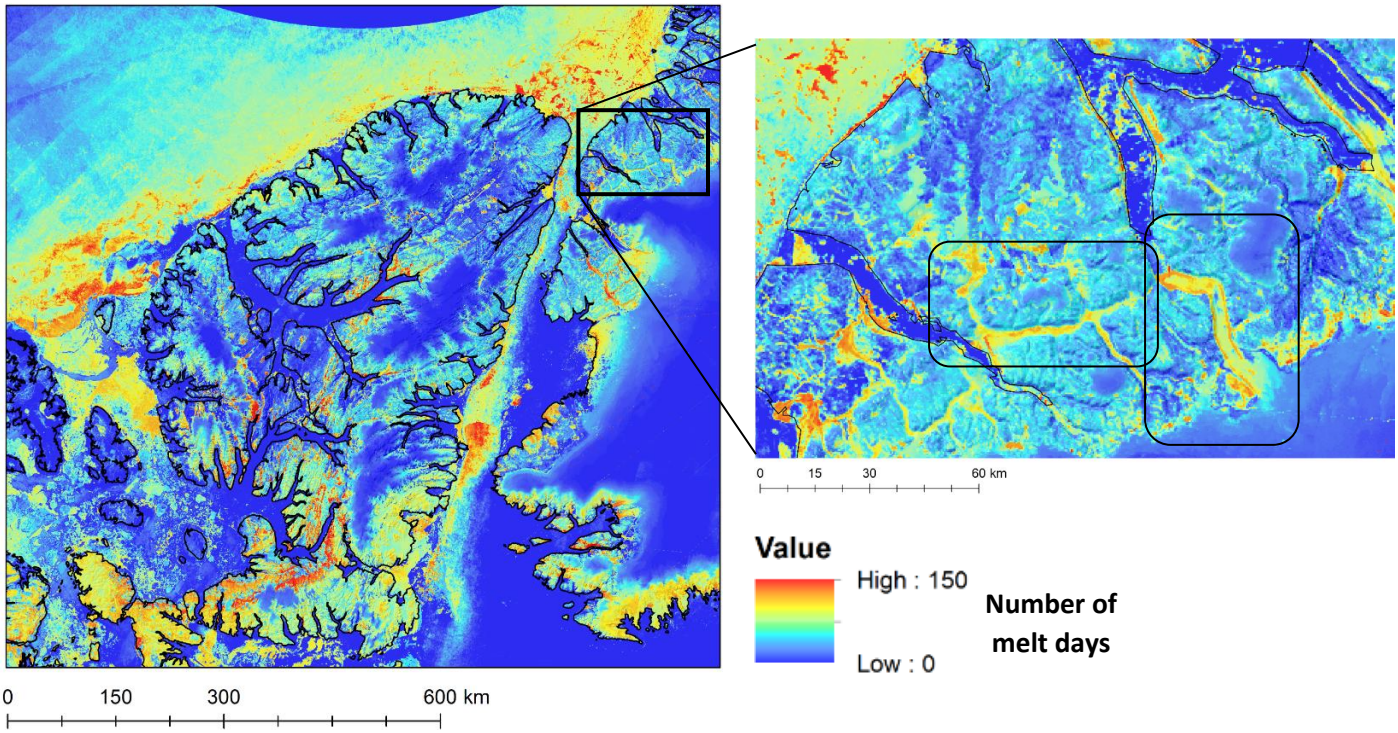


Fig. 42. Left: Number of melt days derived using SAR HV polarization in the year 2018 for Ellesmere Island. Right: Subset of the map on the left, showing a part of the northern coast of Greenland. Contains modified Copernicus Sentinel data (2018). RADARSAT-2 Data and Products ©MacDonald, Dettwiler Associates Ltd. (2018) – All Rights Reserved. RADARSAT is an official trademark of the Canadian Space Agency.

The mean number of melt days varied across different aspects. North facing slopes had a smaller number of melt days than south facing slopes. The difference was roughly 4 days for all sensors on the whole land area. The difference at the elevation of the ice caps was about 6 days, except for ASCAT, where it was only 3.5 days (Fig 43).

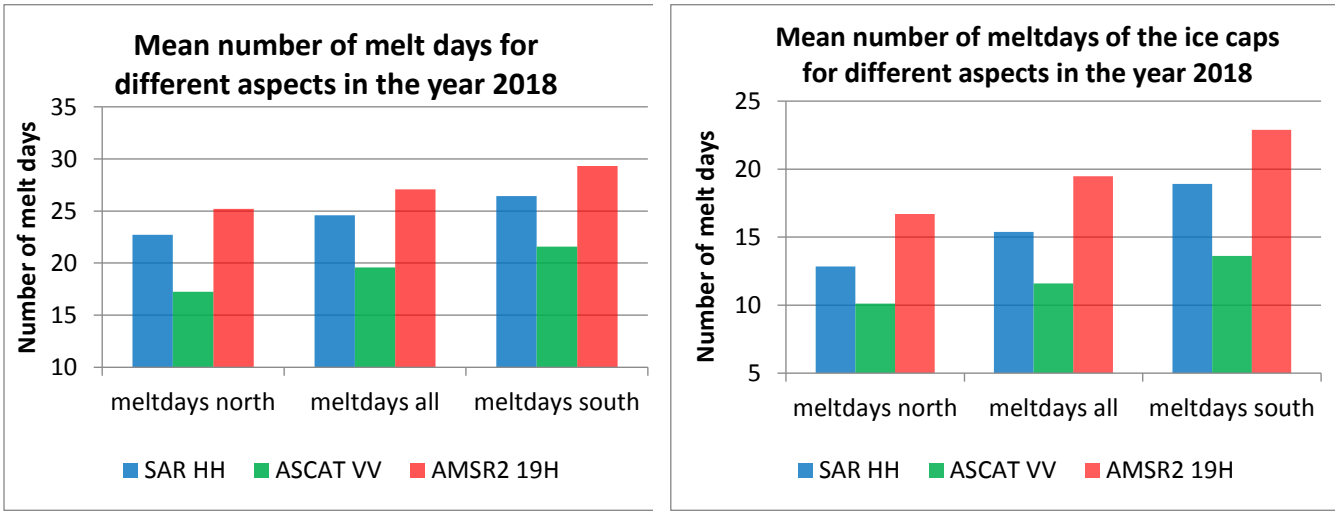


Fig. 43. Left: Mean number of melt days for different aspects on the whole land area (north facing vs. south facing slopes). Furthermore, the three different sensor types (SAR, scatterometer and passive microwave) are compared. Right: Mean number of melt days for different aspects on the ice caps' elevation.

## 4.5. Further analysis

A further comparison between the different sensor retrievals is presented here, as well as an intercomparison for the SAR sensor derived products. Different composite intervals, polarizations and thresholds were juxtaposed and compared. In a last step, melt onset, end and the number of melt days for sea ice is presented.

### 4.5.1. Comparison with spatial temperature estimates

To estimate the quality of the three different sensor products, a comparison with the MODIS land surface temperature can be seen in fig 44. The MODIS melt onset was estimated by assuming the first day in the year with a temperature above 0°C to be melt onset. The similarity of the MODIS product to the SAR onset product is remarkable, even with consideration of the cloud cover frequency. Yet the MODIS product denoted later melt onsets in the highest elevations, but also later onsets at some very low elevations in comparison to SAR.

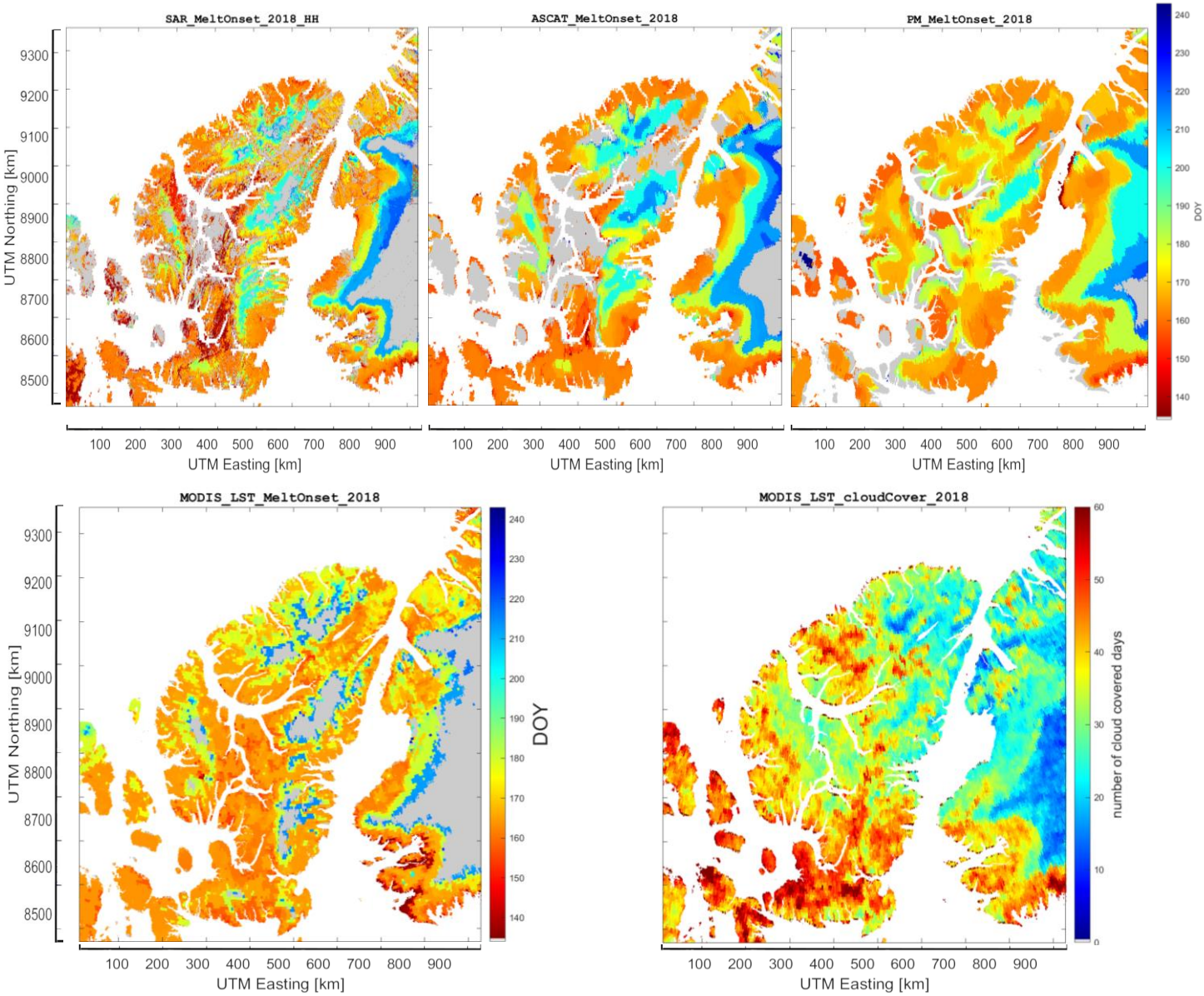


**Fig. 44. Top row: 2018 melt onset products derived from SAR, ASCAT and AMSR2. Bottom left: MODIS land surface temperature derived melt onset product, where melt onset corresponds to the first day with temperature > 0°C. Bottom right: MODIS land surface temperature cloud covered days as a quality indicator. Contains modified Copernicus Sentinel data (2018).**

The mean melt onset found by each sensor type revealed that the SAR HH polarized products were always closest to the MODIS temperature product, with a mean difference of just 1.41 days in these 4 years (Fig. 45). The MODIS products tended to estimate melt onset earlier than the other products.

The largest deviations were between the ASCAT and the MODIS products in the years 2015 and 2018, where ASCAT had significant later mean melt onsets.

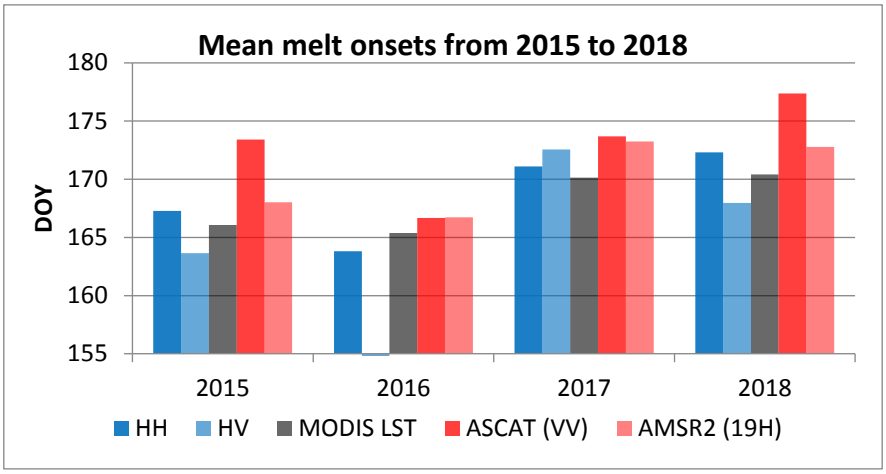


Fig. 45. Mean melt onset from 2015 to 2018 derived by the three different sensor types (SAR, Scatterometer, passive microwave). Additionally, SAR melt onset is divided into HH and HV polarization and the MODIS LST melt onset is shown as a reference.

SAR HH polarization showed a slightly better correlation with the MODIS LST product. It should be noted that for the year 2016, SAR HV polarization is missing, due to a Sentinel-1A HV data gap over the greater part of Ellesmere Island.

### 4.5.2. Spatial Resolution

One of the most important differences between the three sensor types was the spatial resolution. Fig. 46 shows a comparison of the SAR derived melt onset over the ice cap at Barbeau Peak, which is called the northern Ellesmere Icefield. The SAR product was computed using composite backscatter products with 400 x 400 m resolution, while the ASCAT product had more than 10 times poorer resolution (4.45 x 4.45 km). Hence, the SAR product made it even possible to detect different melt onsets in small valleys or on single small glaciers, while in the ASCAT product, these signals were mixed and therefore not discriminable.

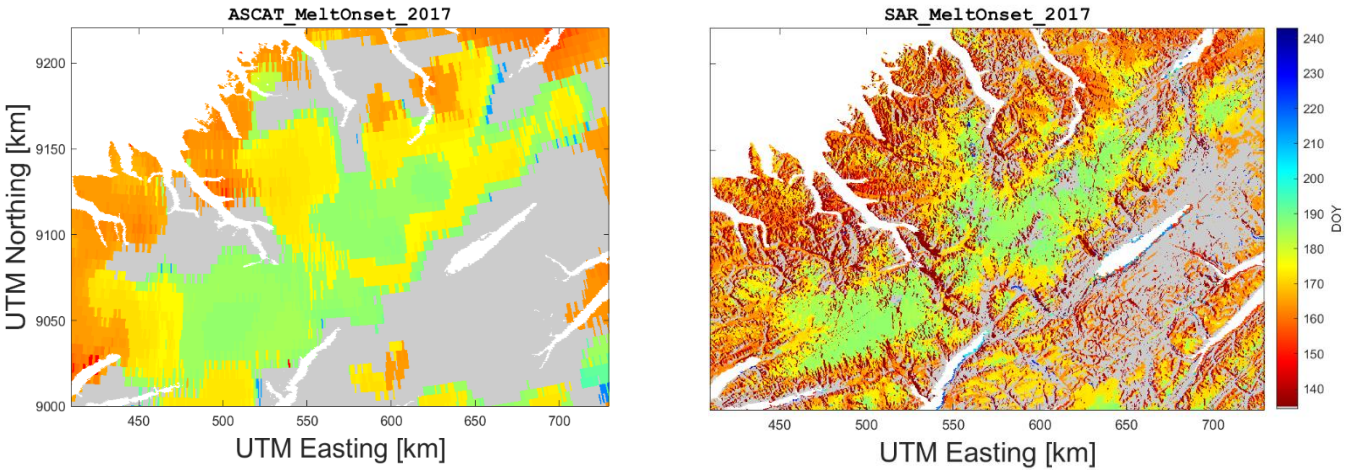


Fig. 46. Spatial subset of the northern Ellesmere Icefield. Shown are the 2017 SAR HH and ASCAT melt onset products. Note the different resolutions of the two products. Contains modified Copernicus Sentinel data (2017).

### 4.5.3. SAR polarizations

As seen in fig. 45, SAR HV polarized data often showed an earlier mean melt onset. Furthermore, SAR HV polarized data also showed later melt ends, especially at lower elevations (Fig. 47).

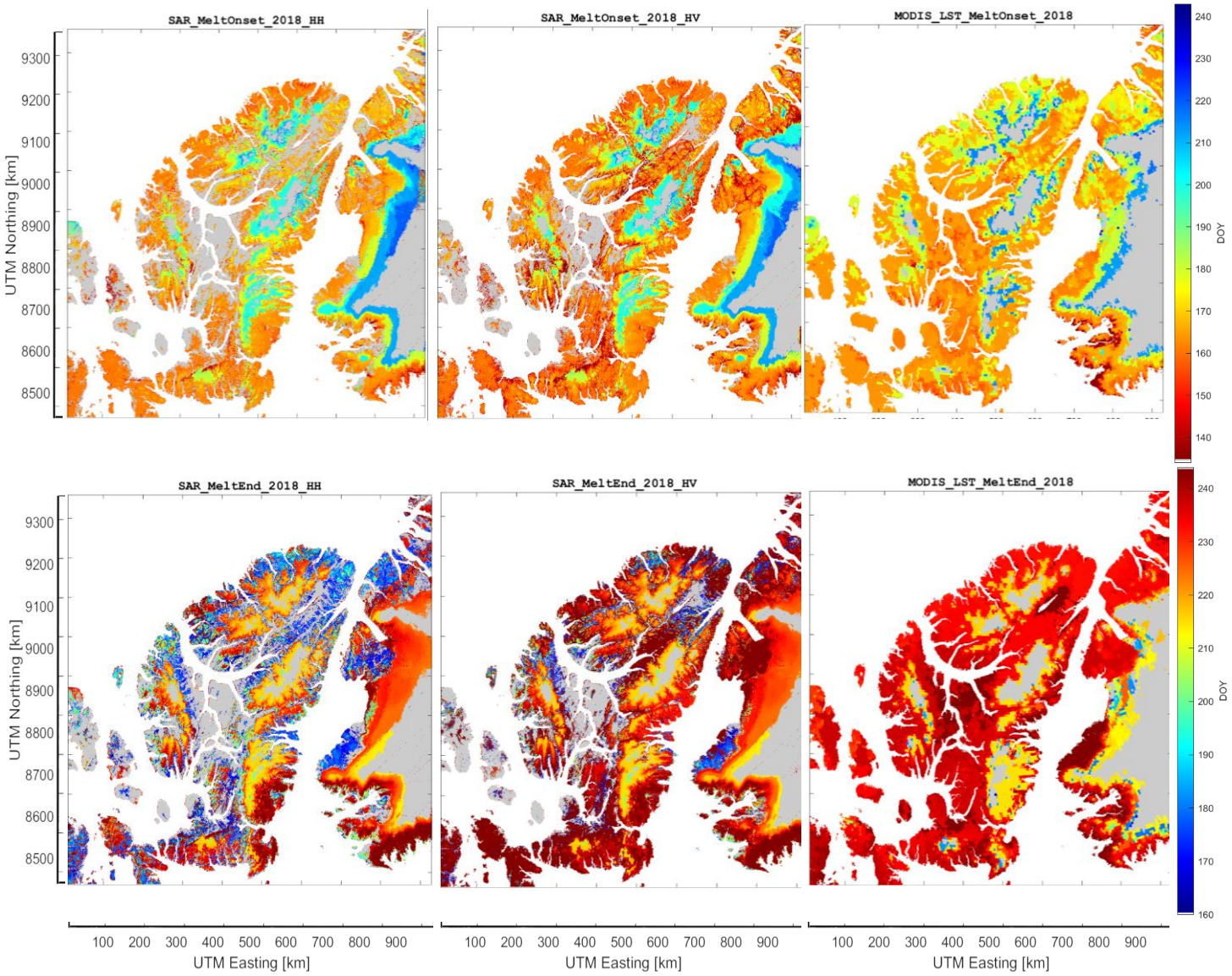


**Fig. 47. Top row from left to right: SAR melt onset 2018 using HH polarization, HV polarization, and MODIS LST first day with temperatures > 0°C. Bottom row from left to right: SAR melt end 2018 using HH polarization, HV polarization, and MODIS LST last day with temperatures > 0°C. Contains modified Copernicus Sentinel data (2018).**

When compared to ASCAT, SAR HH melt onset, end and melt days products were much more similar than were the HV products. ASCAT showed an earlier melt end in the lowlands, as did SAR HH. The SAR HH melt onset product looked more similar to the MODIS LST derived melt onset product. Melt end on the other hand, was more similar for the HV product when comparing it to the MODIS LST product. But we should keep in mind, that the MODIS LST melt end corresponds to the last day in the year with a temperature >0°C and is therefore not dependent on the presence of snow or ice.

### 4.5.4. SAR composite intervals

Shorter composite intervals, like the 1-day S1 & RS2 combined SAR $\gamma_c^0$ composites, resulted in a more complete picture and fewer no onset found areas. Especially in the lowlands, or the grassland class more melt on-

set areas were found. The estimated melt onset in lowlands was often earlier than in the 3-day composites. On the other hand, the shorter composite intervals were also more affected by artifacts (Fig. 48).

The letter a) in fig. 48 shows an example where more melt onset was found using the shorter time interval. Region b) shows the greater susceptibility to artifacts when using the shorter composite interval.

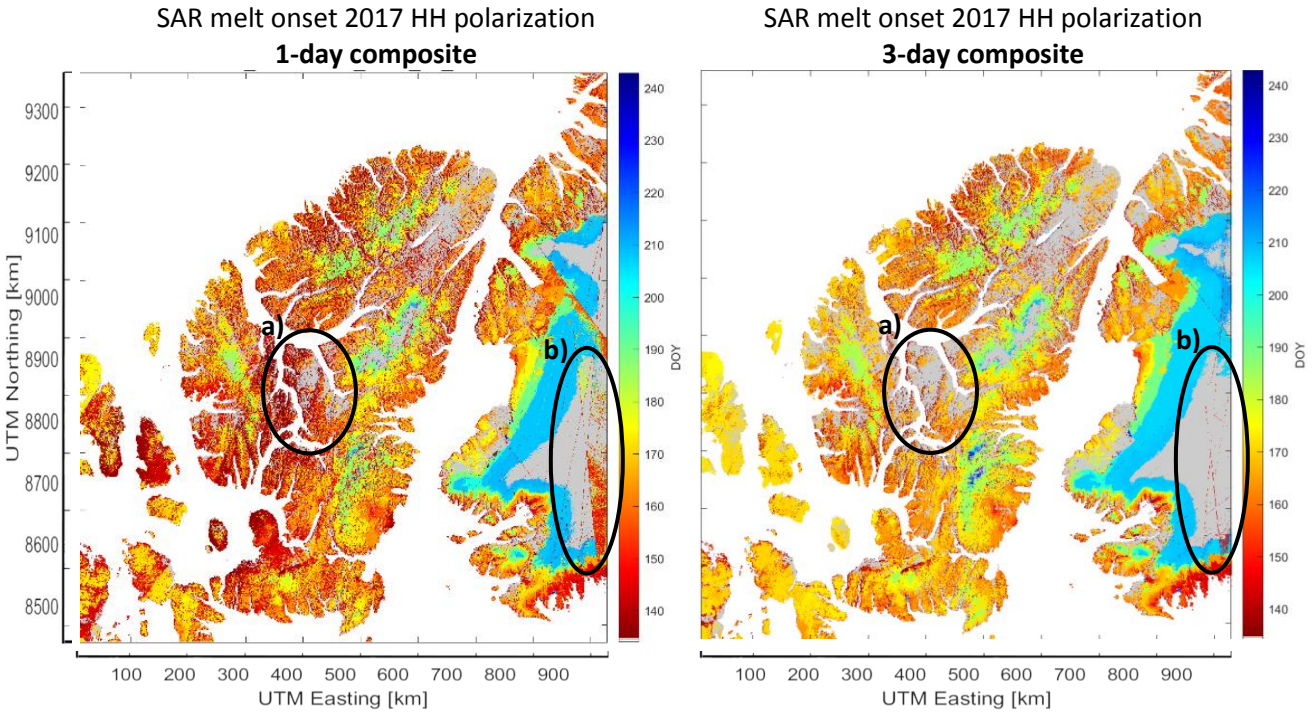


**Fig. 48. Left: SAR melt onset 2017 using the HH polarization and 1-day composite interval. Right: SAR melt onset 2017 using the HH polarization and 3-day composite interval. Contains modified Copernicus Sentinel data (2017). RADARSAT-2 Data and Products ©MacDonald, Dettwiler Associates Ltd. (2017) – All Rights Reserved. RADARSAT is an official trademark of the Canadian Space Agency.**

### 4.5.5. Land cover specific thresholds

Fig. 49 illustrates the mean SAR and ASCAT backscatter values within each MODIS land cover class, indicating the need for an adjusted threshold in the grassland class. A small decrease in backscatter was observable around the 12$^{th}$ July in the grassland class, but the decrease did not exceed the -2dB threshold. The decrease was followed by a rather strong increase in backscatter values of about +3dB.

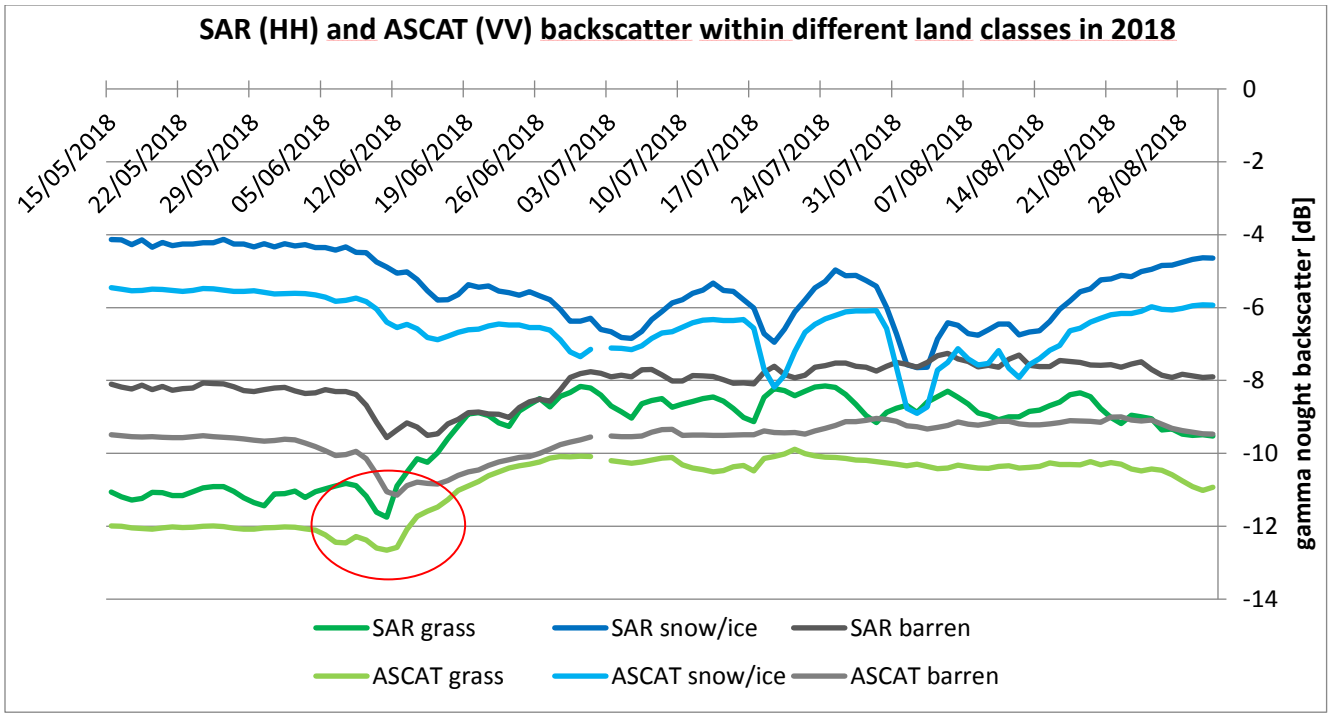


Fig. 49. Mean backscatter values within different land cover classes derived from SAR and ASCAT backscatter images in 2018. The red circle indicates the observable small backscatter decrease within the grassland class in June.

The use of a smaller threshold to detect wet snow in the grassland area resulted in a more complete picture (Fig. 50). A threshold of -1dB resulted in an almost complete picture for the lowlands where melt was probable. An earlier onset was seen in a major part of the lowlands, also seen using shorter composite intervals.

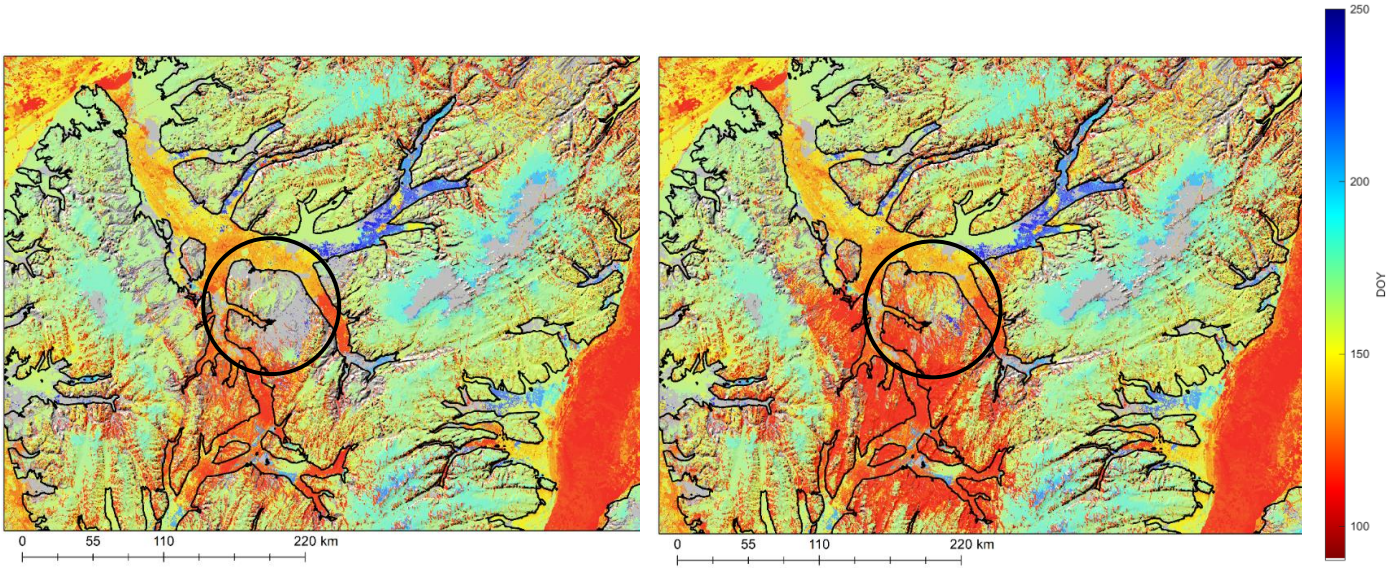


Fig. 50. Left: SAR melt onset 2017 HH 2d, using a -2 dB backscatter threshold to detect wet snow over grassland. Right: SAR melt onset 2017 HH 2d, using a -1 dB backscatter threshold to detect wet snow over grassland. The black circle indicates the area of significant changes between the two products. Contains modified Copernicus Sentinel data (2017). RADARSAT-2 Data and Products ©MacDonald, Dettwiler Associates Ltd. (2017) – All Rights Reserved. RADARSAT is an official trademark of the Canadian Space Agency.

### 4.5.6. Sea ice

As described in 3.2.2., the thresholds to map WSIA are land cover specific, also for sea ice. FYI generally increases in backscatter at the melt onset, MYI decrease in backscatter similar to land areas (Fig. 51), (Barber 2005). Also, the increasing backscatter from the vegetation growth could be seen in the fig 51.

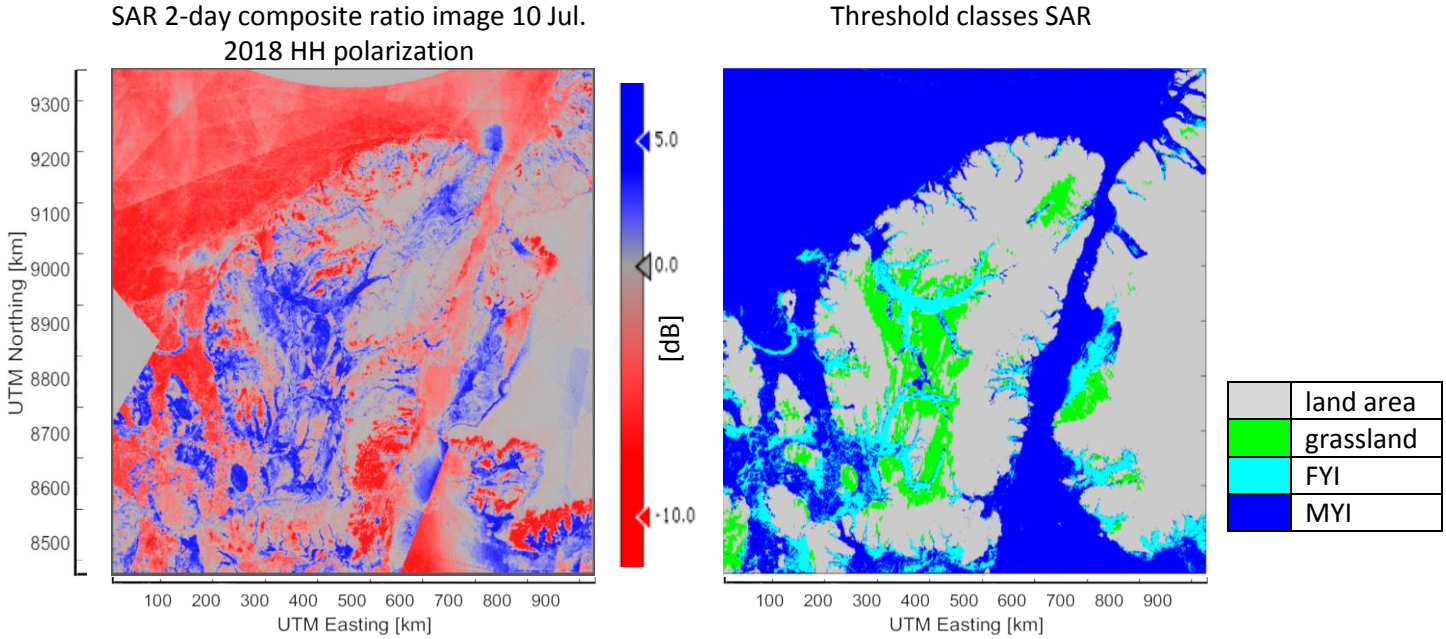


**Fig. 51. Left: SAR 2-day composite ratio image in HH polarization acquired on the 10 July 2018. Right: Land cover classes which need a specific threshold each generated with the mean SAR HH polarization backscatter from 1. April to 30 September and the MODIS land cover class product. Contains modified Copernicus Sentinel data (2017). RADARSAT-2 Data and Products ©MacDonald, Dettwiler Associates Ltd. (2017) – All Rights Reserved. RADARSAT is an official trademark of the Canadian Space Agency.**

Fig. 52 presents melt onset products derived using the three sensor types including sea ice. In all three products, a very early melt onset was observed in the Nares Strait – the water body between Ellesmere Island and Greenland.

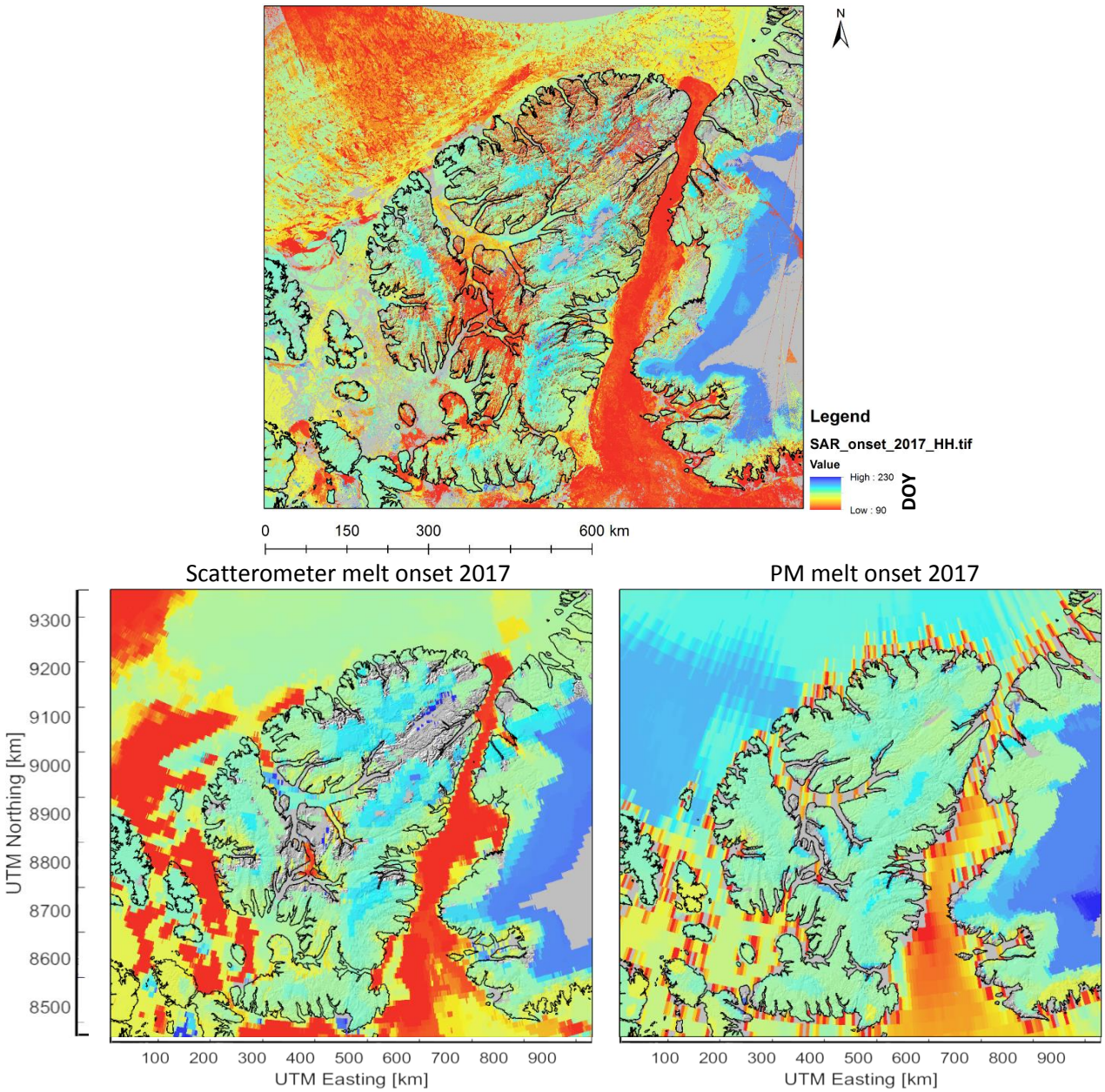


**Fig. 52. Top: SAR melt onset 2017 HH 2d including melt onset on sea ice. Bottom right: ASCAT melt onset 2017 VV including melt onset over sea ice. Bottom right: Passive microwave melt onset 2017 including melt onset for sea ice. Contains modified Copernicus Sentinel data (2017). RADARSAT-2 Data and Products ©MacDonald, Dettwiler Associates Ltd. (2017) – All Rights Reserved. RADARSAT is an official trademark of the Canadian Space Agency.**

Again, SAR and ASCAT showed strong similarities, especially in the Nares Strait. The similarities in the northern and western sea ice were smaller. The passive microwave product by Markus et al., 2009 indicated much later melt onsets in the northwestern sea than the other two products. The lower spatial resolution of the passive microwave product was quickly apparent, causing a lot of areas to be missed near the coast due to mixed pixels.

The similarity in the northwestern sea was much higher for the melt end products (Fig. 53). Only in Nares Strait the PMW algorithm by Markus et al., 2009, denoted sooner melt ends. Therefore, the PMW algorithm generally indicated later melt onsets and earlier melt ends.

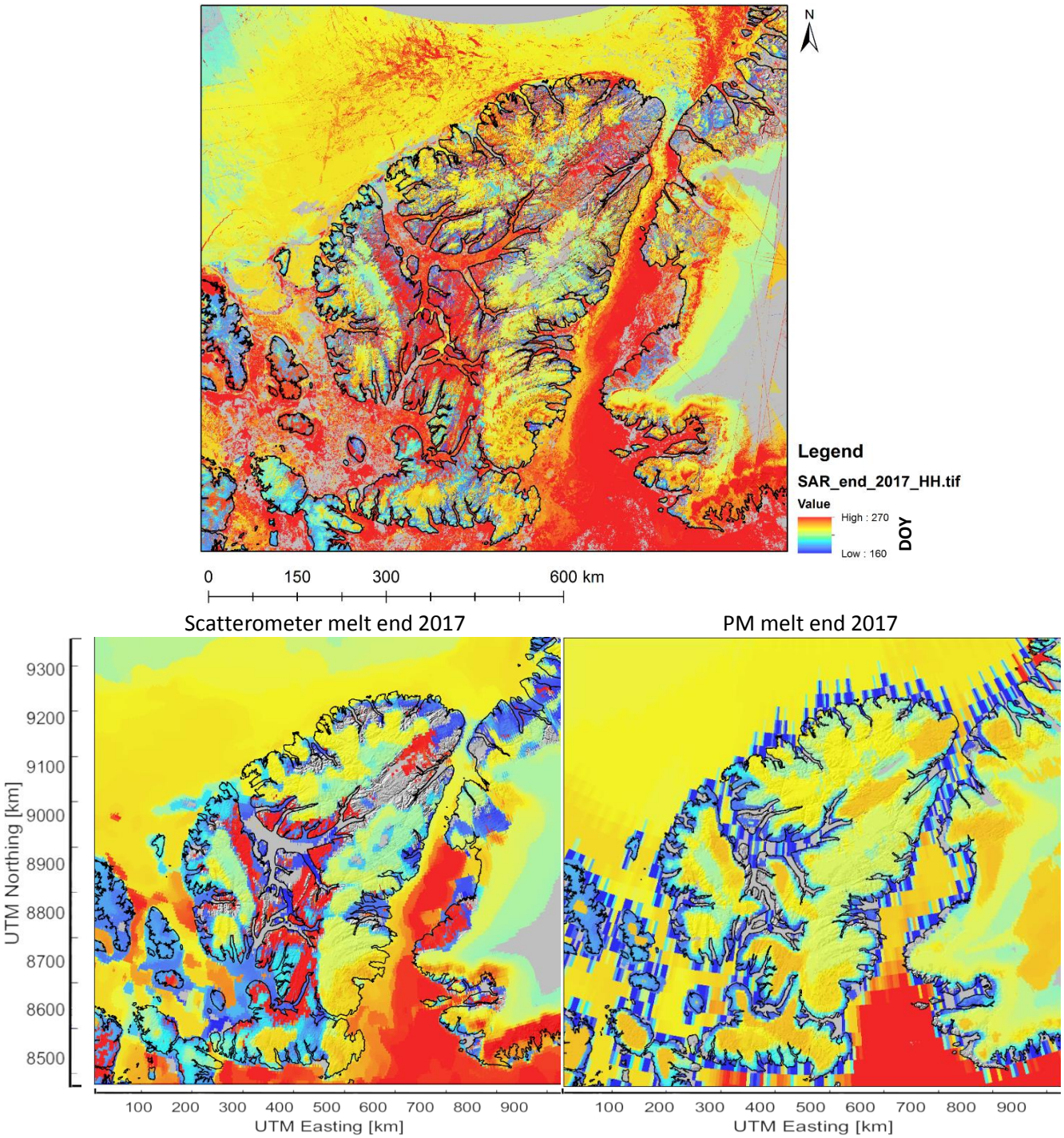


**Fig. 53. Top: SAR melt end 2017 HH 2d including melt onset on sea ice. Bottom right: ASCAT melt end 2017 VV including melt onset over sea ice. Bottom right: Passive microwave melt end 2017 including refreezing for sea ice. Contains modified Copernicus Sentinel data (2017). RADARSAT-2 Data and Products ©MacDonald, Dettwiler Associates Ltd. (2017) – All Rights Reserved. RADARSAT is an official trademark of the Canadian Space Agency.**

Fig. 54 illustrates the difference between the 2018 melt end derived by SAR HH and HV polarization. Using the HH polarization resulted in a more complete image. Using the HV polarization, less melt end was found, for example around Nares Strait.

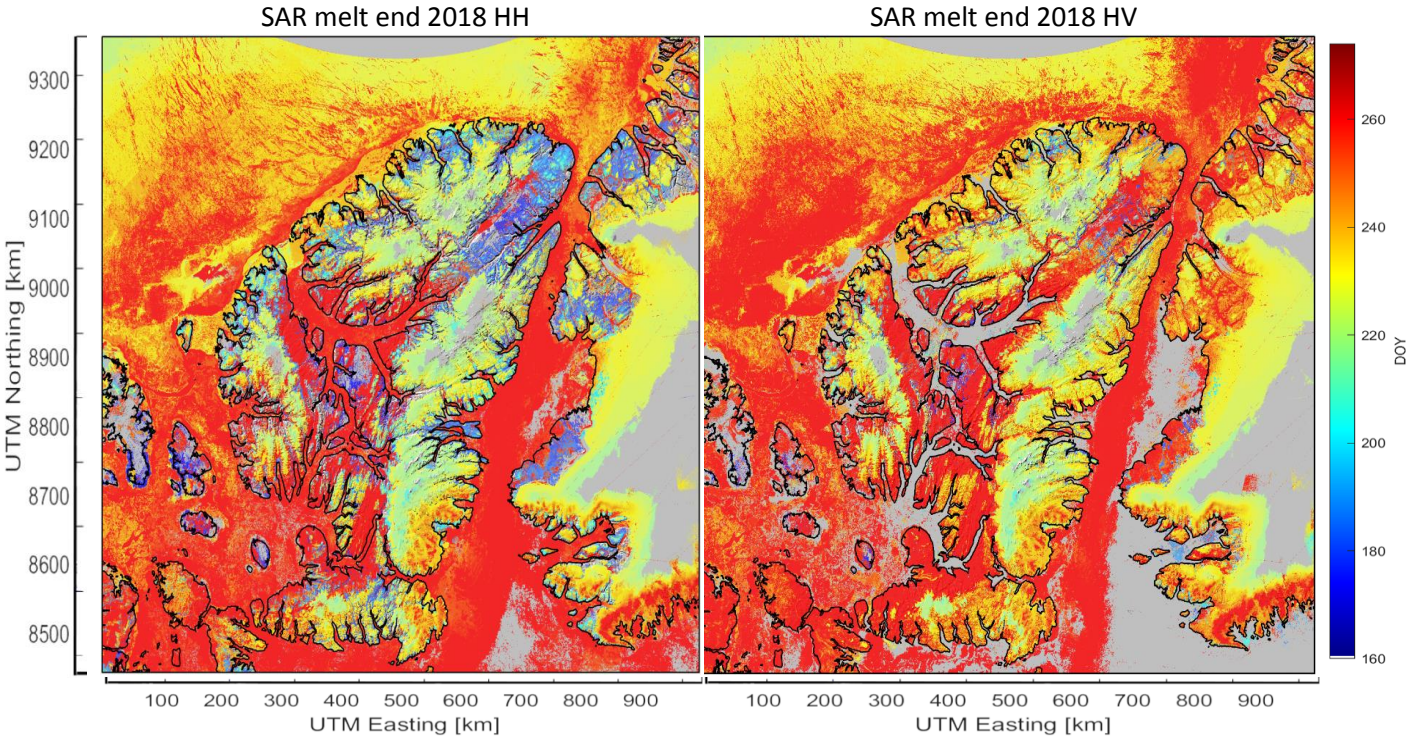


**Fig. 54. Left: Melt end SAR 2018 HH polarization. Right: Melt end SAR 2018 HV polarization. Contains modified Copernicus Sentinel data (2018). RADARSAT-2 Data and Products ©MacDonald, Dettwiler Associates Ltd. (2018) – All Rights Reserved. RADARSAT is an official trademark of the Canadian Space Agency.**

For a detailed analysis of sea ice melt onset derived from SAR, ASCAT and passive microwave, see Howell et al., 2018. They used $\gamma_c^o$ SAR backscatter composites to estimate melt onset of sea ice in the same study area. In their melt onset products, the northwestern part of the ocean showed later melt onsets, comparable to the ASCAT or the PM product here. They used a threshold of -8 dB for multi-year-ice in SAR scenes, whereas here, a threshold of -5 dB was taken. Their cold reference scene was generated by using the April mean, in our study a mean of January and February was used. The different threshold and the different reference time range could explain the earlier melt onset of the SAR product presented here.

# 5. Discussion

Remote sensing of snow and ice has a long-lasting history and is a powerful tool, especially in remote areas such as the Arctic. Passive microwave and scatterometer data have been used frequently in mapping wet snow or estimating melt onset of snow or ice areas (Drobot and Anderson, 2001), (Belchansky et al., 2004), (Howell et al., 2006), (Markus et al., 2009), (Wang et al., 2011), (Bliss and Anderson, 2014), (Mortin et al., 2014). Their high temporal resolution and the large areal coverage made them to the instruments of choice. However, their spatial resolution limited the investigation to large study areas such as the whole arctic. Smaller investigations, such as islands or even single valleys were not viable. SAR data with a higher spatial resolution has been used to detect wet snow areas as well, but the temporal resolution was often a limit in finding melt onsets. Moreover, the influence of different viewing geometries between passes and sensors was problematic in creating a consistent time series (Howell et al., 2018).

Now the concept of $\gamma_c^0$ allows us to overcome the disadvantages of SAR compared to PM or scatterometer (Howell et al., 2018). An improved temporal resolution due to multi-sensor and multi-pass products and corrected viewing geometries were achieved using $\gamma_c^0$ backscatter composites. The comparison of SAR derived WSIA and melt onset/end/number of melt days products with results from PM and scatterometer proved the high potential of SAR $\gamma_c^0$ composites.

The following chapter discusses the results presented in chapter 4. The results are analyzed and compared with previous scientific researches.

## 5.1. WSIA mapping

### 5.1.1. Passive Microwave (PM) WSIA mapping methods

In chapter 4.1.1. we saw that only the single band threshold method showed plausible results in mapping the WSIA with passive microwave brightness temperatures. The diurnal method proposed by Ramage and Isacks (2002) clearly underestimated the WSIA. Ramage and Isacks (2002) applied their method in the southeastern Alaskan icefields. The southeastern Alaskan icefields are located approximately 20° further southwards of Ellesmere Island, and are therefore southern of the polar circle. The method detects melt onset only when the DAV (diurnal amplitude variation) exceeds a threshold, which may have been problematic here. Arctic summers show lower daily temperature variations, because it is always daytime (Fig. 55). Sunlight is present for the whole day. Foster et al., 2011 also applied this method for the whole arctic area, but they also used scatterometer data to improve their product. Using passive microwave data alone, the used thresholds might need to be adjusted when using it for Arctic or Antarctic areas.

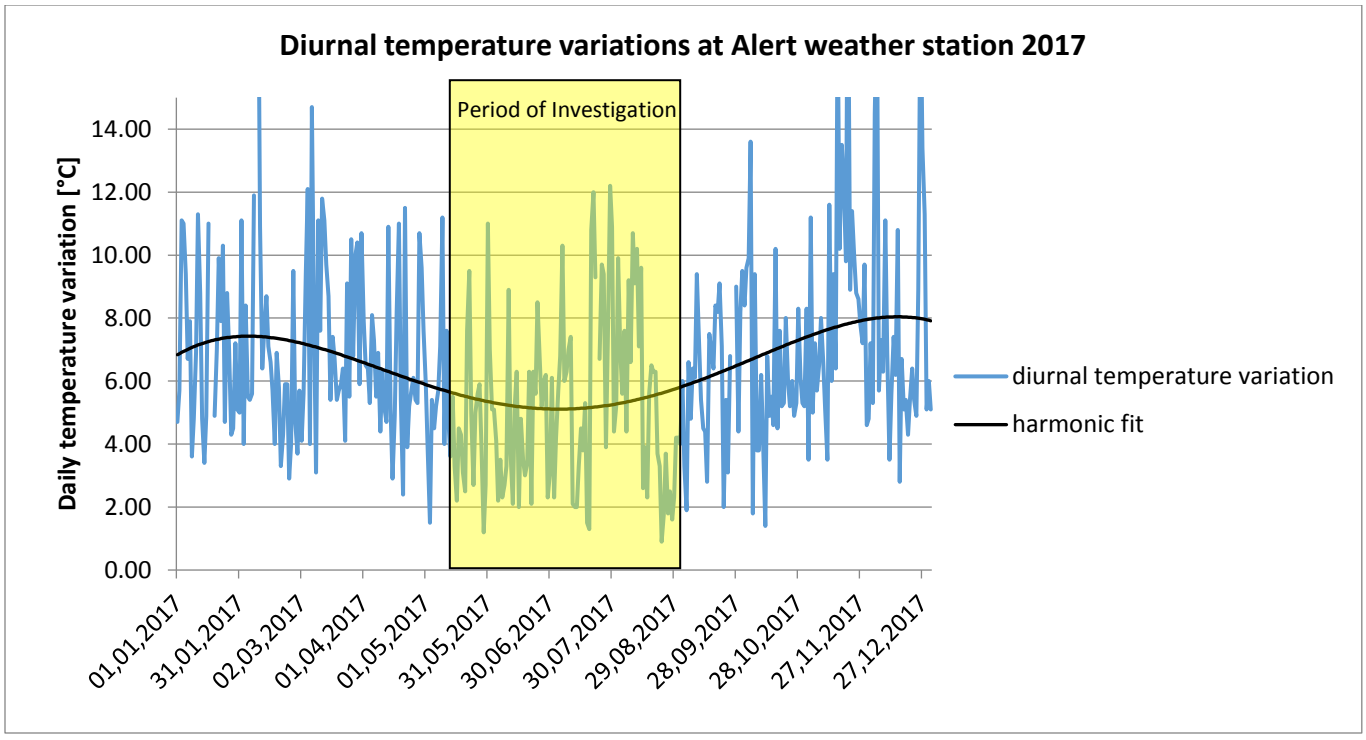


**Fig. 55. Diurnal temperature variations throughout the year 2017. The blue curve illustrates the difference of the minimum and maximum air temperature measured at Alert weather station. The black curve presents a harmonic (polynomial) fit through the measured variations.**

The FY3C algorithm showed smaller WSIA on warm days than on cold days. Liu et al., 2018 tested this method along with six other algorithms for its capability to map snow extent in China. Along their tested algorithms, the FY3C showed the best accuracy. However, Liu et al., 2018 did not evaluate the accuracy of the sub-categories in the algorithm (thick and thin dry snow, thick and thin wet snow). Hence, the FY3C algorithm might hold a good accuracy in mapping the overall snow extent, but may lack in delineating wet from dry snow. The fact that the FY3C algorithm showed the highest areas of wet snow in wintertime indicates that the sub-categories thin and thick wet snow also detect major parts of dry snow areas.

The single band threshold method showed reasonable results in mapping WSIA. The threshold of +30°K applied here was taken because of the similarity to the SAR and scatterometer WSIA results. However, this threshold might need to be further adjusted, since real ground truth measurements of snow liquid water content were not available. Furthermore, the threshold was adjusted for this specific study site, where in other areas it might need to be further adjusted.

### 5.1.2. WSIA derived from SAR, Scatterometer and PM instruments

The WSIA results showed a strong correlation with temperature and snow depth data for all the three different sensor types, for example a correlation coefficient of r= 0.74 for SAR HH polarization with temperature data. WSIA increased with rising air temperatures or decreasing snow depth. Especially at the first day of mean air temperatures above 0°C a rapid increase in WSIA was observed. Furthermore, at low mean air temperatures (e.g. < -2°C) almost no WSIA was present. Therefore, all sensor types were capable of mapping WSIA up to a certain accuracy and the results were trustworthy.

SAR and scatterometer showed a high resemblance to each other, more than to the PM single band threshold method. Since both sensor types deliver C-band backscatter products, and were processed with the same

method and the same thresholds, this is not surprising. The only difference between them was the spatial resolution, the polarization and the pre-processing, where SAR images were composited with the concept of $\gamma_c^0$. Some bigger differences in the WSIA percentage curve (Fig. 29) between SAR and scatterometer could be explained by missing SAR data. At some dates the SAR composite images were not spatially complete, especially in 2015 and 2016, where only Sentinel-1A images were available and no Senstinel-1B (www.earth.esa.int). Other differences were probably caused by the different spatial resolution. SAR images had a resolution of 400 m, which was superior in rough terrain investigations compared to ASCAT with a 4.45 km resolution. The coarser resolution resulted in more mixed pixels, where different land covers, heights or aspects were merged together to one pixel. The third potential reason for variations is the polarization. SAR images were available in HH or HV and ASCAT in VV polarizations. Surface types and materials react differently in other polarizations according to their 3D-structure and dielectric properties (Ulaby et al., 1981). The last explanation for differences is the pre-processing. SAR images were pre-processed using the concept of $\gamma_c^0$. By applying this concept, the SAR images were terrain corrected, in comparison to the ASCAT images. The terrain correction removes the backscatter signal caused by topography and viewing angles, resulting in backscatter only caused by other factors, like material properties (Ulaby et al., 1981), (Small 2011), (Small 2012). However, using the change detection method, where the backscatter difference to a reference is calculated, a terrain correction should not make any difference according to Nagler et al., 2016. At least this is the case, when repeat passes and similar viewing angles are considered. Fig. 56 shows density plots as a comparison between SAR HH $\gamma_c^0$ backscatter composites and ASCAT VV backscatter images. The density plots are made for two dates and two different land classes (grassland and snow/ice). If both images would have shown the same backscatter for each pixel, the density would perfectly align along the reference (blue line). On the 15-17 May the correlation of SAR with ASCAT was quite strong. The highest density was aligned with the same gradient as the reference line. Therefore, in winter time with mostly dry snow and ice conditions, the resemblance between SAR and ASCAT was high. In contrast, on the 04-06 July the resemblance was low. In the grassland class, the density was not aligned; it was circle-shaped. The correlation in the snow class was only given for some very bright pixels (backscatter values > -5 dB). For the darker pixels, the resemblance decreased, where especially SAR tended to shift towards lower backscatter values, which was probably caused by the higher spatial resolution.

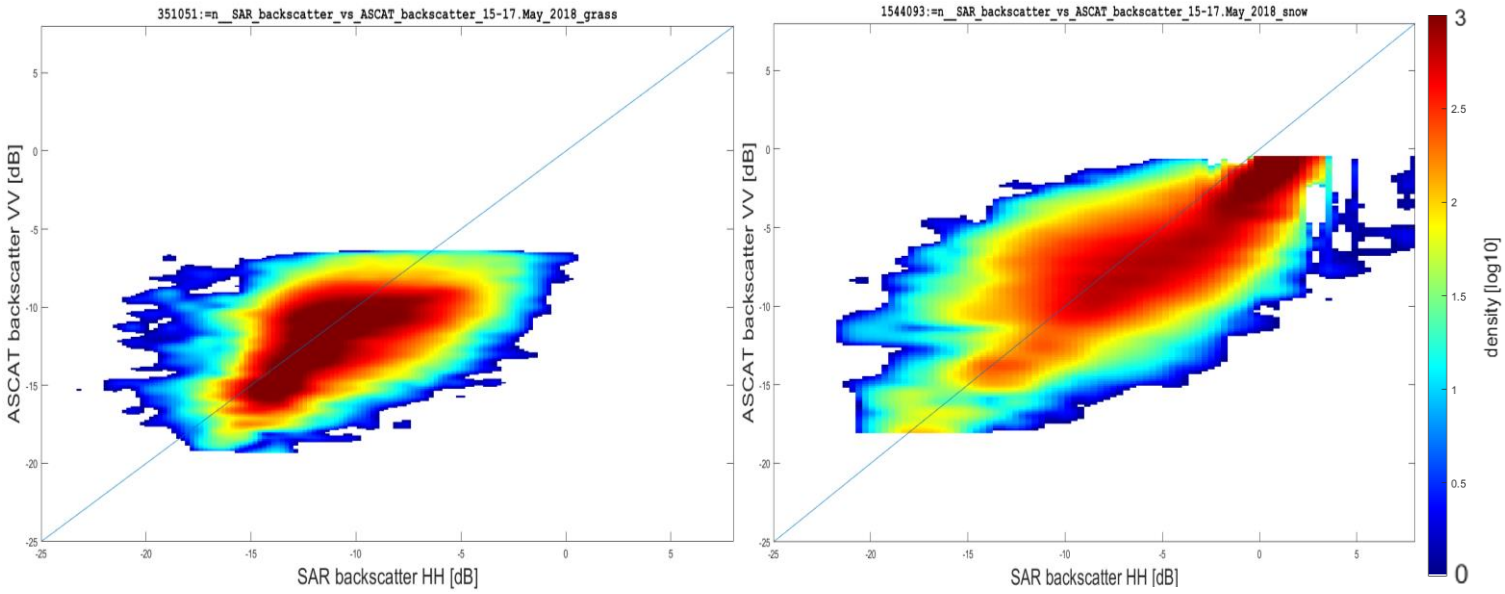

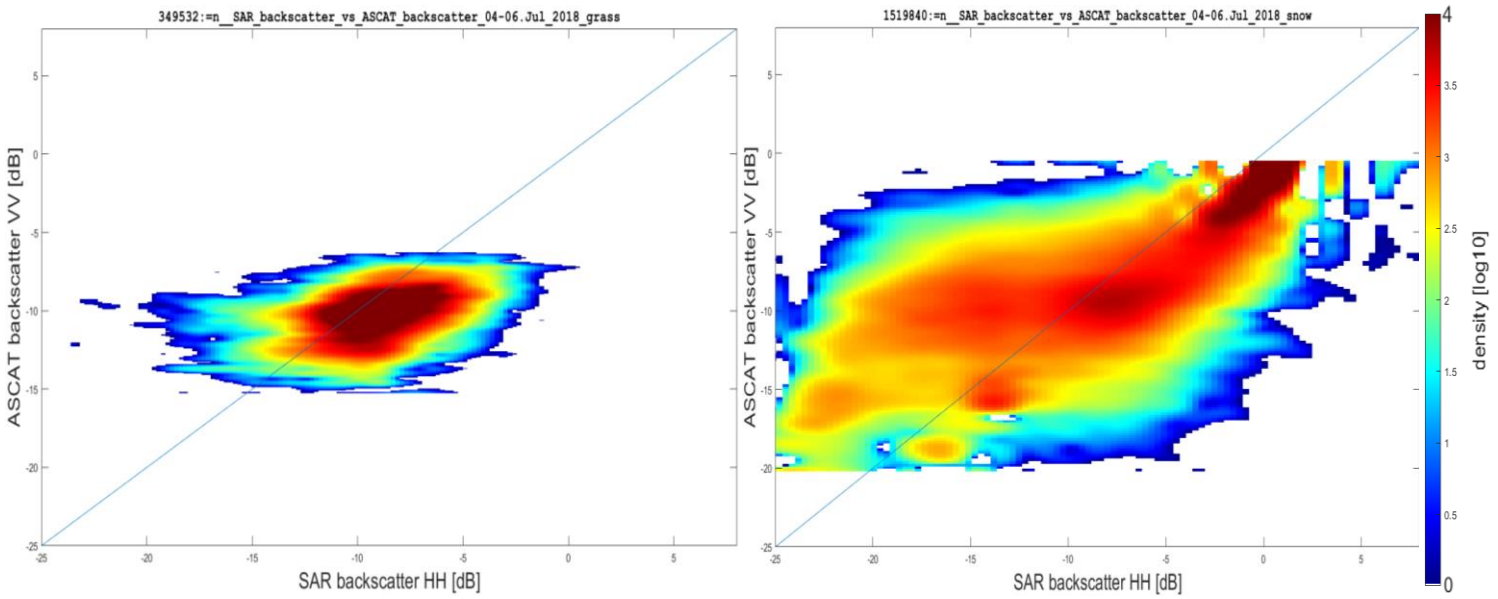


**Fig. 56. Density plots of the backscatter images of SAR HH and ASCAT VV. Top: Backscatter density plot on between the 15 May and 17 May 2018, for the grassland class and the snow/ice class. Bottom: Backscatter density plot on between the 04 Jul and 06 Jul 2018, for the grassland class and the snow/ice class.**

WSIA derived from PM showed a high resemblance to SAR and ASCAT too, but some peaks were significantly higher for PM. Most likely the PM algorithm had a worse ability to delineate wet-snow from no-snow. Wet snow and dry/frozen soil have similar brightness temperatures, they both appear as warm (Amlien, 2008), (Mätzler et al., 1982). The brightness temperature of snow increases as soon as the snow is wet, but other areas also increase in brightness temperature with increasing surface temperatures, because the brightness temperature and the physical surface temperature are correlated (Zwally and Gloersen, 1977), (Liu et al., 2006). Furthermore, the applied method with PM used the 19 GHz band, as suggested by Liu et al., 2006, which is less sensitive to liquid water than the C-band (~ 5.3 GHz) used by SAR and ASCAT. Smaller frequencies are more sensitive to the influence of liquid water in the snowpack (Stiles and Ulaby, 1980). Therefore, it is possible to exceed the +30°K threshold by increasing the surface temperature of no-snow areas. That was the reason of adding a snow extent mask in the PM WSIA algorithm, where only areas with a snow depth >0m should be addressed. However, the PM single band threshold still showed some higher peaks, but not as high as before. The snow depth product was an ERA5 product, with a spatial resolution of 0.25°. This resolution might be insufficient, and using a better snow extent mask, the difference to the ASCAT and SAR products could possibly be decreased further.

The comparison with another ERA5 product, the snowmelt estimates showed less correlation than with the temperature data. Especially in 2015 the difference in WSIA in mid-summer was large. The ERA5 snowmelt product indicated almost no WSIA, while all three sensor types used in this study showed a maximum. The number of melt days for the ERA5 product and the ASCAT product can deliver an explanation to this difference (Fig. 57). The ERA5 snowmelt product showed a significant lower number of melt days for the ice caps. In mid-summer, almost just these ice caps showed WSIA in the SAR and ASCAT products. Therefore, these areas were missing in the ERA5 snowmelt resulting in the big difference. Ice areas are probably masked out in the ERA5 product considering only snow, or snow on ice.

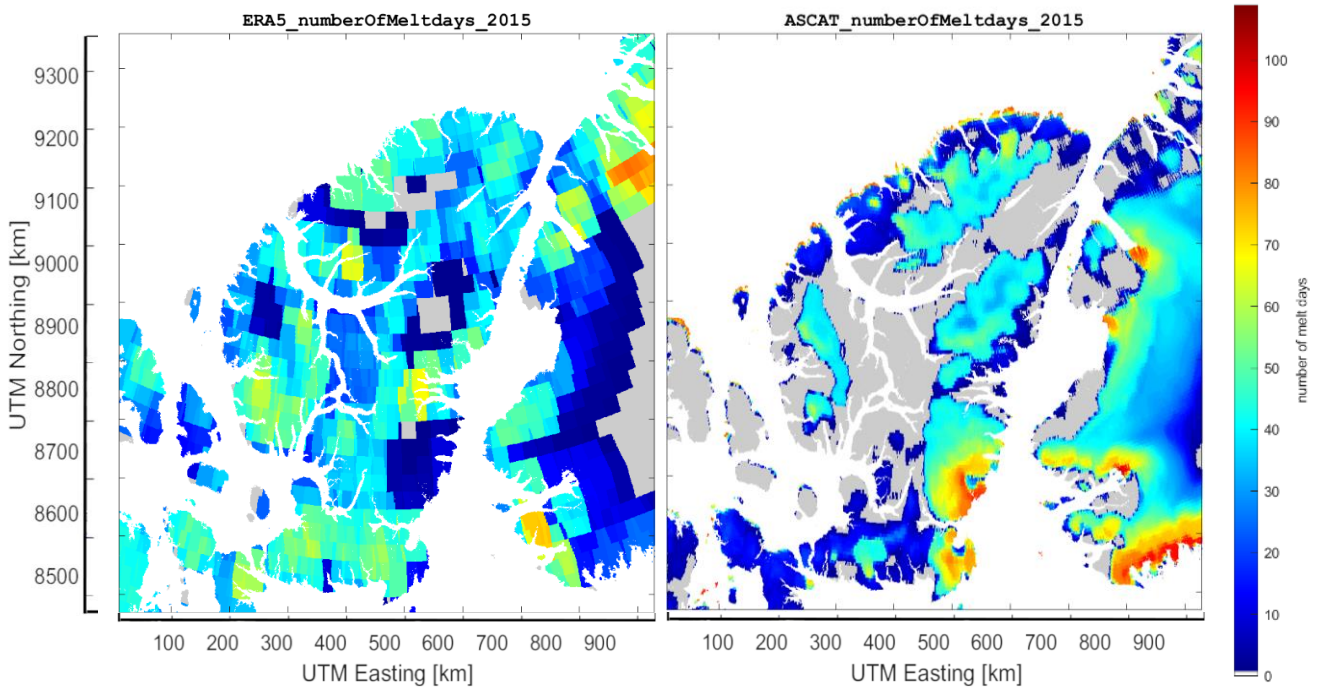


Fig. 57. Left: Number of melt days in 2015 derived from the ERA5 snowmelt product. Right: Number of melt days in 2015 calculated with ASCAT data.

Not only the ice caps showed large differences in WSIA between the ERA5 product and SAR, scatterometer and PM, but also the lowlands. ERA5 showed more melt days in the lowlands than for example SAR (Fig. 58).

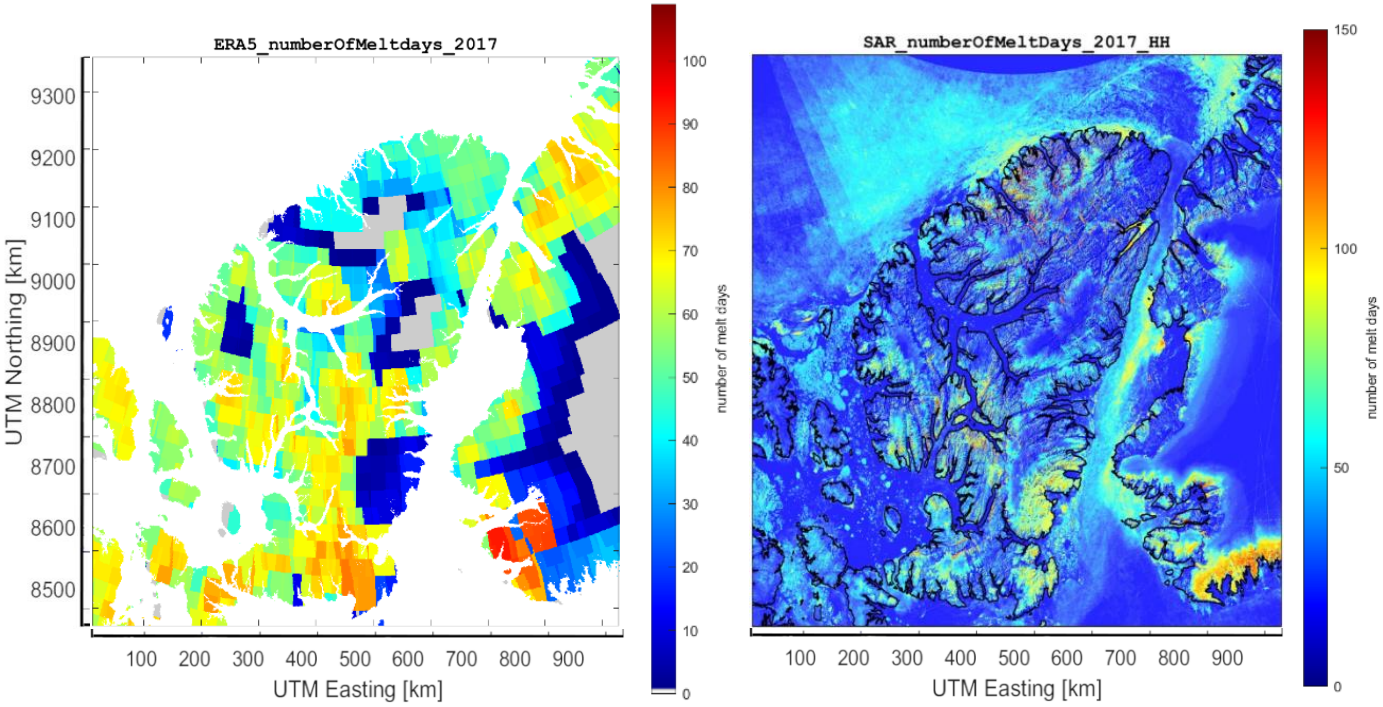


Fig. 58. Left: Number of melt days in 2017 derived from the ERA5 snowmelt product. Right: Number of melt days in calculated with SAR HH polarized data. Note the different color scaling. Contains modified Copernicus Sentinel data (2017). RADARSAT-2 Data and Products ©MacDonald, Dettwiler Associates Ltd. (2017) – All Rights Reserved. RADARSAT is an official trademark of the Canadian Space Agency.

MODIS optical false color composites supported the SAR or ASCAT results rather than the ERA5 product. The MODIS false color images indicated fast melted snow areas around Lake Hazen, while the ERA5 product still indicated snowmelt 20 days later (Fig. 59).

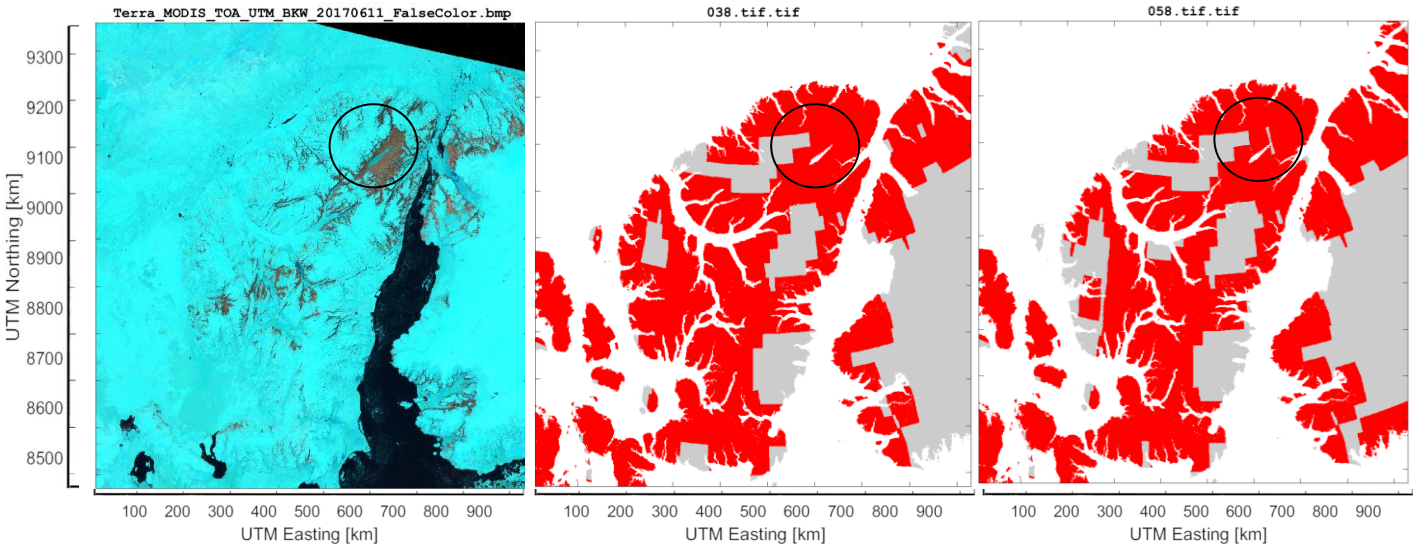


11-21.06.2017 21.06.2017 11.07.2017

**Fig. 59. Left: Optical MODIS false color composite (R= SWIR, G= NIR, B=RED). The images used where acquired between 11.06.2017 and 21.06.2017. Middle: ERA5 WSIA on the 21.06.2017. Right: ERA5 WSIA on the 11.07.2017.**

Therefore, the WSIA products created in this study are considered to be more accurate and valuable than the ERA5 snowmelt product. First, the spatial resolution is much better, especially in the SAR derived products. Second, ice areas are most likely excluded in the ERA5 product, which is an important surface feature. And third, the snowmelt in lowland areas is clearly overestimated in the ERA5 product.

## 5.2. Melt onset

In chapter 4.2. the melt onset products derived by the three different sensor types were presented. Melt onset estimates showed reasonable results for all three sensor types, because a clear increase in melt onset dates was visible with an increasing height. Higher elevations typically have lower air temperatures and therefore a later melt onset (Mote and Anderson, 1995). The earlier melt onsets for SAR in 2017 and 2018 in the highest classes were most probably caused by a low number of pixels in these classes and therefore by a large uncertainty. Furthermore, south facing slopes showed earlier melt onsets than north facing slopes, due to a stronger solar irradiance (McCutchan and Fox, 1986).

All melt onset products created showed earliest melt onsets in the year 2016. The temperature data supported these findings, because 2016 was the warmest year in the time period of investigation (see measured temperature in fig. 29).

The reason of significant later mean melt onsets for ASCAT compared to SAR and PM could not be completely explained by later melt onset values alone, because SAR and ASCAT showed a similar WSIA percentage curve. However, the number of pixels at higher elevation could give an additional explanation, where ASCAT mapped more WSIA at high elevation. These pixels typically had a very late melt onset, because of the lower temperature in these heights. When calculating the mean melt onset, these pixels are shifting the melt onset towards a later mean.

PM generally showed earlier melt onsets in high elevations compared to SAR and ASCAT. Most likely the low spatial resolution lead to mixed pixels, containing earlier melt onsets from lower elevations.

Fig. 60 presents an example for a melt onset map derived using SAR HH polarization for the year 2018. Some spatial features shall be discussed in more detail here:

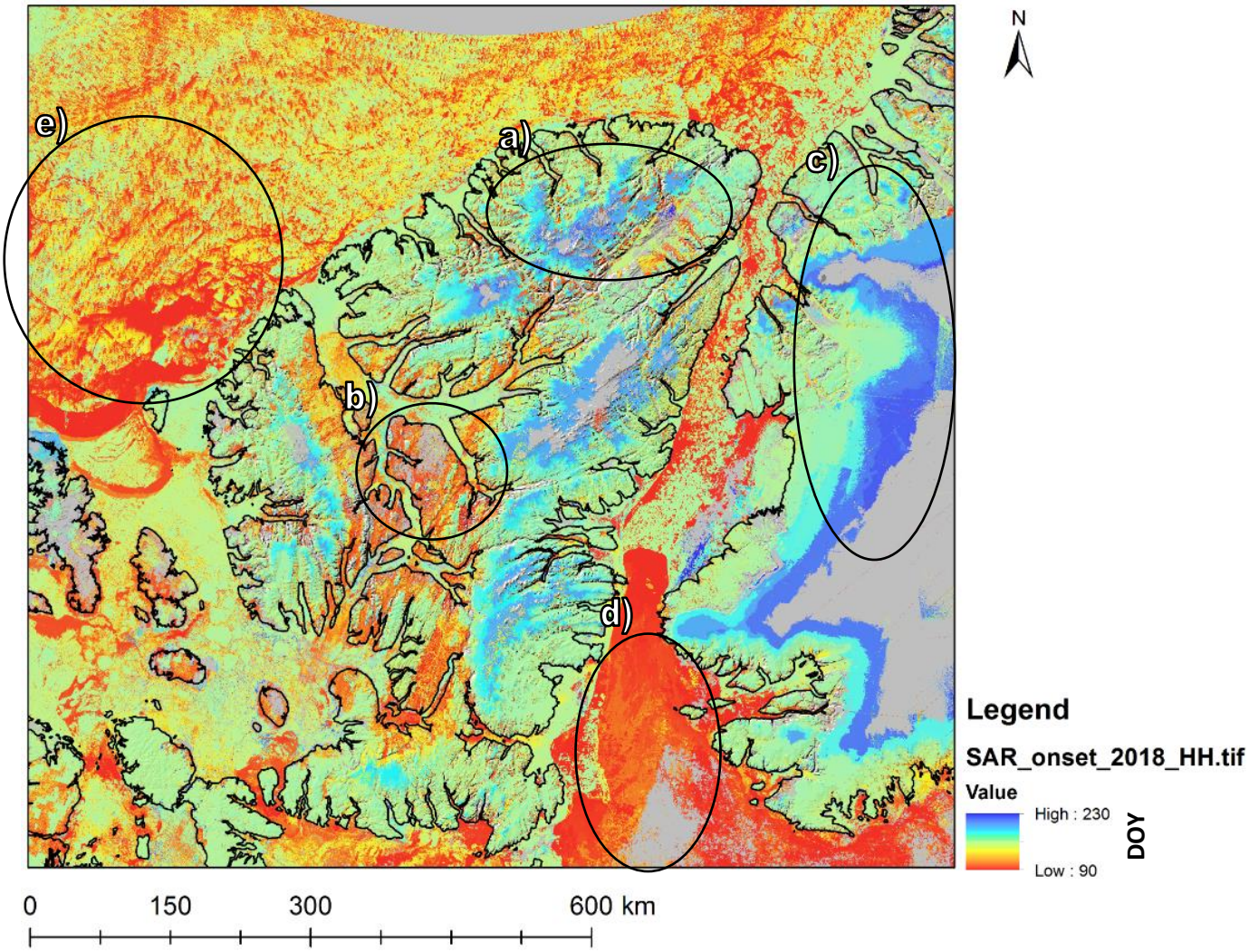


**Fig. 60. Melt onset estimated with SAR HH polarization in the year 2018. Letters a) to e) indicate specific areas being discussed. Contains modified Copernicus Sentinel data (2018). RADARSAT-2 Data and Products ©MacDonald, Dettwiler Associates Ltd. (2018) – All Rights Reserved. RADARSAT is an official trademark of the Canadian Space Agency**

a) The circle indicates the location of the northeastern Ellesmere Icefield. A significant later melt onset was present for higher elevation. Furthermore, in the highest terrain, for example at Barbeau Peak, no melt processes were registered. Both these findings indicate the lower air temperature at higher elevations.

b) The lowlands near Eureka showed one of the earliest melt onsets on land. Some areas showed a missing onset in that region even with using a different threshold for the grassland class and a shorter composite interval of 2 days. Nevertheless, the missing onsets in these regions could be decreased compared to the – 2 dB threshold and a 3-day composite interval leaving only a small part of missing

onsets. In the southern part of the indicated area small ridges are visible in the terrain with a later melt onset, again here, indicating higher elevation and therefore lower air temperatures on the ridges.

c) Adjacent Greenland showed the latest melt onset values in this product. Low air temperatures due to high elevations could explain the late onset. Furthermore, a major part of inner Greenland showed no onset estimates, also indicating cold temperatures leading to no melt processes. Looking closer even single glaciers can be distinguished, which often had an earlier melt onset compared to the surrounding terrain. This was important for two reasons: First, the spatial resolution of SAR was good enough to distinguish such small-scale features. Second, the glaciers presumably showed earlier melt onset, because they are located in valleys and therefore at lower elevations with higher air temperatures.

d) Nares Strait showed the earliest overall melt onsets. Also in the optical MODIS images the early onset was visible, Nares Strait was ice-free very early. In 2018 also the SAR HH product showed quite a lot of missing onset values in the south of Nares Strait – probably it was already ice free at the beginning of the observation period (1. April).

e) A very early onset was also observed in the northwestern ocean. In the PM product, such an early melt onset was not visible and in the ASCAT product the area of early onset was smaller. Howell et al., 2018 used another threshold for multi-year-ice (MYI), namely one of -8 dB instead of -5 dB. That area is presumably dominated by MYI and therefore the melt onset would be later when using the -8 dB threshold. Additionally, sea-ice structures were visible in that area. Probably these structures were really caused by melt processes, but they could also have derived from the topography of the ice. The changing structure of the moving ice could change the backscatter like a mountainous topography on land. Such influences would be problematic because they do not represent real melt processes (Howell et al., 2018), (Zhou et al., 2019).

## 5.3. Melt end

Like melt onset products, melt end estimates were feasible. Higher elevations showed an earlier melt end, due to lower air temperatures. However, the very low elevation often showed a very early melt end. That can be explained by completely melted snow. As soon as no snow is left, or the temperatures are cold again, the melt end is reached (Fig. 61). The passive microwave results supported this finding, because it was less affected by completely melted snow, due to the lacking capability of delineating wet-snow from no-snow. Therefore, the PM melt end product is more like a refreezing onset product, similar to the MODIS LST melt end.

However, even PM showed an n-shaped pattern of melt end, this can be explained by the coast. The coast often showed early melt ends in the passive microwave result. Most likely the early melt end is due to mixed pixels at the coast, where brightness temperatures are merged by land and sea signals.

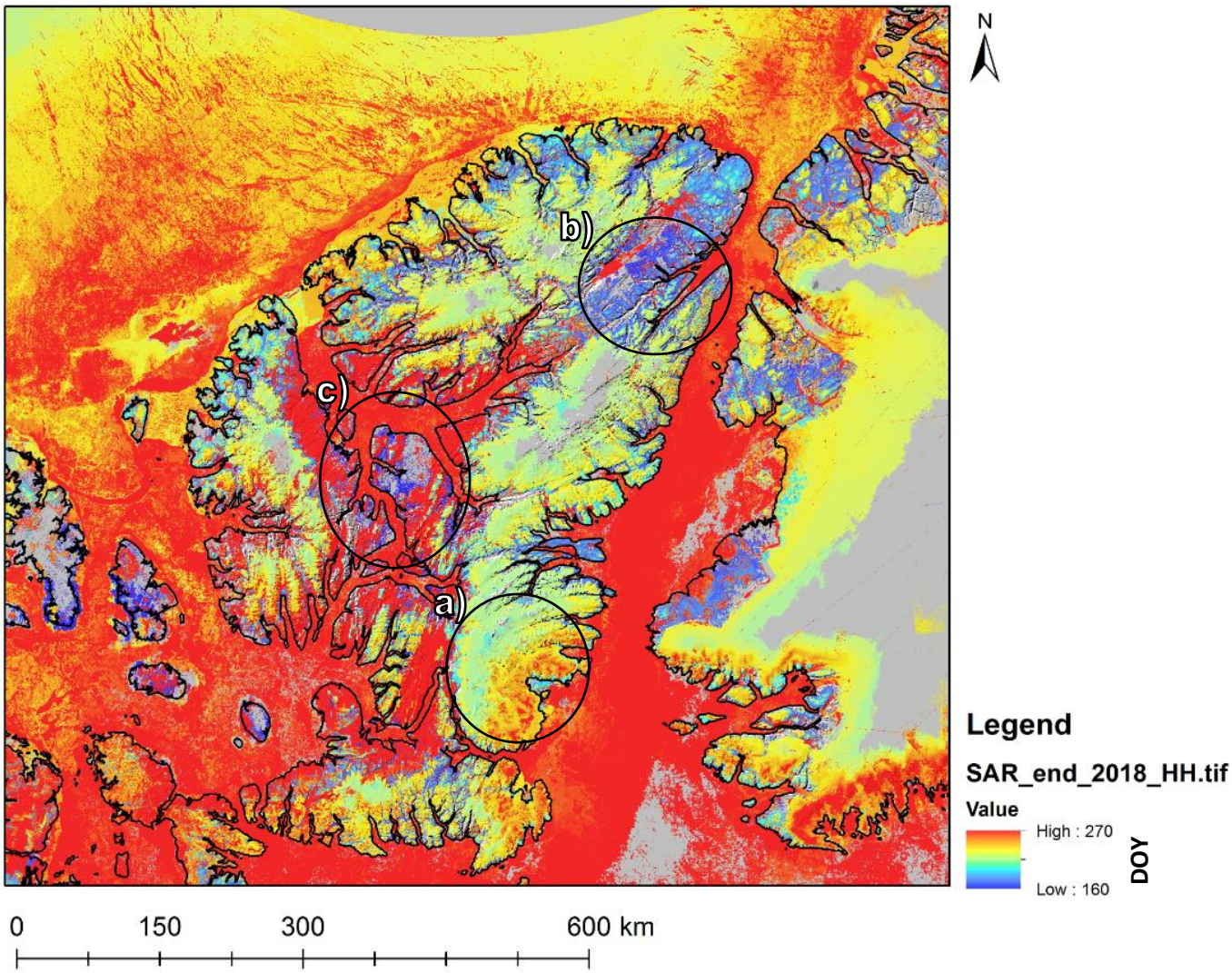


Fig. 61. Melt end estimated with SAR HH polarization in the year 2018. Letters a) to c) indicate specific areas being discussed. Contains modified Copernicus Sentinel data (2018). RADARSAT-2 Data and Products ©MacDonald, Dettwiler Associates Ltd. (2018) – All Rights Reserved. RADARSAT is an official trademark of the Canadian Space Agency.

a) Letter a) shows the Prince of Wales Icefield located in the southeast of Ellesmere Island. An earlier melt end was observed at higher elevation due to lower air temperatures. At the coast of the Icefield, at lower elevation, the melt end was much later.

b) Around Lake Hazen the melt end was one of the earliest observable. However, Lake Hazen itself showed one of the latest melt ends. The reason for this abnormality is probably the large specific heat capacity of water (Osborne and Ginnings, 1939). The surrounding area of Lake Hazen showed early melt ends, probably because just a thin snow layer was present, which was melted very soon. The early snow-free area was also visible in the optical MODIS images. The region around Lake Hazen was the first snow free area.

c) In the lowlands near Eureka again very early melt ends were observed, similar to Lake Hazens' surroundings, but also very late ones. An explanation could be another snowfall event during the period of investigation. The additional snow could be melted later in the year.

## 5.4. Number of melt days

The highest number of melt days was visible in the lower part of the ice caps, approximately at 1000 m a.s.l. This result is plausible, since at lower elevation the temperatures are higher, but snow/ ice availability is lower. Therefore, the highest number of melt days is somewhere in the middle, where temperatures are quite high and a lot of snow/ice is available (Fig. 62).

In colder years, the maximum was shifted towards lower altitudes, because less melt processes could take place at higher elevation.

South facing slopes showed a higher number of melt days than north facing slopes, indicating higher temperatures.

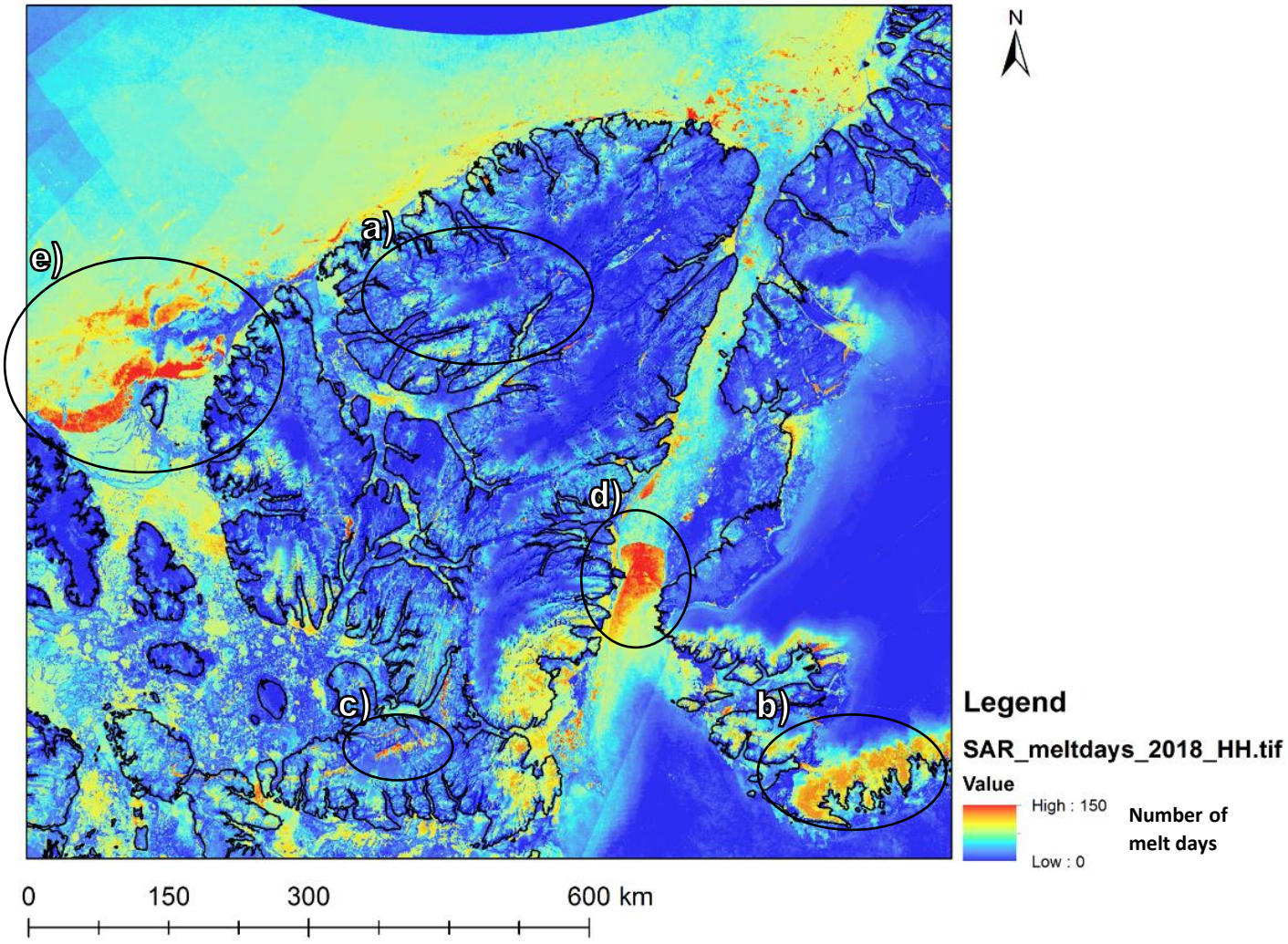


Fig. 62. Number of melt days estimated with SAR HH polarization in the year 2018. Letters a) to e) indicate specific areas being discussed. Contains modified Copernicus Sentinel data (2018). RADARSAT-2 Data and Products ©MacDonald, Dettwiler Associates Ltd. (2018) – All Rights Reserved. RADARSAT is an official trademark of the Canadian Space Agency.

a) In a) the highest number of melt days was observable in the lower part of the ice caps. The lower part of the ice caps is located in warmer temperatures, but still a lot of potential melt material is present. Therefore, melt processes can take place throughout a long time in the year.

b) The here visible southern part of Greenland's west coast showed one of the highest number of melt days. The southern part is probably located in warm temperatures, which was also present in the early melt onset of Nares Strait. Furthermore, this area was never completely ice/snow free when looking at the optical MODIS images, leading to a high melt potential.

c) The red line indicating a high number of melt days is located in a valley with a large river basin. The river could lead to a misclassification of melt days, because the liquid flowing water could be confused with melt processes depending on the reference scene's features. On the other hand, if enough snow/ice is present throughout the melting period, the warm temperatures in the valley could provide a high number of melt days.

d) The high number of melt days in the middle of Nares Strait could be an indication of a transition zone. An area of advancing and retreating sea ice over a longer time could cause a high number of melt days.

e) Moving sea ice could also be an explanation for the high number of melt days here. However, also the sea ice structure could have caused misclassifications (see 5.6.).

As mentioned before, the number of melt days was calculated by adding up the actual days with melt processes. The resulting product can give important information on how much melt water emerged in the areas. However, climatologists often investigate the melt season length and its change, therefore the number of days in which melt can occur (e.g. Stroeve et al., 2014). The melt season length can also be addressed using active microwave data. Fig. 63 presents such a melt season length product derived from SAR HH polarization in 2017. The product was processed by subtracting the melt end product by the melt onset product. Now a clear higher number of "possible" melt days were visible at lower elevation, for example near Eureka. In the case of sea ice, a longer melt season was present in more southern areas, or in the fiords. However, the melt season product is still affected by completely melted snow. Some areas in the lowlands still had a small melt season length, because the melt end was early due to completely melted snow. Therefore, melt season lengths and freeze onsets are still mostly calculated using passive microwave data, because they are less affected by the abundance of snow – but more by temperature (see e.g. (Markus et al., 2009), (Belchansky et al., 2004)). However, sea ice melt duration can also be done using active microwave imagery, since the melt end is not dependent on ice availability over water bodies (e.g. Jeffries et al., 1997). Or melt season length over permanent snow/ice covered features, like glaciers can be addressed as it was for example done by Winsvold et al., 2018.

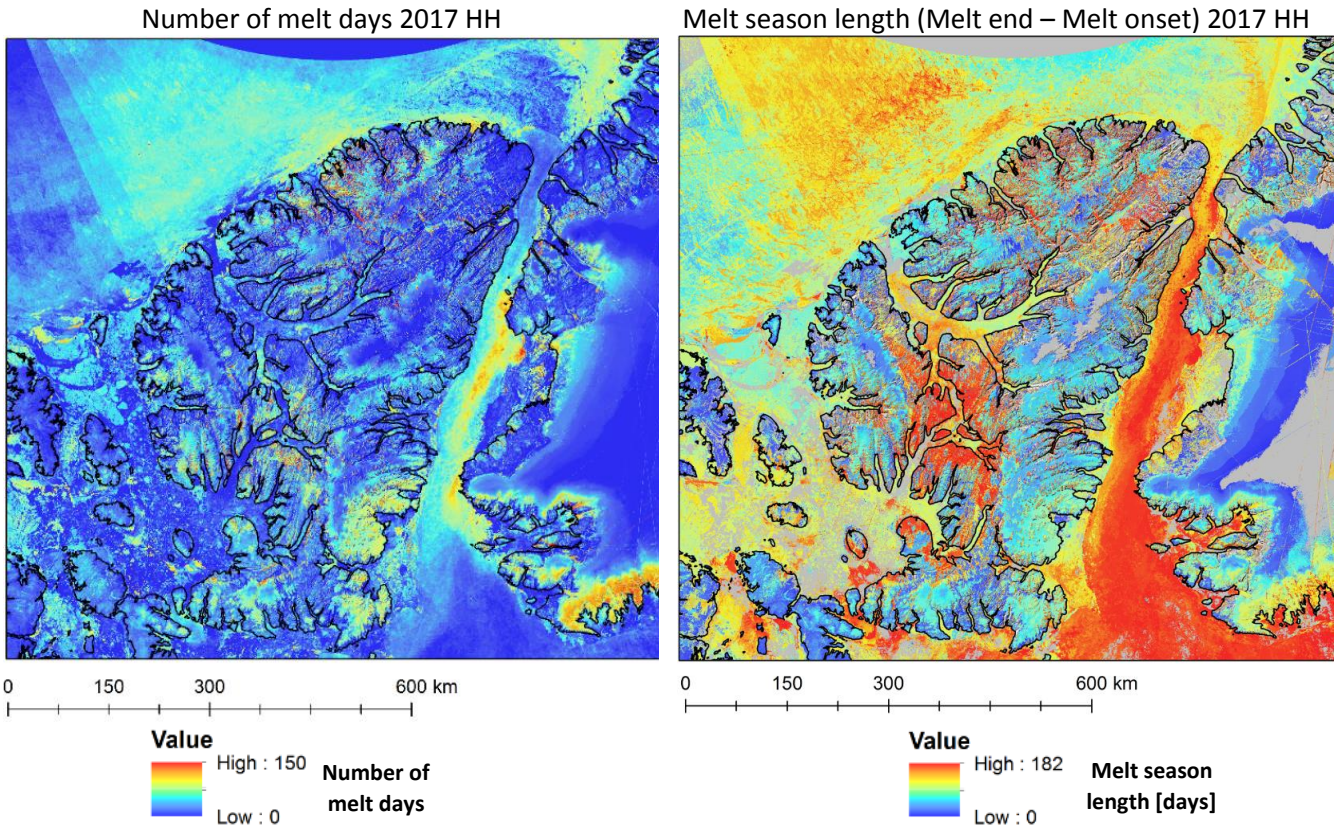


**Fig. 63. Left: Actual number of days with detected melt derived from SAR HH polarization in 2017. Right: Melt season length (melt end date (without sea ice extent mask) subtracted by melt onset date), derived from SAR HH polarization in 2017. Contains modified Copernicus Sentinel data (2018). RADARSAT-2 Data and Products ©MacDonald, Dettwiler Associates Ltd. (2018) – All Rights Reserved. RADARSAT is an official trademark of the Canadian Space Agency.**

## 5.5. Further analysis

### 5.5.1. Comparison to spatial temperature data – MODIS land surface temperature

Compared to the MODIS land surface temperature dataset, the SAR HH onset products showed the most similar result. Therefore, it is suggested that the SAR HH products are superior to the products derived using scatterometer or passive microwave data. The MODIS LST product indicated minimal (1-2 days) earlier melt onsets compared to SAR HH, except in 2016. This difference is rather small and is most probably just representing the uncertainty, also considering that the SAR product was processed with 3-days composites. However, the earlier melt onset in the MODIS LST product might also be caused by a time shift, where the temperature has to be above 0°C for some time until melt processes take place. Another explanation could be that snow may not melt at 0°C depending on solute concentrations within the snow pack (Colliander et al., 2012). Sturdivant et al., 2019 even used a threshold of -0.5°C as a proxy for snowmelt instead of 0°C, but actually this would decrease the temperature derived melt proxy even further.

The later melt onset in the MODIS LST product in the highest elevations could be explained by cloud cover. Cloud cover can only increase the melt onsets, because the actual/earlier melt onset could be missed. Over the ice caps the cloud coverage was quite high throughout the summers. The cloud coverage may also explain the later melt onset in MODIS LST in the year 2016.

### 5.5.2. SAR polarizations

SAR HH showed a much more complete image than SAR HV over sea ice. In the SAR HV product a lot of sea-ice areas showed a missing melt onset. SAR HH generally has higher backscatter values – meaning more received energy compared to the cross-polarized channel. SAR HV is therefore more affected by thermal noise than HH, because of the weaker depolarized power (Park et al., 2018). The influence of thermal noise is especially present over the sea. On water bodies the backscatter is low anyway, because of the absorptive nature of water in the microwave spectrum. Therefore, it is suggested to make use of the SAR HH polarization, rather than of the HV polarization to investigate melt processes of/ over sea ice. Stettner et al., 2018 suggested the use of HV polarization data on land areas, where in their results the VV polarization showed the smallest accuracy. Especially the increased backscatter signal from vegetation, which was also a problem here, had a higher impact in the HH or VV polarizations. Furthermore, the VH polarization may be better suited in finding the transition from volume scattering in dry snow to the surface scattering in wet snow. Nagler et al., 2016 stated that HV polarization can better delineate wet snow from snow free surfaces, especially at low incidence angles (e.g. on fore-slopes). In this study, the HV products generally showed less early melt ends in the lowlands, which could be caused by the worse capability in separating wet from no-snow. Therefore, HV data might be better suited to detect wet snow on land areas, but in our results this could not be ultimately supported without ground-truth data.

### 5.5.3. Spatial resolution

The best spatial resolution was by far observed in the SAR derived products. Passive microwave products had a spatial resolution of 10 km, where even at large scale the coastal areas were mixed with signals from the sea. The ASCAT derived product had more than a 2x better resolution (4.45 km) compared to PM. However, the rough topography of Ellesmere Island could not be sufficiently represented using this resolution. Valleys and nearby hills or mountains were merged together into one pixel. SAR $\gamma_c^0$ composites on the other hand, had an even more than 10 x better spatial resolution compared to ASCAT and a 25 x better compared to PM. With a spatial resolution of 400m it was even possible to delineate the signals from single valleys or glaciers. Therefore, if confronted with a rough terrain study site or narrow channels with sea ice, SAR holds a major advantage and is the candidate of choice (Winebrenner et al., 1994), (Small et al., 2011), (Howell et al., 2018).

### 5.5.4. Composite interval

Shorter $\gamma_c^0$ SAR composite intervals resulted in more onset area found. An explanation could be the snow thickness, where in some areas; especially in the inner-lowlands the snow layer is very thin. The snow depth in spring 2018 at the weather station Eureka was just 13 cm. The reason for just a thin snow layer is most probably due to a very low precipitation rate in the Island's interior. Therefore, shorter composite intervals are better able to detect melt processes when the snow layer is thin and melted away fast.

### 5.5.5. Land cover specific thresholds

As we have seen in fig. 49 there was a decrease in backscatter in the grassland class at the time of rising air temperatures, but it was too small to be detected as melt. Again here, the problem was most probably caused by the too thin snow layer. But the presence of snow was assured for all of Ellesmere Island as indicated by the optical MODIS products. Wagner et al., 2013 stated that rough snow surfaces or rough terrain, thin snow or protruding vegetation could neutralize the backscatter decrease of melt processes. In our study area, we had exactly these conditions of thin snow and rough terrain and probably also rough snow surfaces. Therefore, it became necessary to reduce the threshold from -2 dB to -1 dB, where an almost complete image could be achieved. Furthermore, the images using the new threshold were feasible, because of their similarity to the products derived with a shorter composite interval. The increase in backscatter in the grassland areas after the snow was melted was probably caused by vegetation growth. Higher vegetation increases the surface roughness, leading to more received energy by the sensor (Fig. 64), (Chen et al., 2007).

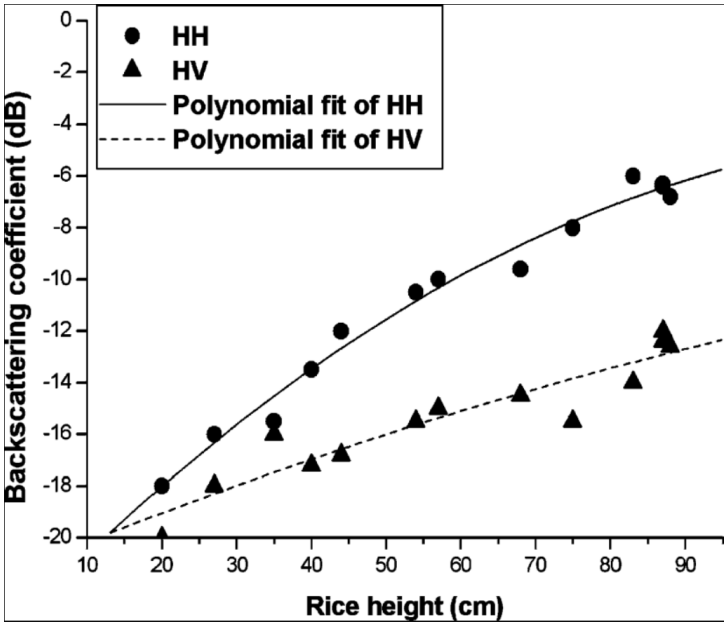


Fig. 64. SAR backscatter coefficient for different heights of rice (Chen et al., 2007).

Fig. 65 illustrates the increasing NDVI with increasing backscatter values.

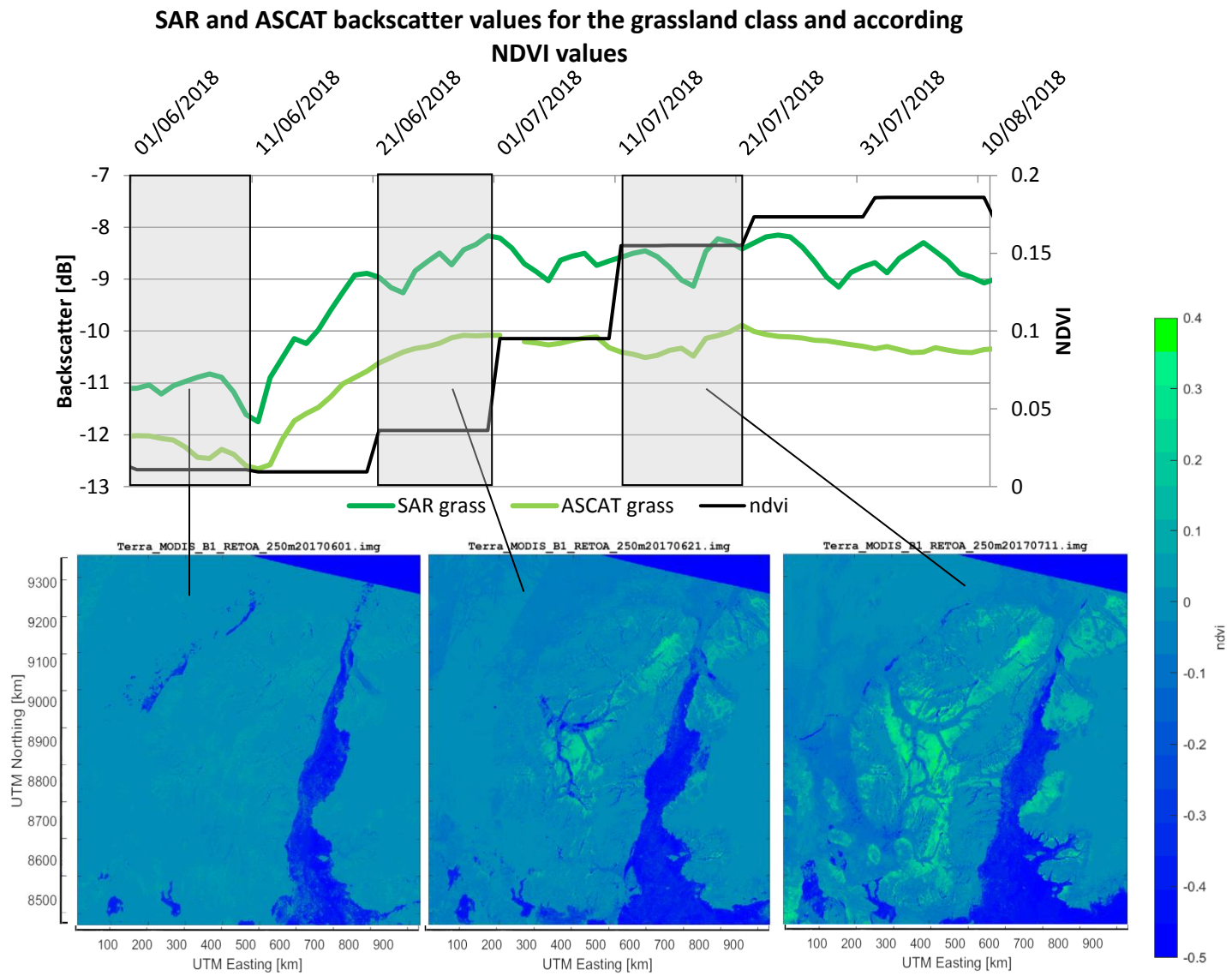


Fig. 65. Top: SAR HH and ASCAT VV mean backscatter values in the grassland class. The black line illustrates the NDVI calculated with optical MODIS composites. Bottom: NDVI images corresponding to the grey boxes above.

## 5.6. Sea ice

The sea ice melt end products had a high resemblance to each other. Melt onset products showed similarities too, for example the early melt onset in Nares Strait, but especially the northwestern sea showed differences. The early melt onset in Nares Strait was also observed in the optical MODIS images (Fig. 66).

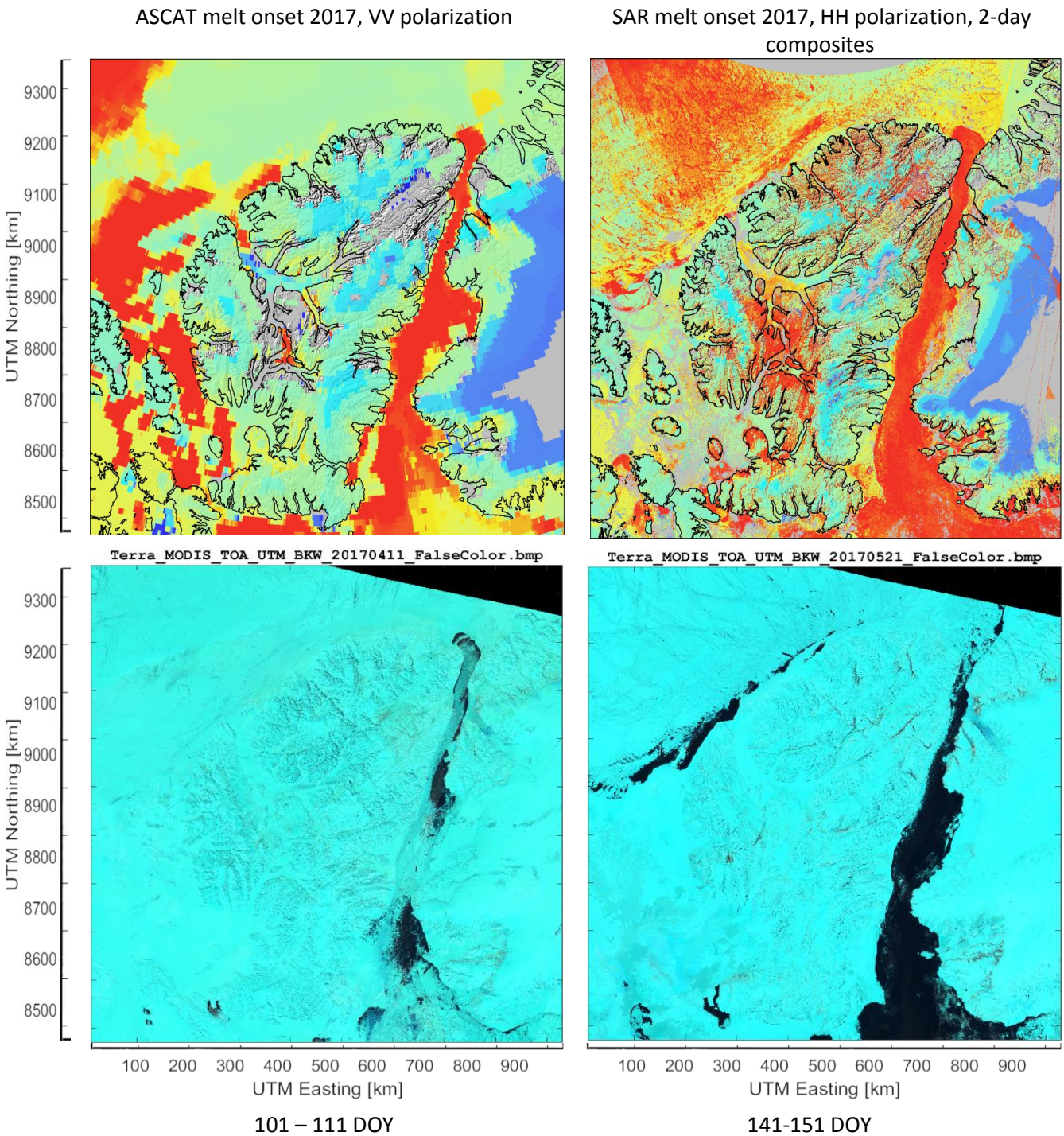


**Fig. 66. Top left: Melt onset 2017 estimated with ASCAT VV polarization. Top right: Melt onset estimated with SAR HH polarization. Bottom left: MODIS false color composite (R= SWIR, G= NIR, B=RED) acquired between the 101th and 111th day of year (DOY). Bottom right: MODIS false color composite (R= SWIR, G= NIR, B=RED) acquired between the 141th and 151th day of year (DOY). Contains modified Copernicus Sentinel data (2018). RADARSAT-2 Data and Products ©MacDonald, Dettwiler Associates Ltd. (2018) – All Rights Reserved. RADARSAT is an official trademark of the Canadian Space Agency.**

The northwestern ocean part showed significant earlier melt onsets for PM than for the SAR result. ASCAT showed earlier melt onsets too but not as strong as PM. An overall later melt onset for SAR was also found by Mahmud et al., 2016; they assumed that the higher spatial resolution of SAR lead to more variability and therefore to later melt onsets. Howell et al., 2018 used a threshold of -8dB for MYI, but this threshold resulted in a large missing onset area here in this study. Therefore, a threshold of -5dB was applied here. The reason for the need of another threshold was probably the choice of the reference scenes' time range. Howell et al., 2018 used the mean of whole April. In our study the reference was calculated as the mean of whole January and February. The decision of the reference scenes' time range obviously had an impact in the thresholds adjustment, because everything else was similar to the study of Howell et al., 2018. Also, the classification of MYI and FYI showed a different result in using another time range of the reference scene; in our study a smaller area was classified as FYI compared to the study of Howell et al., 2018 despite the same threshold of -14.5 dB was used.

The passive microwave sea ice melt product had frequent missing values at the coastal areas. These pixels were probably removed, because they were mixed pixels with including signals from the land areas. This problem decreases with increasing spatial resolution, but we could observe it also in the ASCAT product. In fig. 66, the coastal areas around Nares Strait showed a small stripe of later melt onset than for the inner part of Nares Strait. In the SAR product, such a later onset was not visible. These samples were probably caused by mixed signals. The onset was later, because signals from the land areas were included, which had indeed a later melt onset.

In fig. 60 and 62 e) we saw sea-ice-like structures in the melt products. The structure or topography of sea ice could potentially change the backscatter behavior of SAR, which was also reported by Howell et al., 2018. Such structures include ridges, crevasses or just rough surfaces (Zhou et al., 2019). Same effects are present on the land topography. However, the influence of the land terrain was corrected using a DEM, whereas the sea ice structure cannot be corrected yet due to missing information about the fast-changing ice structure.

## 5.7. Outlook

More available C-band SAR sensors in the future will improve the temporal resolution even further. Shorter composite intervals, like 1 day $\gamma_c^0$ backscatter composites, will be operational with a lower abundance of artifacts. Therefore, the daily temporal resolution can be achieved with an improved spatial resolution compared to previous used PM or scatterometer data. Especially the upcoming RADARSAT Constellation Mission will provide the additional C-band SAR images. The mission consists of three identical SAR satellites with up to 4 times a day revisits of the Arctic (www.asc-csa.gc.ca), (Howell et al., 2018).

The $\gamma_c^0$ backscatter composites used in this study had a spatial resolution of 400m. However, Sentinel-1 and RADARSAT-2 SAR instruments deliver acquisitions with an even better spatial resolution of 5 m to 80 m or 1 m to 100 m depending on the product type (www.earth.esa.int), (www.asc-csa.gc.ca). The spatial resolution is currently limited to 400 m because of the digital elevation model (DEM) used for the terrain correction. A new DEM with a better spatial resolution could therefore improve the spatial resolution further (Small, 2012).

A terrain correction would not be necessary when applying the change detection method. However, to combine sensors with different viewing geometries and passes it becomes essential. Furthermore, melt onset detection could potentially be achieved without using a reference scene in terrain corrected images.

Several suggestions for the choice of the reference scene's time range are present in the literature. Nagler and Rott 2000, suggested a mean of autumn to midwinter. Howell et al., 2018 used the April mean, because Yackel and Barber, 2000 assumed that variations in the dielectric constants, due to temperature changes are small during April. Therefore, the April mean may be better suited for investigating sea ice. Sturdivant et al., 2018 used a 14-day running mean for each date of observation. Nghiem et al., 2001 used a diurnal threshold for scatterometer data, where snow was considered to be actively melting when the afternoon backscatter was at least -1.8 dB smaller than the morning acquisition. Here in this study a compromise was applied, where the mean of January and February was calculated. However, as we have seen, the choice of the reference scenes' time range can cause significant differences. A new method not depending on a reference scene is therefore desired. However, the influence of the local incidence angle on the backscatter value was a problem (Guangjun et al., 2017). With the use of $\gamma_c^0$ composites, this problem can be overcome, since the local incidence angles are corrected using a DEM.

Melt onset is reached when the pixel value is lower than a threshold. Using a single scene threshold is for example frequently used in flood mapping, where everything below a threshold is considered as water bodies (e.g. Manjursee et al., 2012). The thresholds to detect wet snow without a reference scene were iterated until the products became as close as possible to the products created previously with using a reference scene (Tab. 4). The detection of melt processes on FYI also needed an upper threshold, to delineate sea ice from open water surfaces.

Tab. 4. Applied thresholds in dB to detect wet snow without using a reference scene.

| Land cover | HH polarization thresholds [dB] | HV polarization thresholds [dB] |
|---|---|---|
| Land (without grassland) | $\gamma_c^0$ <= **-9** | $\gamma_c^0$ <= **-15** |
| Grassland | $\gamma_c^0$ <= **-13** | $\gamma_c^0$ <= **-20** |
| FYI | **-12** <= $\gamma_c^0$ <= **-14.5** | **-21** <= $\gamma_c^0$ <= **-23** |
| MYI | $\gamma_c^0$ <= **-15** | $\gamma_c^0$<= **-23** |

Less melt onset was detected in high elevations, because these areas showed a relatively high backscatter throughout the whole year. Earlier onsets were found in lowlands when using the method without a reference scene (Fig 67). Without the use of ground truth data, it is not ultimately clear which method presented real conditions more trustworthy, but temperature data indicate that the melt onset in the lowlands is too early using no reference scene. The onset date could be shifted towards a later onset by using a smaller threshold, but that also resulted in a lot more missing onset areas.

Earlier onsets were detected on northwestern sea ice, which now corresponds better to the results found by the PMW algorithm and the results found by Howell et al., 2018. Furthermore, the new method was less affected by the sea ice structure than the one using a reference scene, which could also explain the later onsets. HV polarization SAR data showed no more a higher abundance of missing onset values, as it did with using a reference scene.

The method without using a reference scene is presumably better suited in addressing melt of or on sea ice, but lacks in detecting melt processes on land due to the complex backscatter behavior of different land materials.

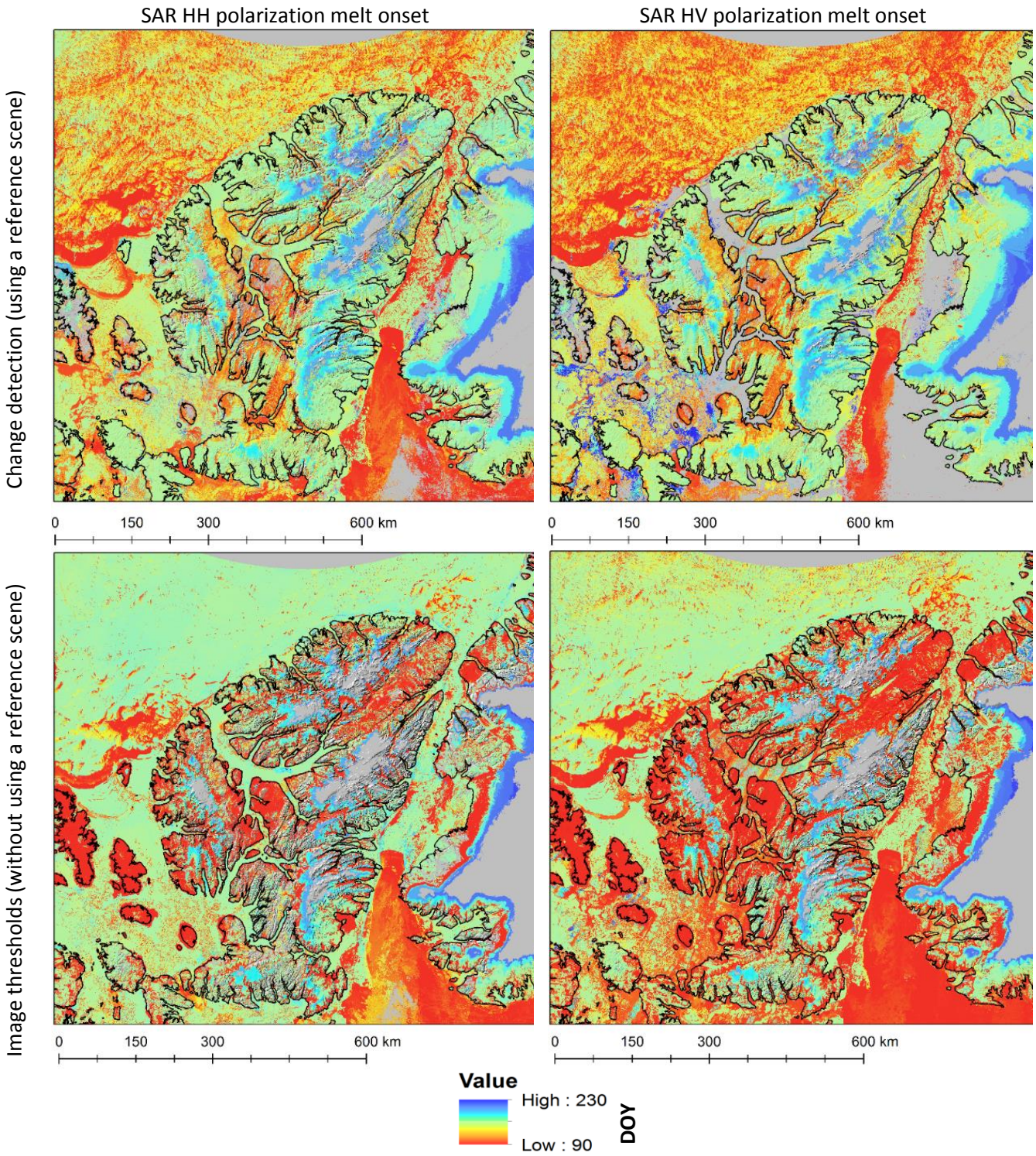


**Fig. 67. Top left: SAR HH polarization melt onset for the year 2018 using 2-day composites and a reference scene. Top right: SAR HV polarization melt onset for the year 2018 using 2-day composites and a reference scene. Bottom left: SAR HH polarization melt onset for the year 2018 using 2-day composites without a reference scene. Bottom right: SAR HV polarization melt onset for the year 2018 using 2-day composites without a reference scene. Contains modified Copernicus Sentinel data (2018). RADARSAT-2 Data and Products ©MacDonald, Dettwiler Associates Ltd. (2018) – All Rights Reserved. RADARSAT is an official trademark of the Canadian Space Agency.**

The number of melt days and the melt end showed a lot of similarities using the methods with and without a reference scene. Nevertheless, there were some differences (Fig. 68):

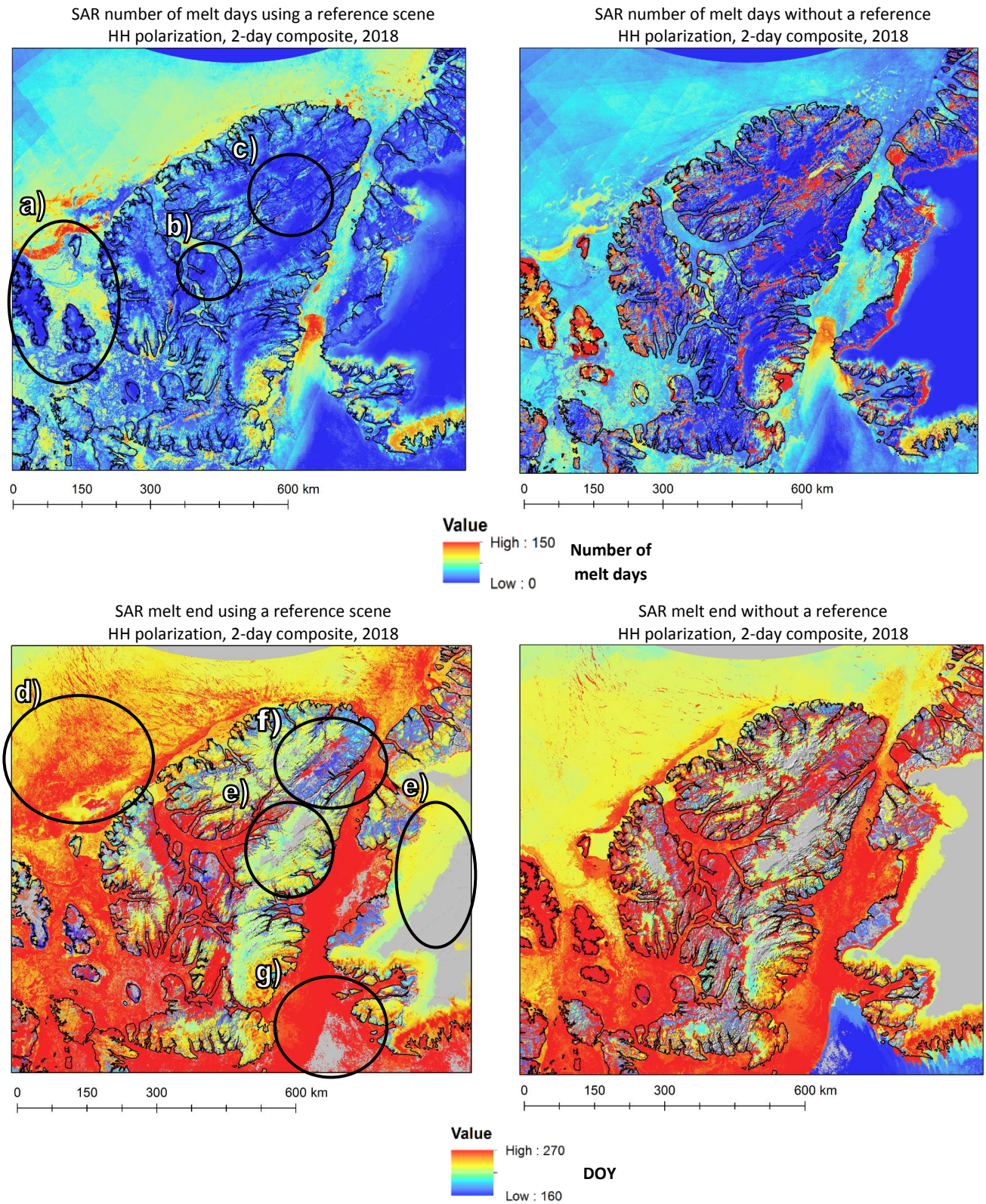


**Fig. 68. Top left: SAR HH polarization number of melt days for the year 2018 using 2-day composites and a reference scene. Top right: SAR HH polarization number of melt days for the year 2018 using 2-day composites without a reference scene. Bottom left: SAR HH polarization melt end for the year 2018 using 2-day composites and a reference scene. Bottom right: SAR HH polarization melt end for the year 2018 using 2-day composites without a reference scene. Contains modified Copernicus Sentinel data (2018). RADARSAT-2 Data and Products ©MacDonald, Dettwiler Associates Ltd. (2018) – All Rights Reserved. RADARSAT is an official trademark of the Canadian Space Agency.**

a) More melt days were observed on the smaller islands in the west of Ellesmere Island.
b) More melt days were observed in the lowlands, especially near Eureka.
c) Glaciers showed a maximum number of melt days when using no reference scene. Probably such a high number of melt days was caused by the low elevation of the glaciers and the availability of ice. But the number of melt days was so large that it is more likely to be a misclassification. Glaciers would probably need another threshold to classify melt processes.
d) Earlier melt end was observed in the northwestern sea and it was less affected by sea ice structures.
e) Less onset/end was found in high elevations.
f) The lowlands near Lake Hazen showed much later melt ends when using no reference scene. A snow-fall event during the melt period could possibly explain such a late melt end, because in the MODIS false color images we saw early melted snow in this area.
g) An early melt end was found in southern Nares Strait without the use of a reference scene, where no melt end was found with using a reference.

To improve the no-reference method maybe other thresholds for other land covers would be needed, for example another threshold for ice caps and maybe one for glaciers. But on land areas this would be a hard task, because so many different materials have different backscatter properties and classifications are not easily done. On water surfaces this task was easier, since only FYI and MYI had to be classified and less different materials are present on water surfaces.

In Fig. 69, the combination of the original change detection method and the new method without a reference scene is shown. For water surfaces, the result from the no-reference scene method was used and for land areas the change detection results. Presumably, this combination is superior to all other results.

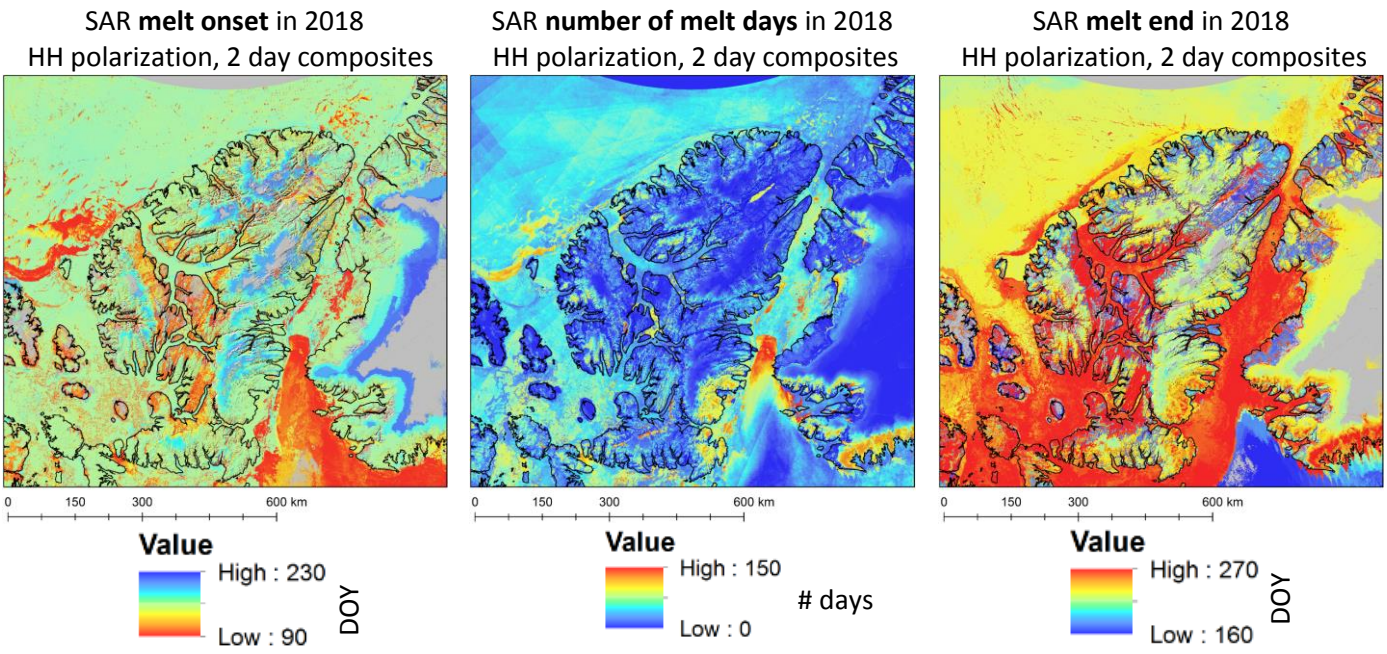


**Fig. 69. Tis image is identical to the front pages' image. From left to right: SAR HH polarization melt onset, number of melt days and melt end for the year 2018. The sea ice area was investigated using the new method without a reference scene. The land area was investigated using the change detection method described in 3.2.2, 3.3 and 3.4. Contains modified Copernicus Sentinel data (2018). RADARSAT-2 Data and Products ©MacDonald, Dettwiler Associates Ltd. (2018) – All Rights Reserved. RADARSAT is an official trademark of the Canadian Space Agency.**

ASCAT data could also be used to detect melt on sea ice without using a reference scene, because for sea ice a terrain correction is not needed. However, other thresholds are needed when using ASCAT data, because the ASCAT VV polarization typically shows smaller backscatter values than SAR HH, which can also be seen in fig. 49.

Another approach to estimate melt onset and end without the use of a reference scene would be an investigation of the backscatter at each sample. At each sample a time series of the backscatter could give information on the timing of melt onset and end, since a strong decrease in backscatter should be observable at melt onset and a corresponding increase at melt end. The increase and decrease could be detected with an edge detection. A similar approach was done by Liu et al., 2006 with the use of PM data.

# 6. Conclusion

SAR $\gamma_c^0$ backscatter composite images have proven their capability in mapping wet snow/ice areas on Arctic land areas as well as of sea ice. Furthermore, melt onset, end and the number of melt days could be estimated. The enhanced spatial resolution made SAR much more robust against mixed pixels and is therefore ideal in rough terrain. However, refreezing onset and the length of melt season is still problematic for some land areas, since the melt end is dependent on snow/ice availability. Therefore, refreezing onset can only be estimated for sea ice or areas with permanent snow/ice cover, like glaciers or ice caps. Furthermore, a smaller threshold for areas with a shallow snow cover is needed especially when using ASCAT or SAR $\gamma_c^0$ images with a composite interval longer than 1 day. Otherwise these areas might be missed for WSIA detection. In this study a threshold of -1 dB was found to be appropriate for this specific study region.

The comparison of the SAR derived WSIA, melt onset, end and number of melt days with the scatterometer and passive microwave products showed a strong correlation, especially between the SAR and scatterometer products. Furthermore, weather data from weather stations and MODIS optical images supported the results from SAR.

The disadvantage of SAR compared to scatterometer and passive microwave instruments can now be overcome almost completely using the concept of $\gamma_c^0$. Multisensor SAR composites can increase the temporal resolution up to the desired 1-day resolution, if enough sensors/images are available in the area of interest. However, the mixture of Sentinel-1A, Sentinel-1B and RADARSAT-2 still caused a significant abundance of artifacts within the composite images, especially at a high temporal resolution.

Nevertheless, the spatial resolution can currently be improved by approximately 10x compared to ASCAT and 25x to PM respectively. Melt detection using SAR was spatially much more precise than using climate reanalysis data. Moreover, the estimated melt variables, like melt onset, are empirically measured rather than modeled. Snow or ice melt is not only dependent on the surface temperature, its dependent on the whole energy balance. The energy balance also includes winds for example, which can strongly affect the timing of melt onset (van Den Broeke et al., 2010).

Crevasses in flowing ice streams on sea ice can lead to misclassifications based on the differences in backscatter (Zhou et al., 2019). Information of the sea ice structure would be necessary in future applications to improve the results.

SAR HH polarization data have been proven to be superior to HV data in detecting WSIA of/on sea ice when using a reference scene. SAR HV polarization data often missed more areas when estimating melt onset, end or the number of melt days, due to the higher influence of thermal noise in the cross polarized channel (Park et al., 2018). When using no reference scene to detect melt processes, the problem was not observed. Also for land areas HH is more similar to MODIS, at least for the melt onset product, but the HV polarization data seemed to be less affected by noise on land areas. A higher accuracy of the cross-polarized channel was also reported in the literature by Nagler et al., 2016 and Stettner et al., 2018. However, in their studies no $\gamma_c^o$ backscatter images were used. Without further investigations and without ground truth data, it was not possible to ultimately prefer a specific polarization in $\gamma_c^o$ composite images on land areas.

The upcoming RADARSAT Constellation Mission will even further improve the investigation of melt processes in the Arctic. More C-band SAR sensors will be available resulting in a high temporal resolution. Therefore, SAR instruments could become the candidates of choice in investigating melt processes in the Arctic (Howell et al., 2018).

In summary, the research questions could be answered as follows:

- How well can we detect melt onset and end using $\gamma_c^o$ backscatter SAR scenes compared to the often used scatterometer and passive microwave instruments?
  $\gamma_c^o$ backscatter SAR scenes have proven their capability in detecting wet snow and determining melt onset and the number of melt days. The comparison to ASCAT and PM data, as well as weather data showed a strong correlation.

    - Do the SAR HH and HV polarizations make any difference and if yes, how?
      SAR HH polarization data were better suited to address snow or ice melt when using a change detection method with the use of a reference scene. Especially sea ice melt or snow on sea ice was better addressed with HH data. HV data often missed to estimate melt processes in significant more areas. Using the no-reference method, this problem was not observed and therefore, HV data might be superior, because it might be less affected by noise on land areas.

- How plausible are the results when we compare them to auxiliary data, such as temperature data?
  The correlation of microwave WSIA showed a strong correlation with temperature and snow depth data. SAR showed the strongest correlation to the temperature measurements (r = 0.74) and the melt onset estimates were closest to MODIS LST melt onsets.

- What advantages and disadvantages does each instrument offer considering the task of detecting wet snow and melt onset and end?
  A summary of the advantages and disadvantages can be seen in tab. 5.

Tab. 5. Advantages and disadvantages each instrument type offers concerning the detection of melt processes.

| Instrument type | Advantages | Disadvantages |
|---|---|---|
| SAR ($\gamma_c^o$ backscatter composites) | - **Best spatial resolution**<br>- Almost a daily temporal resolution<br>- Melt end is **dependent on snow availability**<br>- Number of melt days is an estimate of the **actual number of melt days** and not the possible number of melt days | - **Length of melt season** can only be addressed for permanent snow/ice covered areas or sea ice<br>- A shorter composite interval leads to **more artifacts**<br>- Special land areas might need an **adjusted threshold** – for example areas with thin snow cover or FYI<br>- **Computation** is harder than for ASCAT (need also the generation of $\gamma_c^o$ backscatter composites)<br>- The choice of the **reference scene time range** influences the result |
| Scatterometer | - Better spatial resolution than PM<br>- **Daily temporal resolution**<br>- Melt end is **dependent on snow availability**<br>- Number of melt days is an estimate of the **actual number of melt days** and not the possible number of melt days | - Worse **spatial resolution** than SAR<br>- **Length of melt season** can only be addressed for permanent snow/ice covered areas or sea ice<br>- Special land areas might need an **adjusted threshold** – for example areas with thin snow cover<br>- The choice of the **reference scene time range** influences the result |
| Passive Microwave | - **Daily temporal resolution**<br>- **Less affected by no-snow areas**<br>- **Length of melt season** can be better estimated<br>- **No adjusted threshold** for different land classes needed<br>- **Long-term** measurements available | - Worst **spatial resolution;** the low spatial resolution results in **mixed pixels**<br>- Melt onset/ end **not necessarily dependent on snow availability**<br>- The choice of the **reference scene time range** influences the result |

As an addition, a new method was shown to monitor melt processes using $\gamma_c^o$ backscatter SAR composites without using a reference scene. The presented method was capable to detect sea ice melt and snowmelt on sea ice with an even stronger similarity to the PMW algorithm results (Markus et al., 2009) and the results found by Howell et al., 2018 than the method including a reference scene. The results on the land area however, were less plausible due to more complex backscatter behaviors of different land materials. Nevertheless, future algorithms to detect melt processes should further investigate the capability of $\gamma_c^o$ backscatter SAR composites and no-reference methods, because the choice of the reference scene's time range can influence the result strongly.

# List of figures

# List of tables

## List of abbreviations

| | |
|---|---|
| **AMSR2** | Advanced Microwave Scanning Radiometer 2 |
| **AMSR-E** | Advanced Microwave Scanning Radiometer for the Earth Observing System |
| **ASCAT** | Advanced Scatterometer |
| **CCRS** | Canadian Centre for Remote Sensing |
| **DAV** | Diurnal Amplitude Variation |
| **DEM** | Digital Elevation Model |
| **ECMWF** | European Centre for Medium-Range Weather Forecasts |
| **ERA5** | ECMWF Reanalysis 5th Generation |
| **ESA** | European Space Agency |
| **FYI** | First Year Ice |
| **HH** | Horizontally polarized sent, Horizontally polarized received |
| **HV** | Horizontally polarized sent, Vertically polarized received |
| **IW** | Interferometric Wide |
| **LRW** | Local Resolution Weighting |
| **LST** | Land Surface Temperature |
| **MODIS** | Moderate Resolution Imaging Spectro-Radiometer |
| **MWRI** | MicroWave Radiation Imager |
| **MYI** | Multi Year Ice |
| **NASA** | National Aeronautics and Space Administration |
| **NDSI** | Normalized Difference Snow Index |
| **NDVI** | Normalized Difference Vegetation Index |
| **PM** | Passive Microwave |
| **PMW** | Passive MicroWave algorithm |
| **QuikSCAT** | Quick Scatterometer |
| **RS2** | RADARSAT-2 |
| **RSL** | Remote Sensing Laboratories |
| **RTC** | Radiometrically Terrain Corrected |
| **S1** | Sentinel-1 |
| **SAR** | Synthetic Aperture Radar |
| **SD** | Snow Depth |
| **SE** | Snow Extent |
| **SSM/I** | Special Sensor Microwave/ Image |
| **SSMR** | Scanning Multichannel Microwave Radiometer |
| **SWIR** | Short-wave Infrared |
| **Tb** | Brightness Temperature |
| **TOA** | Top Of Atmosphere |
| **Ts** | physical near Surface Temperature |
| **UTM** | Universal Transverse Mercator |
| **VV** | Vertically polarized sent, Vertically polarized received |
| **WSIA** | Wet Snow or Ice Area |

## References:


- www.cruisemapper.com/ports/ellesmere-island-port-2578, visited on 26.09.2018
- www.espo.nasa.gov/attrex/image/Sea_ice_along_the_coast_of_Ellesmere_Island, visited on 26.09.2018
- www.flickr.com/photos/8905239@N05/6209581637, visited on 25.09.2018
- www.thecanadianencyclopedia.ca/en/article/ellesmere-island, visited on 25.09.2018
- www.climate.nasa.gov/news/2641/keeping-an-eye-on-earths-energy-budget/, visited on 01.10.2018
- www.climatecentral.org/gallery/graphics/spring-snow-cover, visited on 01.10.2018
- www.earth.esa.int/web/guest/missions/esa-operational-eo-missions/sentinel-1, visited on 01.10.2018
- www.earth.google.com, visited on 13.02.2019
- www.lpdaac.usgs.gov/dataset_discovery/modis/modis_products_table/mcd12c1, visited on 13.02.2019
- www.modis.gsfc.nasa.gov/about/, visited on 13.02.2019
- www.remss.com/missions/amsr/, visited on 13.02.2019
- www.wmo-sat.info/oscar/satellites/view/116, visited on 13.02.2019
- www.asc-csa.gc.ca/eng/satellites/radarsat/faq.asp, visited on 02.04.2019

- **Akyürek** Z. and **Sorman** A.Ü. (2002): Monitoring snow-covered areas using NOAA AVHRR data in the eastern part of Turkey. *Hydrological Sciences, 47, 243–252*
- **Amlien** J. (2008): Remote Sensing of Snow with Passive Microwave Radiometers. A Review of Current Algorithms. *Report No. 1019 (Oslo: Norsk Regnesentral)*
- **Bales** R.C., Molotch N.P., Painter T.H., Dettinger M.D., Rice R. and Dozier J. (2006): Mountain hydrology of the western United States. *Water resources research, 42*
- **Barber** D.G. (2005): Microwave remote sensing, sea ice and arctic climate. *Physics in Canada, 61 (2005), pp. 105-111*
- **Barnett** T.P., Adam J.C., and Lettenmaier D.P. (2005): Potential impacts of a warming climate on water availability in snow-dominated regions. *Nature, 438, 7066, 303–309*
- **Belchansky**, G.I., Douglas D.C., Mordvintsev I.N. and Platonov N.G. (2004): Estimating the time of melt onset and freeze onset over arctic sea-ice area using active and passive microwave data. *Remote Sensing of Environment, 92, 21-39*
- **Bhattacharya** A. and **Mukherjee** K. (2017): Review on InSAR based displacement monitoring of Indian Himalayas: issues, challenges and possible advanced alternatives. *Geocarto International, 32:3, 298-321*

- **Bliss** A.C. and **Anderson** M.R. (2014): Snowmelt onset over Arctic sea ice from passive microwave satellite data: 1979-2012. *The Cryosphere, 8, 2089-2100*
- **Brown** R.D. (2000): Northern Hemisphere snow cover variability and change, 1915–97. *Journal of Climate, 13, 2339–2355.*
- **Brown** R.D. and **Robinson** D.A. (2011): Northern Hemisphere spring snow cover variability and change over 1922-2010 including an assessment of uncertainty. *Cryosphere, 5, 219-229*
- **Chang** A.T.C. and **Rango** A. (2000): Algorithm Theoretical Basis Document (ATBD) for the AMSR-E Snow Water Equivalent Algorithm. *Version 3.1, 1–49 (Greenbelt, MD: NASA Goddard Space Flight Center)*
- **Chang** A.T.C., Foster J. and Hall D.K. (1987): NIMBUS-7 SMMR derived global snow cover parameters. *Annals of Glaciology, 9, pp. 39–44*
- **Chen** J., Lin H. and Pei Z. (2007): Application of ENVISAT ASAR Data in Mapping Rice Crop Growth in Southern China. *IEEE Geoscience and Remote Sensing Letters, 4:3*
- **Clifford** D. (2010): Global estimates of snow water equivalent from passive microwave instruments: history, challenges and future developments. *International Journal of Remote Sensing, 31, 3707–3726*
- **Colbeck** S., Akitaya E., Armstrong R., Gubler H., Lafeuille J., Lied K., McClung D. and Morris E. (2015): The international classification for seasonal snow on the ground. *International Association of Scientific Hydrology, 253, 6557 743–749*
- **Colbeck** SC. (1979): Grain clusters in wet snow. *J. Colloid Interface Sci.* 72, 371–84
- **Colliander** A., McDonald K.C., Zimmermann R., Schroeder R., Kimball J.S. and Njoku E.G. (2012): Application of QuikSCAT Backscatter to SMAP Validation Planning: Freeze/Thaw State over ALECTRA Sites in Alaska from 2000 to 2007. *Geoscience and Remote Sensing, IEEE Transactions On 50(2): 461-468*.
- **Dietz** A.J., Kuenzer C., Gessner U. and Dech S. (2012): Remote sensing of snow – a review of available methods. *International Journal of Remote Sensing, 33:13, 4094-4134*
- **Dozier** J. (1989): Spectral signature of Alpine snow cover from the Landsat Thematic Mapper. *Remote Sensing of Environment, 28, 9–22*
- **Dozier** J. and **Painter** T.H. (2004): Multispectral and hyperspectral remote sensing of alpine snow properties. *Annu. Rev. Earth Planet. Sci., 32, 465-94*
- **Drobot** S.D. and **Anderson** M.R. (2001): An improved method for determining snowmelt onset dates over Arctic sea ice using Scanning Multichannel Microwave Radiometer and Special Sensor Microwave/Imager data. *Journal of Geophysical Research, 106, 24033-24049*
- **Early** D.S. and **Long** D.G. (2001): Image reconstruction and enhanced resolution imaging from irregular samples. *IEEE Transactions on Geoscience and Remote Sensing, 39 (2), 291-302*
- **Environment and Climate Change Canada** (2018): Canadian Environmental Sustainability Indicators: Snow cover. Consulted on Month day, year. *Available at: www.canada.ca/en/environment-climate-change/services/environmental-indicators/snow-cover.html*
- **Foster** J., Hall D., Chang A., Rango A., Wergin W. and Erbe E. (1999): Effects of snow crystal shape on the scattering of passive microwave radiation. *IEEE Transactions on Geoscience and Remote Sensing, 37, 1165–1168.*
- **Foster** J., Liston G., Koster R., Essery R., Behr H., Dumenil L., Verseghy D., Thompson S., Pollard D. and Cohen J. (1996): Snow cover and snow mass intercomparisons of general circulation models and remotely sensed datasets. *Journal of Climate, 9, 409–426*

- **Foster** J., Sun C., Walker J.P., Kelly R., Chang A., Dong J. and Powell H. (2005): Quantifying the uncertainty in passive microwave snow water equivalent observations. *Remote Sensing of Environment, 94, 187–203*
- **Foster** J.L., Hall D.K., Eylander J.B., Riggs G.A., Nghiem S.V., Tedesco M., Kim E., Montesano P.M., Kelly R.E.J., Casey K.A. and Choudhuri B. (2011): A blended global snow product using VIS, passive microwave and scatterometer satellite data. *International Journal of Remote Sensing, 32, 1371–1395.*
- **Fyfe** J.C., von Salzen K., Gillet N.P., Aurora V.K., Flato G.F. and McConnell J.R. (2013): One hundred years of Arctic surface temperature variation due to anthropogenic influence. *Scientific Reports, 3(1), 2645*
- **GDAL/OGR contributors** (2018): GDAL/OGR Geospatial Data Abstraction Software Library. *Open source Geospatial Foundation. URL http://gdal.org*
- **Green** R.O., Dozier J., Roberts D.A. and Painter T.H. (2002): Spectral snow reflectance models for grain size and liquid water fraction in melting snow for the solar reflected spectrum. *Ann. Glaciol.* 34, 71–73
- **Guangjun** H., Feng X., Xiao P., Xia Z., Wang Z., Chen H., Li H. and Guo J. (2017): Dry and wet snow cover mapping in mountain areas using SAR and optical remote sensing data. *IEEE journal of selected topics in applied earth observations and remote sensing, 10, 6*
- **Hall** D.K. and **Martinec** J. (1985): Remote Sensing of Ice and Snow *(New York: Chapman & Hall)*
- **Hall** D.K. and **Riggs** G.A. (2007): Accuracy assessment of the MODIS snow-cover products. *Hydrological Processes, 21, 1534–1547*
- **Hall** D.K., Riggs G.A. and Salomonson V.V. (1995): Development of methods for mapping global snow cover using moderate resolution imaging spectroradiometer data. *Remote Sensing of Environment, 54, 127–140*
- **Hall** D.K., Riggs G.A., Foster J. and Kumar S.V. (2010): Development and evaluation of a cloud-gap-filled MODIS daily snow-cover product. *Remote Sensing of Environment, 114, 496–503*
- **Hall** D.K., Riggs G.A., Salomonson V.V., Digirolamo N.E. and Bayr K.J. (2002): MODIS snow-cover products. *Remote Sensing of Environment, 83, 181–194.*
- **Howell** S.E.L., Small D. and Brady M. (2018): Estimating melt onset over Arctic sea ice from hybrid Sentinel-1 and RADARSAT-2 backscatter. *Accepted in: Remote Sensing of Environment, 2019*
- **Howell** S.E.L., Tivy A., Yackel J.J. and Scharien R.K. (2006): Application of a SeaWinds/QuikSCAT sea ice melt algorithm for assessing melt dynamics in the Canadian Arctic Archipelago. *Journal of Geophysical Research, 111(C7), C07025*
- **Hyvärinen** O., Eerola K., Siljamo N. and Koskinen J. (2009): Comparison of snow cover from satellite and numerical weather prediction models in the Northern Hemisphere and Northern Europe. *Journal of Applied Meteorology and Climatology, 48, 1199–1216*
- **Jain** S.K., Goswami A. and Saraf A.K. (2008): Accuracy assessment of MODIS, NOAA and IRS data in snow cover mapping under Himalayan conditions. *International Journal of Remote Sensing, 29, 5863–5878.*
- **Jeffries** M.O., Schwartz K. and Li S. (1997): Arctic summer sea-ice SAR signatures, melt-season characteristics, and melt-pond fractions. *Polar Record 33(185): 101-112*
- **Kelly** R., Chang A., Tsang L. and Foster J. (2003): A prototype AMSR-E global snow area and snow depth algorithm. *IEEE Transactions on Geoscience and Remote Sensing, 41, 230–242.*

- **Klein** A.G. and Stroeve J. (2002): Development and validation of a snow albedo algorithm for the MODIS instrument. *Annals of Glaciology, 34, 45–52*
- **Klein** A.G., Hall D.K. and Nolin A.W. (2000): Development of a prototype snow albedo algorithm for the NASA MODIS instrument. *In 57th Eastern Snow Conference, 17–19 May 2000, Sysacuse, NY, USA, 143–158*
- **König** M., Winther J. and Isaksson E. (2001): Measuring snow and glacier ice properties from satellite. *Reviews of Geophysics, 39, 1–27.*
- **Koskinen** J., Metsämäaki S., Grandell J., Jänne S., and Matikainen L. (1999): Snow monitoring using radar and optical satellite data. *Remote Sens. Environ., 69, 1, 16–29*
- **Koskinen** J.T., Pulliainen J.T. and Hallikainen M.T. (1997): The use of ERS-1 SAR Data in Snow Melt Monitoring. *Transactions on geosciences and remote sensing, 35*
- **Kumar** V. and **Venkataraman** G. (2011): SAR interferometric coherence analysis for snow cover mapping in the western Himalayan region. *Int. J. Digit. Earth, 4, 1, 78–90*
- **Kwok** R. (2004): Annual cycles of multiyear sea ice coverage of the Arctic Ocean: 1999-2003. *Journal of Geophysical Research, 109(C11), C11004*
- **Lemke** P., Ren J., Alley R.B., Allison I., Carrasco J., Flato G., Fujii Y., Kaser G., Mote P., Thomas R.H. and Zang, T. (2007): Observations: changes in Snow, ice and frozen ground. In *Climate Change 2007: The Physical Science Basis. Contribution of Working Group I to the Fourth Assessment Report of the Intergovernmental Panel on Climate Change*, S. Solomon, D. Qin, M. Manning, Z. Chen, M. Marquis, K.B. Averyt, M. Tignor and H.L. Miller (Eds.), pp. 337–384, Cambridge and New York: Cambridge University Press
- **Lesins** G., Duck T.J. and Drummond J. R. (2010): Climate trends at Eureka in the Canadian high Arctic. *Atmos. Ocean, 48, 2, 59-80*
- **Ling** F. and **Zhang** T. (2003): Impact of the timing and duration of seasonal snow cover on the active layer and permafrost in the Alaskan Arctic. *Permafr. Periglac. Process. 14, 141-150*
- **Liu** H., Wang L. and Jezek K.C. (2006): Spatiotemporal variations of snowmelt in Antarctica derived from satellite scanning multichannel microwave radiometer and Special Sensor Microwave Imager data (1978-2004). *Journal of geophysical research, 111*
- **Lucas** R.M. and **Harrison** A.R. (1990): Snow observation by satellite: a review. *Remote Sensing Reviews, 4, 285-348*
- **Mahmud** M.S., Howell S.E.L., Geldsetzer T. and Yackel J. (2016): Detection of melt onset over the northern Canadian Arctic Archipelago Sea ice from RADARSAT, 1997-2014. *Remote sensing of Environment, 178, 59-69, 56(11), 6686-6698*
- **Manjusree** P., Kumar P., Bhatt C. M., Rao G. S. and Bhanumurthy V. (2012): Optimization of Threshold Ranges for Rapid Flood Inundation Mapping by Evaluating Backscatter Profiles of High Incidence Angle SAR Images. *Disaster Risk Sci., 3(2): 113-122*
- **Markus** T., Stroeve J. C. and Miller J. (2009): Recent changes in Arctic sea ice melt onset, freezup, and melt season length. *Journal of Geophysical Research, 114, C12024*
- **Mätzler** C. and **Schanda** E. (1984): Snow mapping with active microwave sensors. *Remote Sensing, 5, 1521-1523*

- **Mätzler** C., Schanda E. and Good W. (1982): Towards the definition of optimum sensor specifications for microwave remote-sensing of snow. *IEEE Transactions on Geoscience and Remote Sensing 20(1): 57-66.*
- **Maxwell** J.B. (1981): Climatic regions of the Canadian Arctic islands. Arctic, 34, 3, 225-240
- **McCutchan** M. H. and **Fox** D.G. (1986): Effect of Elevation and Aspect on Wind, Temperature and Humidity. *Journal of Climate and Applied Meteorology. 25. 1996-2013*
- **Meier**, E. (2013): Einführung in die Radar-Fernerkundung. Geographisches Institut der Universität Zürich-Irchel.
- **Miller** S.D. and **Lee** T.F. (2005): Satellite-based imagery techniques for daytime cloud/snow delineation from MODIS. *Journal of Applied Meteorology, 44, 987–997*
- **Mortin** J., Howell S.E.L., Wang L., Derksen C., Svensson G., Graversen R.G. and Schroder T.M. (2014): Extending the QuikSCAT record of seasonal melt-freeze transitions over Arctic sea ice using ASCAT. *Remote Sensing of Environment, 141, 214-230*
- **Mortin** J., Schroder T.M., Hansen A.W., Holt B. and McDonald K.C. (2012): Mapping of seasonal freeze-thaw transitions across the pan-arctic land and sea ice domains with satellite radar. *Journal of Geophysical Research, 117(C8), C08004*
- **Mote** T.L. and **Anderson** M.R. (1995): Variations in snow pack melt on the Greenland ice sheet based on passive-microwave measurements. *J. Glaciol., 41 (37). 51-60*
- **Nagler** T. (1996): Methods and analysis of SAR data from ERS-1 and X-SAR for snow and glacier applications. *Ph.D. dissertation, Inst. Meteorol. Geophys., Univ. Innsbruck, Innsbruck, Austria*
- **Nagler** T. and **Rott** H. (2000): Retrieval of wet snow by means of multitemporal SAR data. *IEEE Trans. Geosci. Remote Sens., 38, 2, 754–765*
- **Nagler** T., Rott H., Ripper E., Bippus G. and Hetzenecker M. (2016): Advancements for Snowmelt Monitoring by Means of Sentinel-1 SAR. *Remote Sens., 8, 348*
- **Nghiem** S.V. and **Tsai** W.Y. (2001): Global snow cover monitoring with spaceborne Ku-band scatterometer. *IEEE Transactions on Geoscience and Remote Sensing, 39, 2118–2134*
- **Nghiem** S.V., Steffen K., Kwok R. and Tsai W.Y. (2001): Detection of snow melt regions on the Greenland ice sheet using diurnal backscatter change. *Journal of Glaciology, 47, 539–547*
- **Nghiem** S.V., Steffen K., Neumann G. and Huff R. (2005): Mapping of ice layer extent and snow accumulation in the percolation zone of the Greenland ice sheet. *Journal of Geophysical Research, 110, 1–13.*
- **Osborne** S. and **Ginnings** B. (1939): Handbook of Chemistry and Physics. *53rd ed., Cleveland, Ohio, D128 (1972-1973)*
- **Painter** T.H., Rittger K., McKenzie C., Slaughter P., Davis R.E. and Dozier J. (2009): Retrieval of subpixel snow covered area, grain size, and albedo from MODIS. *Remote Sensing of Environment, 113, 868–879*
- **Parajka** J., Pepe M., Rampini A., Rossi S. and Blöschl G. (2010): A regional snow line method for estimating snow cover from MODIS during cloud cover. *Journal of Hydrology, 381, pp. 203-212*
- **Park** J.W., Korosov A.A., Babiker M., Sandven S. and Won J.S. (2018): Efficient Thermal Noise Removal for Sentinel-1 TOPSAR Cross-Polarization Channel. *IEEE Transactions on Geoscience and Remote Sensing, 56(3):1555-1565*

- **Park** S.E., Yamaguchi Y., and Singh G. (2014): Polarimetric SAR response of snow-covered area observed by multi-temporal ALOS PALSAR fully polarimetric mode. *IEEE Trans. Geosci. Remote Sens., 52, 1, 329–340*
- **Peng** S., Piao S., Ciais P. and Fang J. (2010): Change in winter snow depth and its impacts on vegetation in China. *Global Change Biology, 16, 3004–3013*
- **Pepe** M., Brivio P.A., Rampini A., Rota Nodari F. and Boschetti M. (2005): Snow cover monitoring in Alpine regions using ENVISAT optical data. *International Journal of Remote Sensing, 26, 4661–4667*
- **Perovich** D. K., Nghiem S.V., Markus T. and Schweiger A. (2007): Seasonal evolution and interannual variability of the local solar energy absorbed by the Arctic sea ice-ocean system. *J. Geophysical Research Letters, 112, C03005*
- **Ramage** J.M. and **Isacks** B.L. (2002): Determination of melt onset and refreeze timing on southeast Alaskan icefields using SSM/I diurnal amplitude variations. *Annals of Glaciology, 34, 391–398*
- **Robinson** D., Kunzi K., Kukla G., and Rott H. (1984): Comparative utility of microwave and shortwave satellite data for all-weather charting of snowcover. *Nature, 312, 5993, 434–435*
- **Rodell** M. and **Houser** P.R. (2004): Updating a land surface model with MODIS-derived snow cover. *Journal of Hydrometeorology, 5, 1064–1075*
- **Rott** H. and **Nagler** T. (1995): Intercomparison of snow retrieval algorithms by means of spaceborne microwave radiometry. *Passive Microwave Remote Sensing of Land- Atmosphere Interactions, 227-243*
- **Schweiger** A.J. (2004): Changes in Seasonal Cloud Cover over the Arctic Seas from Satellite and Surface Observations. *Geophysical Research Letters 31 (12)*
- **Shi** J. and **Dozier** J. (1995): Inferring Snow Wetness Using C-Band Data from SIR-C's Polarimetric Synthetic Aperture Radar. *IEEE transactions on geosciences and remote sensing, 33*
- **Shi** J.C. and **Dozier** J. (1997): Mapping seasonal snow with SIR-C/X-SAR in mountainous areas. *Remote Sens. Environ., 59, 2, 294–307*
- **Shi** J.C., Dozier J., and Rott H. (1994): Snow mapping in alpine regions with synthetic aperture radar. *IEEE Trans. Geosci. Remote Sens., 32, 1, 152–158*
- **Shi** J.C., Hensleya S., and Dozier J. (1997): Mapping snow cover with repeat pass synthetic aperture radar. *IEEE Int. Geosci. Remote Sens. Symp., 1997, 2, 628–630.*
- **Small** D. (2011): Flattening Gamma: Radiometric Terrain Correction for SAR Imagery. *IEEE transactions on Geoscience and Remote Sensing, 49*
- **Small** D., Zuberbühler L., Schubert A. and Meier E. (2011): Terrain-flattened gamma nought Radarsat-2 backscatter. *Can. J. Remote Sensing, 37, 5, 493-499*
- **Small**, D. (2012): SAR backscatter multitemporal compositing via local resolution weighting. *IEEE International Geoscience and Remote Sensing Symposium IGARSS, Munich, Germany, 4521-4524*
- **Stettner** S., Lantuit H., Heim B., Eppler J., Roth A., Bartsch A. and Rabus B. (2018): TerraSAR-X Time Series Fill a Gap in Spaceborne Snowmelt Monitoring of Small Arctic Catchments – A Case Study on Qikiqtaruk (Herschel Island), Canada. *Remote Sens., 10, 1155*
- **Stiles** W.H. and **Ulaby** F.T. (1980): The active and passive microwave response to snow parameters .1. Wetness. *Journal of Geophysical Research-Oceans and Atmospheres 85(NC2): 1037-1044.*
- **Stroeve** J.C., Markus T., Boisvert L., Miller J., and Barrett A. (2014): Changes in Arctic melt season and implications for sea ice loss. *Geophys. Res. Lett., 41, 1216–1225*

- **Sturdivant** E.J., Frey K.E. and Urban F.E. (2019): Snowmelt detection from QuikSCAT and ASCAT satellite radar scatterometer data across the Alaskan North Slope. GIScience & Remote Sensing, 56:1, 87-108
- **Sturm** M., Holmgren J. and Liston G.E. (1995): A seasonal snow cover classification system for local to global applications. *Journal of Climate, 8, 1261–1283*
- **Tait** A. (1998): Estimation of snow water equivalent using passive microwave radiation data. *Remote Sensing of Environment, 64, 286–291*
- **Trishchenko** A.P. (2017): MODIS Time Series for Ellesmere Island Derived From Canada 10-day Composites Over 2000-2017 Period. Product Details*. Natural Resources Canada/Earth Sciences Sector/Long Term Satellite Data Record.*
- **Ulaby** F.T. and **Moore** R.K. (1982): Microwave Remote Sensing: Active and Passive. Volume 2: Radar Remote Sensing and Surface Scattering and Emission Theory. *Reading, MA, USA: Addison-Wesley*
- **Ulaby**, F.T., Moore R.K. and Fung A.K. (1986): Microwave Remote Sensing: Active and Passive, From Theory to Applications. *Artech House, Norwood, Mass.*
- **Ulaby**, F.T., Moore R.K., Fung A.K. and House A. (1981): Microwave Remote Sensing: Active and Passive. *Vol. 1. Massachusetts: Addison-Wesley Reading*
- **Upton** G. and **Cook** I. (1996): Understanding Statistics. *Oxford University Press, p. 55*
- **Van** Den Broeke M., König-Langlo G., Picard G., Munneke P.K. and Lenaerts J. (2010): Surface Energy Balance, Melt and Sublimation at Neumayer Station, East Antarctica. *Antarctic Science 22(1): 87-96*
- **Vikhamar** D. and **Solberg** R. (2003): Snow-cover mapping in forests by constrained linear spectral unmixing of MODIS data. *Remote Sensing of Environment, 88, 309–323*
- **Vögtli** M. (2018): Land surface dynamics of the Canadian Arctic Archipelago and adjacent Greenland observed using optical and SAR time series.
- **Wagner** W., Hahn S., Kidd R., Melzer T., Bartalis Z., Hasenauer S., Figa-Saldaña J., De Rosnay P., Jann A. and Schneider S. (2013): The ASCAT Soil Moisture Product: A Review of ist Specifications, Validation results, and Emerging Applications. *Meteorologische Zeitschrift 22(1): 5-33.*
- **Wan** Z., Hook S. and Hulley G. (2015): MOD11C1 MODIS/Terra Land Surface Temperature and the Emissivity Daily L3 Global 0.05Deg CMG. *JPL and MODAPS SIPS – NASA. NASA LP DAAC*
- **Wang** L., Derksen C. and Brown R. (2008): Detection of pan-Arctic terrestrial snowmelt from QuickSCAT, 2000–2005. *Remote Sensing of Environment, 112, 3794–3805*
- **Wang** L., Sharp M., Brown R., Derksen C. and Rivard B. (2005): Evaluating of spring snow covered area depletion in the Canadian Arctic from NOAA snow charts*. Remote Sensing of Environment, 95, 453–463*
- **Wang** L., Wolken G.J., Sharp M.J., Howell S.E.L., Derksen C., Brown R.D., Markus T. and Cole J. (2011): Integrated Pan-Arctic melt onset detection from satellite active and passive microwave measurements, 2000-2009. *Journal of Geophysical research, 116, D22103*
- **Warren** S.G. and **Wiscombe** W.J. (1980): A model for the spectral albedo of snow, II, snow containing atmospheric aerosols. *J. Atmos. Sci.* 37, 2734–45
- **White** A. and **Copland** L. (2018): Area change of glaciers across Northern Ellesmere Island, Nunavut, between ~1999 and ~2015. *Journal of Glaciology, 64, 246, 609-623*

- **Winebrenner** D.P., Nelson E.D., Colony R. and West R.D. (1994): Observation of melt onset on multi-year Arctic sea ice using the ERS 1 synthetic aperture radar. *Journal of Geophysical Research: Oceans (1978–2012), 99 (C11) (1994), pp. 22425-22441*
- **Winsvold** S.H., Kääb A., Nuth C., Andreassen L.M., Pelt W.J.J. and Schellenberger T. (2018): Using SAR satellite data time series for regional glacier mapping. *The Cryosphere, 12, 867-890*
- **Winther** J., Gerland S., Örbaek J.B., Ivanov B., Blanco A. and Boike J. (1999): Spectral reflectance of melting snow in a high Arctic watershed on Svalbard: some implications for optical satellite remote sensing studies. *Hydrological Processes, 13, 2033–2049*
- **Wiscombe** W.J. and Warren S.G. (1980): A model for the spectral albedo of snow, I, pure snow. *J. Atmos. Sci.* 37:2712–33
- **Woodhouse**, I. H. (2005): Introduction to Microwave Remote Sensing. CRC Press.
- **Yackel** J.J. and **Barber** D.G. (2000): Melt ponds on sea ice in the Canadian Archipelago: 2. On the use of RADARSAT-1 synthetic aperture radar for geophysical inversion. *Journal of Geophysical Research: Oceans (1978-2012), 105 (C9), pp. 22061-22070*
- **Zeng** Q., Cao M., Feng X., Liang F., Chen X. and Sheng W. (1984): A study of spectral reflection characteristics for snow ice and water in the north of China. *Hydrological Applications of Remote Sensing and Remote Data Transmission, 145, 451–462*
- **Zhao** H. and **Fernandes** R. (2009): Daily snow cover estimation from Advanced Very High Resolution Radiometer Polar Pathfinder data over Northern Hemisphere land surfaces during 1982–2004. *Journal of Geophysical Research, 114, 1–14*
- **Zhou** C., Zheng L., Sun Q. and Liu R. (2019): Amery Ice Shelf surface snowmelt detected by ASCAT and Sentinel-1. *Remote Sensing Letters, 10:5, 430-438*
- **Zhou** X., Li S. and Stamnes K. (2004): Effects of vertical inhomogeneity on snow spectral albedo and its implication for optical remote sensing of snow. *J. Geophys. Res.* In press
- **Zwally** H. J. and **Gloersen** P. (1977): Passive microwave images of polar regions and research applications. *Polar Rec., 18, 116, 431-450*

## Personal Declaration

I hereby declare that the submitted thesis is the result of my own, independent work. All external sources are explicitly acknowledged in the thesis.

Zürich, 29.04.2019

Place, Date

Simon H.

Signature